Development of a Compton Telescope with 3D Imaging Calorimeter for Gamma-Ray Astronomy

Aleksandar Gostojic Gostojić

▶ **To cite this version:**

Aleksandar Gostojic Gostojić. Development of a Compton Telescope with 3D Imaging Calorimeter for Gamma-Ray Astronomy. Instrumentation and Methods for Astrophysic [astro-ph.IM]. Université Paris Saclay (COmUE), 2016. English. NNT : 2016SACLS136 . tel-01333558

HAL Id: tel-01333558

https://theses.hal.science/tel-01333558

Submitted on 17 Jun 2016

HAL is a multi-disciplinary open access archive for the deposit and dissemination of scientific research documents, whether they are published or not. The documents may come from teaching and research institutions in France or abroad, or from public or private research centers.

L'archive ouverte pluridisciplinaire **HAL**, est destinée au dépôt et à la diffusion de documents scientifiques de niveau recherche, publiés ou non, émanant des établissements d'enseignement et de recherche français ou étrangers, des laboratoires publics ou privés.

NNT : 2016SACLS136

THESE DE DOCTORAT
DE
L'UNIVERSITE PARIS-SACLAY
PREPAREE A
L'UNIVERSITE PARIS-SUD

CENTRE DE SCIENCES NUCLÉAIRES
ET DE SCIENCES DE LA MATIÈRE

ÉCOLE DOCTORALE N°576
Particules, Hadrons, Énergie, Noyau,
Instrumentation, Imagerie, Cosmos et Simulation

Spécialité de doctorat : Astrophysique Nucléaire et Nucléosynthèse

Par

M. Aleksandar Gostojić

DÉVELOPPEMENT D'UN TÉLESCOPE COMPTON AVEC UN CALORIMÈTRE IMAGEUR 3D POUR L'ASTRONOMIE GAMMA

Thèse présentée et soutenue à Orsay, le 21 Avril 2016 :

Composition du Jury :

M. KHAN, Elias	Professeur – Université Paris-Sud	Président
Mme HANLON, Lorraine	Professeur – UCD, Dublin	Rapporteur
M. LAURENT, Philippe	Ingénieur chercheur – APC, IRFU/SAp, Paris	Rapporteur
M. JEAN, Pierre	Professeur – IRAP, Toulouse	Examinateur
M. DE SEREVILLE, Nicolas	Chercheur - IPNO, Orsay	Examinateur
M. TATISCHEFF, Vincent	Directeur de Recherche – CSNSM, Orsay	Directeur de thèse

Mojim roditeljima.

To my parents.

A mes parents.

Acknowledgments

Before expressing any gratitude, I will allow myself a moment to share my reflections on the past several years I have been working on the manuscript you hold. These years, were, without a doubt, a time fulfilled with the most resonating experiences of my life, making me who I am today. A person much different then the one who stepped inside the building 104 to begin his Master 2 internship, more than 4 years ago. I have grown on a personal plan, I have grown on a professional plan maybe even more. I had the honor to work with some of the best scientists in the field today, to feel the frontiers of science, to present in front of great audiences in different countries, to publish my first paper... A start of a scientific career to wish for!

As such, it brings me great pleasure, being able to say thank you to all the people I came in contact with over this period, I will mention some of you by name, but in the same manner, a big greetings go to all of you!

Firstly, I wish to thank Mr. Jean Antoine Scarpaci, director of CSNSM, for supporting my thesis and our project from the very beginning, and Mr. Jean Duprat, assistant director of the CSNSM, for the equal support and following my progress over the years.

I am deeply grateful to the members of the jury of my PhD defense: Mr. Elias Khan, the president of the jury, for his constant support, Ms. Lorraine Hanlon and Mr. Philippe Laurent, the rapporteurs, for their patience while reading the first manuscript and valuable inputs which improved it. Further, to the two examinaters: Mr. Pierre Jean, for the interesting discussion and interest in our work and Mr. Nicolas de Séréville, our colleague on the project, for the great cooperation over the time.

Moreover, I owe a very important debt to the ladies from our lab for always having a smile, and making my non-scientific part of the day feel great. Firstly, to Ms. Réjane Bodson, to whom I have said thank you numerous times, but I repeat it gladly, thanks for guiding me through, what is without exaggeration, every single document in existence. Thank you Mesdames Christelle Dodeman-Denys, Sonia Martineau, Patricia Duarte, Kim N'Guyen, Christine Zaoui, Emilie Bonnardel and Moufida Dziri-Marcé.

To the person, who without a doubt, deserves the biggest thanks and the biggest acknowledgement for this work, my thesis director Mr. Vincent Tatischeff, it was a pleasure and a privilege to work with you, and thank you for always being there for me, for all the patience and guidance and simply for being the best supervisor any student can wish for.

I would also like to offer my gratitude to the members of our nuclear astrophysics group: Jürgen Kiener, Clarisse Hamadache, Alain Coc and Anne Lefebvre-Schuhl; for clarifying various questions, providing invaluable assistance and most importantly nice workdays.

Special thanks to the electronics group of CSNSM for all the work and effort they placed into the project, and for patiently making the acquisition work every time when we needed it: Vincent Alaphilippe, Laurent Gibelin, Nabil Karkour, Xavier Lafay and Denis Linget. My deepest appreciation also goes to the IT developers Eric Legay, Nicolas Dosme and Xavier Grave. I am also grateful to Gregory Sedes, Isabelle Deloncle, Bruno Travers and Stéphane Cabaret for the work and assistance they provided during the initial phase of the project, and to Jean Peyré for sharing many consultations on all possible technical issues.

My gratitude also goes to Ms. Sylvie Loeffel from the école doctorale PHENIICS for all the urgent emails she answered, Ms. Marine Valois from the University Library for being patient and helpful in polishing my final manuscript, and to all other personnel of the Université Paris-Sud who I came in contact with.

Cheers to all the stagiaires, students and postdocs I had the pleasure to meet, even if briefly: Rosa for my first coffee breaks, Vincent for being a friend in need, Nejc for sharing his apartment, and a big group shout-out to the guys from building 108.

My love goes firstly to my parents Leli i Mitru, hvala, no words can describe what you have done for me over the years, but likewise to my other someone, Nathalie, thanks bibs.

Finally, hey to my friends, wherever you are in the world, for all of the real and virtual support and moments: Bojana, Tanja, Irena, Budo, Dunja, Miso, Bojane, Sarah, Lorena, Jovane and all of you other wonderful people I have the pleasure to know.

I will try to make all of you proud in the pages that follow and all yet to come ...

Contents

1 Gamma-ray astronomy **7**
- 1.1 Introduction . . . 7
- 1.2 Ground-based gamma-ray instruments . . . 8
- 1.3 Space borne gamma-ray instruments . . . 10
- 1.4 MeV astronomy . . . 14
  - 1.4.1 MeV astronomy science . . . 15
  - 1.4.2 Gamma-ray interaction with detector material . . . 16
  - 1.4.3 Principle of a Compton telescope . . . 19
  - 1.4.4 New concepts in MeV gamma-ray instruments . . . 22

2 A prototype of an advanced Compton telescope **27**
- 2.1 Introduction . . . 27
- 2.2 The ACT prototype test bench . . . 27
  - 2.2.1 Tracker . . . 28
  - 2.2.2 Calorimeter . . . 30
- 2.3 Simulations of the ACT prototype . . . 30
  - 2.3.1 MEGAlib . . . 30
  - 2.3.2 Model of the prototype . . . 31
  - 2.3.3 Simulated performance . . . 32

3 Development of the Calorimeter testbench **37**
- 3.1 General view of the test-bench . . . 37
- 3.2 $LaBr_3$:Ce detector module . . . 38
- 3.3 $CeBr_3$ detector module . . . 39
- 3.4 Electronics and data acquisition . . . 40
- 3.5 Calibration of the acquisition system . . . 42
- 3.6 Scanning measurements . . . 45
- 3.7 Energy measurements . . . 48
- 3.8 One photoelectron calibration . . . 48

4 Geant4 simulation of the Calorimeter modules **51**
- 4.1 Introduction to Geant4 . . . 51
  - 4.1.1 Simulating optical light propagation and tracking . . . 52
- 4.2 Simulating the $LaBr_3$:Ce and $CeBr_3$ detector modules . . . 53
  - 4.2.1 $LaBr_3$:Ce simulation configuration . . . 54
  - 4.2.2 Parametrization of the $LaBr_3$:Ce simulation . . . 55
  - 4.2.3 Simulation versus experiment for the $LaBr_3$:Ce detector . . . 56
  - 4.2.4 Simulation of the $CeBr_3$ detector . . . 59

5 Gamma-ray tracking with an Artificial Neural Network **63**
5.1 Introduction . . . 63
5.1.1 Artificial Neural Network . . . 63
5.1.2 JETNET 3.0 . . . 64
5.2 ANN configuration and training . . . 67
5.3 ANN performance using simulated data . . . 68
5.3.1 X–Y position reconstruction . . . 68
5.3.2 Depth of interaction reconstruction . . . 68
5.3.3 Module design optimization . . . 71

6 Experimental results **73**
6.1 Position reconstruction . . . 73
6.1.1 Anger logic algorithm . . . 73
6.1.2 ANN performance with experimental data . . . 74
6.1.3 2D position resolution . . . 77
6.1.4 Depth-of-interaction reconstruction . . . 82
6.2 Energy characterization . . . 83
6.2.1 Energy dynamic range . . . 84
6.2.2 Energy resolution . . . 84

Conclusions and perspectives **89**

Appendix **94**

A Defining geometry for the simulation of the $LaBr_3$:Ce module **95**

Synthèse de la thèse en français **111**

Chapter 1

Gamma-ray astronomy

1.1 Introduction

Astronomy of today implies performing observations over the whole range of the electromagnetic spectrum (see Figure 1.1), from radio astronomy with lowest energies of order of 1 peV (10^{-12} eV; $1.24{\times}10^{15}$ nm) to gamma-rays with energies going up to 100 TeV (10^{14} eV; $1.24{\times}10^{-11}$ nm). To study each of these energy bands astronomy expanded into scientific subfields such as X-ray astronomy, which focuses on X-rays or optical astronomy, which studies the visible spectrum and others. Each of these require separate instruments and study methods, but in return each field provides us with wast amount of information. Some phenomena may be studied by more than one field, others are unique to a specific energy signature or a narrow energy interval.

In the same manner, gamma-ray astronomy is the astronomy which focuses on the most energetic phenomena. It starts at energies of several hundreds keV and goes up to several hundred TeV, covering more than nine orders of magnitude of the electromagnetic spectrum. Formally, there is no upper energy limit to gamma rays, yet pair-production on background photons ($\gamma + \gamma \rightarrow e^+ + e^-$) effectively sets a horizon to the explorable Universe. For photon

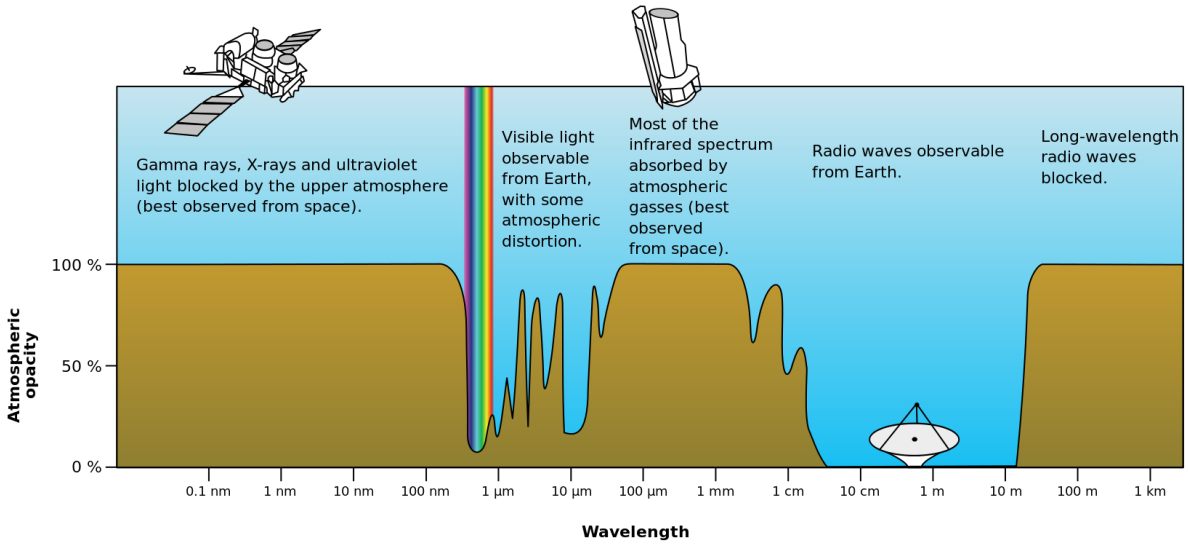

Figure 1.1: Opacity of the Earth's atmosphere as a function of photon wavelength.

energies above 1 PeV (10^{15} eV), this horizon is of the size of our Galaxy (*Gould and Schréder*, 1966). Even more, the modern gamma-ray astronomy is divided into more narrow fields, such as: the low-energy range from about 100 keV to 2 MeV, the medium-energy range from about 2 to 100 MeV, the high-energy range from about 100 MeV to 100 GeV and the very-high-energy range above 100 GeV.

Gamma-ray astronomy has been growing since the mid of 20th century and provided us with the opportunity to study a wide range of topics, including stellar coronas, white dwarf stars, neutron stars, black holes, supernova remnants, clusters of galaxies, diffuse gamma-ray background radiation, gamma-ray bursts, pulsars and many others. The broad width of the gamma-rays energy range necessitates a big versatility in detectors applied. However, we can roughly separate all of the instruments into two groups: first one includes telescopes installed on the ground, which are grouped into 'ground-based' gamma-ray astronomy instruments, and second one are all instruments carried into atmosphere or space by balloons and satellites, they constitute 'space-borne' gamma-ray astronomy.

1.2 Ground-based gamma-ray instruments

Ground based instruments, as mentioned, are all the instruments located on the Earth's surface. Usually they involve an array of several interconnected telescopes focused on detection of gamma-rays with energies above 100 GeV (very-high-energy gamma-ray astronomy). The main principle of work is an indirect detection of high energy γ-rays through their interaction with the Earth's atmosphere. One example would be a telescope array based on Cherenkov technique, illustrated on the Figure 1.2, as it is one of the main techniques used today.

As seen on Figure 1.2, the incoming high energy γ-ray enters and interacts with the Earth's atmosphere, and so produces secondary particles which may further interact with the atmosphere on their own. Such chain effect may eventually lead to a creation of an air shower effect, i.e. the creation of an "avalanche" of particles in the atmosphere. If the particles in the shower possess speeds close to the speed of light they will emit visible radiation (blue light on Figure 1.2), due to Cherenkov radiation effect. Cherenkov radiation is then directly visible and recorded via optical telescopes from the ground. The Cherenkov cone opening is of the order of $10^5 - 10^6$ m^2. The array of telescopes aims to cover as much of this area as possible. The data

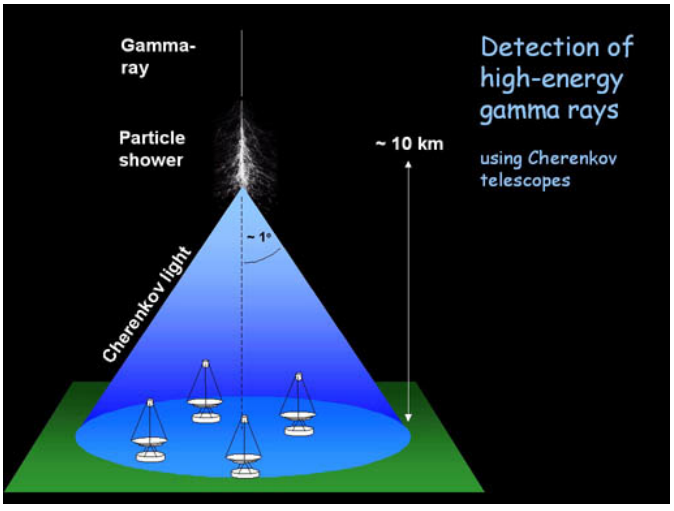

Figure 1.2: EM shower, cherenkov light, telescopes

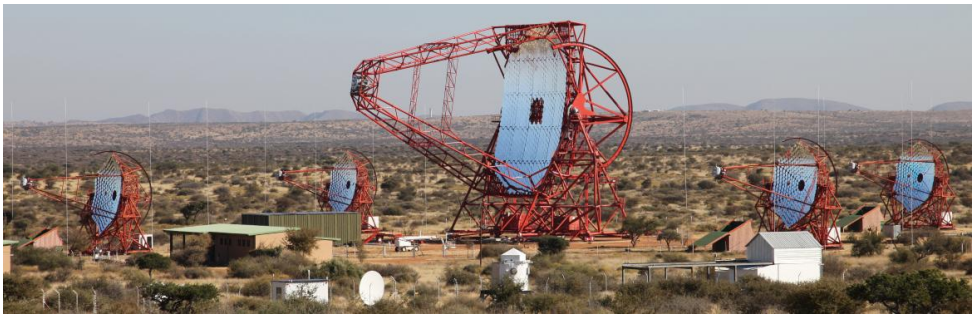

Figure 1.3: H.E.S.S. Telescope Array located in Namibia. It consisted of 4 smaller, 12 meters diameter telescopes, and one central telescope of 28 meters diameter.

from all of the individual instruments is then combined, in order to reconstruct the energy and the point/direction of origin of the primary γ-ray. An example of such telescope array is the High Energy Stereoscopic System (H.E.S.S.) shown on Figure 1.3.

On each telescope dish the Cherenkov light is collected via mirrors and focused on high sensitivity cameras. Some other well known telescopes, of the same type are: MAGIC, VERITAS and a future concept called the Cherenkov Telescope Array (CTA).

The CTA, Figure 1.4 is a large telescope array, currently under development, aiming to detect Very High Energy (VHE) gamma-rays, with the operating range from 10 GeV up to 300 TeV. When finished, the CTA will include two large groups of telescopes, one located in the Northern and the other located in the Southern hemisphere.

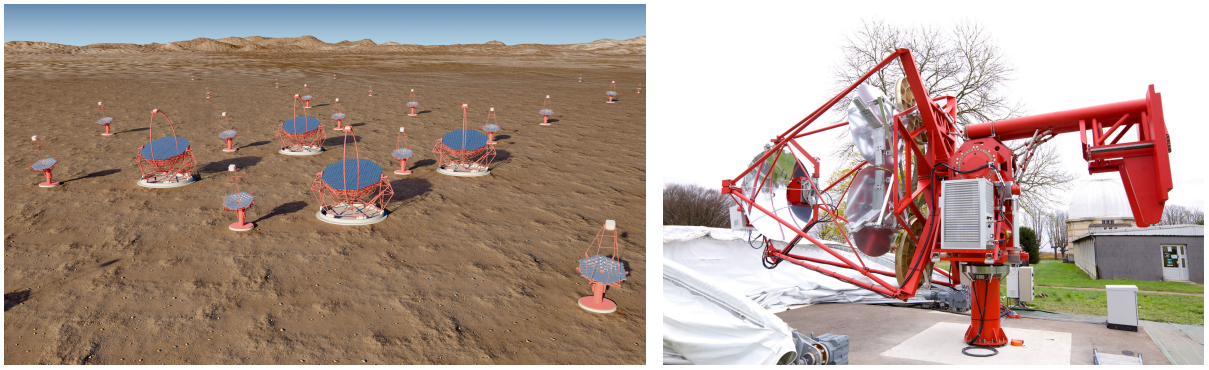

Figure 1.4: $Left$: Artist impression of the CTA site, including 23 m and 12 m telescopes. $Right$: Gamma-ray Cherenkov Telescope (GCT), one of the prototype instruments for the CTA. GCT is a small 4 m diameter telescope, installed at Paris Observatory in Meudon. It is also the first Schwarzschild-Couder telescope to be used in detection of the Cherenkov light.

Currently the $Location\ South$ is planned in Atacama desert in Chile and $Location\ North$ is planned on La Palma in the Canary Islands, Spain. The construction phase is expected to last from 2018 to 2023. Each of the two locations will be designed using different types of Imaging Atmospheric Cherenkov telescopes (IACTs) depending on the energy range they observe. Several big, 23 m diameter telescopes, will focus on the gamma-rays between 20 and 200 GeV, a bigger array of medium, 12 m telescopes, will focus on energies from 100 GeV to 10 TeV and finally a large number of small, 4 m telescopes, is planned for the highest energies from several up to several hundred TeV. Although, the exact number of individual instruments is not yet determined, performance studies have been done with $Location\ South$ containing 4 big, 24 medium and 72 small telescopes and $Location\ North$ having 4 big and 15 medium-sized tele-

scopes (*Bernlöhr et al.*, 2013). The scientific goals are roughly grouped into three main parts: the origin and role of cosmic rays, nature and variety of particle acceleration around black holes and the search for the nature of matter and physics beyond the Standard Model[1].

1.3 Space borne gamma-ray instruments

On the other hand, gamma-rays, from 0.1 MeV up to 10 GeV, are not visible from Earth and are mostly absorbed by the Earth's atmosphere (see Figure 1.1). Therefore, to be able to study this part of the gamma-ray spectrum, balloons and satellites carrying instruments are launched into the Earth's stratosphere or orbit. In this way, a direct observation of gamma-ray sources is performed.

In fact, this is why gamma-ray astronomy, as a discipline had a late start, it lacked any means for direct observations of gamma-rays from space. Therefore, first real experiments started after the 1960s. However, even before any experimental confirmations, there were various scientific works predicting the existence of gamma-ray sources in the universe. Processes such as: cosmic ray interactions with interstellar gas, supernova explosions, and interactions of energetic electrons with magnetic fields were all believed to produce gamma-rays.

The first real astrophysical observation in gamma-rays domain was the detection of 2.223 MeV line from the solar flares, predicted by *Morrison* (1958). One of the first notable gamma-ray missions was Orbiting Solar Observatory 3 (OSO-3) mission, launched in 1967. Over the operating period of 16 months it recorded 621 gamma-ray sources, mostly above 50 MeV, distinguishing among galactic equatorial, galactic center and extragalactic sources, while mapping the sky distributions (*Kraushaar et al.*, 1972). The mission carried various experiments utilizing NaI(Tl) and CsI(Tl) scintillators, photomultipliers and Anti-Coincidence Shielding (ACS) made of plastic scintillators.

Next notable gamma-ray mission was the Small Astronomy Satellite B (SAS-B/SAS-2) (*Fichtel et al.*, 1975). It was launched by NASA in 1972. It consisted of spark chambers and Cherenkov counters with ACS, and operated in 30–200 MeV range. The main purpose was to measure the spatial and energy distribution of primary galactic and extragalactic gamma-ray emissions.

The first gamma-ray mission from ESA, Cosmic ray Satellite ('option B'.) or COS-B was launched in 1975. It provided extensive and important results in the energy range from 50 MeV to 5 GeV, including: creation of 2CG Catalogue (*Swanenburg et al.*, 1981) with over 25 detected gamma-ray sources, the first complete map of the gamma-ray emission from the disc of our Galaxy and the first detectable emission from an extra-galactic object 3C273. The instrument implemented a CsI calorimeter and a spark chamber for determining the direction of gamma-rays (*Bignami et al.*, 1975).

In 1979. NASA launched (H.E.A.O. 3) the third of its High Energy Astronomy Observatory satellites. It was the first mission to carry a gamma-ray instrument based on high-resolution Germanium detectors (*Mahoney et al.*, 1980). The 'C-1' or The Gamma-ray Line Spectrometer Experiment was an instrument made with oxygen cooled p-type High-Purity Ge (HPGe) detectors enclosed with CsI scintillators. It was capable of monitoring energies from 45 keV up to 10 MeV. Over six months it performed all-sky surveys, observing numerous gamma-ray lines, including the ^{26}Al line at 1.8 MeV for the first time.

[1] see: `https://www.cta-observatory.org/` for more detailed topics.

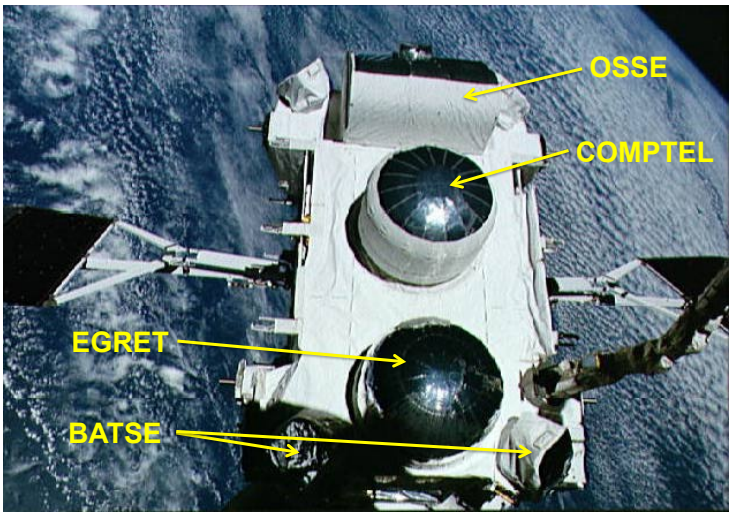

Figure 1.5: View of the Compton Gamma Ray Observatory during deployment of the spacecraft.

In more recent history we have the two of the biggest realized gamma-ray astronomy missions; NASA's Compton Gamma-Ray Observatory (CGRO) mission and ESA's INTEGRAL mission.

Compton Gamma-Ray Observatory (CGRO) was the second of NASA's Great Observatories. At 17 tons, it was the heaviest astrophysical payload ever flown at the time of its launch, aboard the space shuttle Atlantis, on April 5th, 1991. CGRO was safely de-orbited and re-entered the Earth's atmosphere on June 4, 2000. CGRO carried four instruments (Figure 1.5). COMPTEL (a classical Compton telescope, see Sect. 1.4.3) was one of the main instruments on board and was used to study the gamma-ray sky between 0.8 and 30 MeV. Energetic Gamma Ray Experiment Telescope (EGRET) was a pair production telescope, which covered the energies from 20 MeV up to 30 GeV, composed of multi-level thin plate spark chamber for pair production detection with NaI scintillators underneath for added dynamics range. The Burst and Transient Spectrometer Experiment (BATSE) was an all sky monitor used for search of gamma-ray bursts, in the range of 20–600 keV. It was composed of modules containing NaI Spectroscopy Detector and NaI Large Area Detector. The Oriented Scintillation Spectrometer Experiment (OSSE) was designed to undertake comprehensive observations of astrophysical sources in the 0.05-10 MeV energy range. Secondary capabilities for gamma-ray and neutron observations above 10 MeV have also been included, principally for solar flare studies. The primary detector element was the NaI(Tl)-CsI(Na) phoswich consisting of a 102-mm thick NaI(Tl) crystal optically coupled to a 76-mm thick CsI(Na) crystal. Each phoswich was coupled from the CsI(Na) to seven 89-mm diameter photomultiplier tubes (PMTs), providing an energy resolution of 8% at 662 keV. Overall, the CGRO is a showcase of versatility in instrumental design for specific purposes.

INTErnational Gamma-Ray Astrophysics Laboratory (INTEGRAL) is more recent and another great example of MeV astronomy instruments. This, still ongoing, big space mission was launched in 2002. by ESA. Onboard it has two instruments dedicated for gamma-ray detection (Figure 1.6): the Spectrometer on-board INTEGRAL (SPI) and the Imager on-board INTEGRAL (IBIS). SPI has a very high energy resolution of 2.2 keV (FWHM) at 1.3 MeV. It can observe energy interval between 18 keV and 8 MeV. The very high energy resolution comes from 19 hexagonal HPGe detectors which are used as primary calorimeters. Above the calorimeters is a complex hexagonal coded aperture mask. The coded mask is used to "cast a shadow" on the

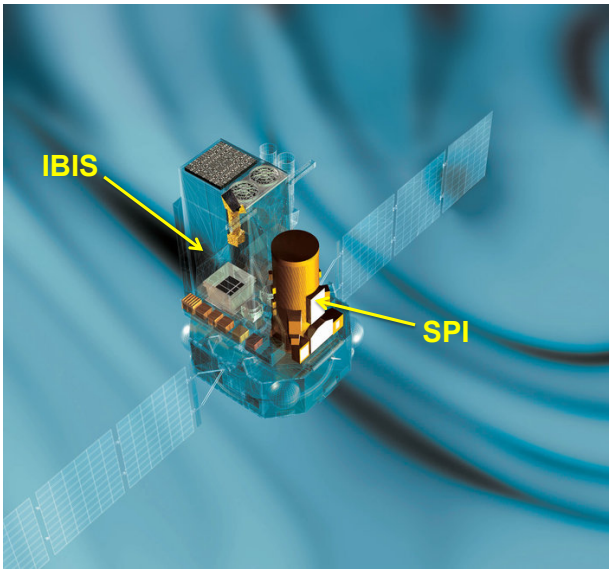

Figure 1.6: Artist's view of the INTEGRAL satellite.

detectors, by knowing the position of this shadow on the detectors plane it is possible to reconstruct the incoming direction of the detected gamma-rays. IBIS, on the other hand, focuses on monitoring the continuum emission and the broad lines within the range of 15 keV up to 10 MeV. It also has a coded mask and two layers of detectors. The upper layer, ISGRI, is made from 16384 CdTe crystals and is used for detecting lower energy gamma-rays, while the bottom one, PICsIT, consists of 4096 CsI detectors which capture higher energy gamma rays. IBIS can also work as a Compton telescope when ISGRI and PICsIT are used in coincidence (*Forot et al.*, 2007). Furthermore, two other instruments, OMC and JEM-X, are monitoring the visible and X-ray bands, respectively. This is a good example of how complex detection and study of gamma-ray phenomena can be, involving sometimes observations from several instruments covering different wide ranges of EM spectrum.

Fermi Gamma-Ray Space Telescope (formerly GLAST) is a large mission launched by NASA in 2008. It carries two main instruments onboard, first is a Large Area Telescope (LAT) and the second is The Glast Burst Monitor (GBM).

Fermi covers the gamma-rays energies from 8 keV up to 300 GeV. Main purpose of the LAT is to perform all sky surveys by covering the entire sky each 3 hours, with the ability for more precise point observation. It is a pair-production telescope comprised of two main detector volumes: a tracker and a calorimeter, both shielded with the anti-coincidence detectors. LAT's tracker is made of 16 tower modules, where each has 16 single sided silicon detector layers separated with 18 tungsten converter layers, meant for inducing the pair creation. The calorimeter is made of 16 CsI(Tl) modules, each containing 96 crystals placed in 8 layers. The anti-coincidence is done with a series of plastic scintillators placed outside of the detectors. The GBM instrument is aiming to monitor all sky, whenever possible and search for very prompt gamma-ray emissions, such as gamma-ray bursts (GRBs). The GBM is placed on the opposite side of LAT, and it has two main types of detectors: 12 NaI(Tl) scintillators for monitoring the X-rays and low-energy gamma rays from 8 keV to 1 MeV, and two bismuth germanate (BGO) detectors for monitoring higher energies up to 30 MeV. This currently operating mission has, so far, provided many important results and discoveries. Some of the examples of Fermi results are:

- Discovery of the first gamma-ray pulsar not emitting in any other wavelengths (PSR

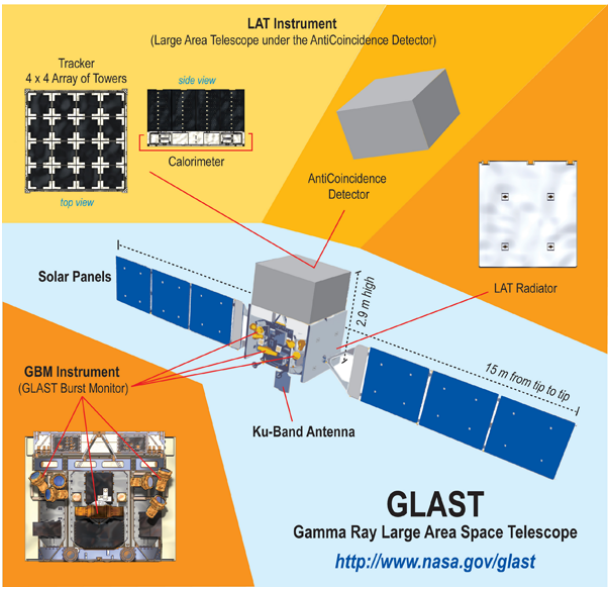

Figure 1.7: Fermi (GLAST) satellite schematic, with noted two main instruments: LAT - with tracker, calorimeter and ACS; and GBM on the opposite side.

J1906+0722).

- Measurement of the strongest energy release, recorded up to date, from a gamma-ray burst (GRB 080916C).
- Discovery of the gamma-ray bubbles originating from the center of the Milky Way.
- Detection of more then 160 gamma-ray pulsars (only 9 were catalogued before Fermi mission), including the first gamma-ray pulsar from another galaxy (PSR J0540-6919).
- Observation of the first pulsar (PSR J1023+0038) that underwent emission transformation from X-rays to gamma-rays, within the binary system AY Sextantis. Noted as the first example of a transient, compact, low-mass gamma-ray binary.
- Establishing classical novae as a distinct class of gamma-ray sources. For the first time ever, Fermi detected gamma-ray emissions produced by novae explosions, observing four such cases: V407 Cyg 2010, V1324 Sco 2012, V959 Mon 2012 and V339 Del 2013.

Figure 1.8 shows the sensitivity of several space and ground-based instruments of high-energy astronomy. The highest energies, the TeV scale, is covered with high sensitivity ground based instruments such as HESS and CTA (Sect.). Such sensitivity is matched or even surpassed with X-ray instruments, at the opposite side of the spectrum, e.g. with the Chandra observatory. Contrarily, the MeV range is standing out by poorest achieved sensitivity. The reasons for such inequality in coverage are discussed in the following section.

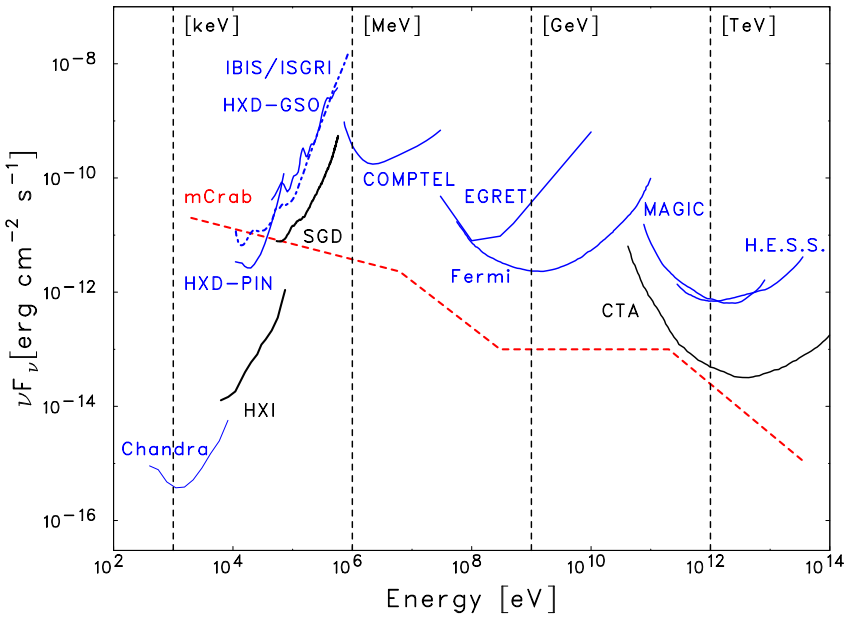

Figure 1.8: Sensitivity achieved in different energy bands of the gamma-ray astronomy by different instruments (from: *Takahashi et al.*, 2012). Here, $\nu F_\nu = S(E) \times E^2$, where E is the photon energy and $S(E)$ the differential sensitivity, i.e. the minimum flux (e.g. in photons cm^{-2} s^{-1} MeV^{-1}) that can be detected at a given confidence level (usually 3σ or 5σ) after a given time of observation of the astrophysical source (see: *Takahashi et al.*, 2012). The lines in blue represent past or currently operating instruments, while instruments planned for the near future are in black. The dashed red line shows the sensitivity reference expressed by mCrab, an equivalent to one thousandth part of intensity detected from the Crab nebula (including the Crab pulsar within it).

1.4 MeV astronomy

From the Figure 1.8 it is straightforward that the sensitivity of the instruments in the MeV range is weaker, up to five orders of magnitude, when compared to instruments in other energy bands. In association with this, stands the fact that currently and in the near future there are no planned missions to specifically cover the MeV range. Therefore the MeV astronomy remains an understudied part of the EM spectrum, and, at the moment, leaves a big scientific potential untouched. These facts, apart from being the main problems for the MeV astronomy are at the same time the main motivator which drives the community to constantly work and push out new ideas and projects in order to overcome the sensitivity gap. However, there are several strong limitations which provide a challenge for constructing instruments with higher-than-current sensitivities:

1. Gamma-rays are very hard to reflect, since their wavelengths are much smaller than the typical interatomic distance. Consequently, focusing mirrors for gamma-rays are of limited performance and require large focal lengths, and as such are difficult to operate in space.

2. The instrumental background in the MeV range is very high, as MeV is also the domain of nuclear γ-ray lines which are produced by irradiation and activation of active and passive materials of the instrument in space.

3. Within the MeV range, the dominant process of photon interactions with matter is Compton scattering, which causes difficulties in reconstructing detected events.

4. The probability of photons interacting with matter reaches minimum at around 1 MeV, which additionally decreases the probability for detection.

1.4.1 MeV astronomy science

The MeV astronomy domain is nevertheless associated with various scientific questions and future studies may provide information of interest to a large number of fields. Some of the main scientific topics of present MeV gamma-ray astronomy[2] include:

- Cosmic rays; their origin, propagation and interaction. Observation of emission between 0.1 and 10 MeV, e.g. 4.4 MeV and 6.1 MeV lines from ^{12}C and ^{16}O respectively, would give a direct measurement of the densitiy of low-energy cosmic-rays (LECRs) in the Milky Way.

- Supernovae; for the supernovae of the type Ia and related subtypes, information such as ignition mechanism and stellar configuration may be deduced from the radioactive isotopes they produce. Therefore, detecting gamma-rays from these isotopes is a diagnostics tool to study the explosion process. For example, one of such isotopes is the ^{56}Ni and its radioactive chain. For core collapse type II supernovae observations on isotopes as ^{56}Co, ^{57}Co can give information on nucleosynthesis, dynamics, possible jet formation and more. ^{44}Ti is one of the radioactive nuclei which is present in all supernovae explosions (thermonuclear and core collapse) and is one of the most important tools to search for supernovae remnants and study the physical parameters of supernovae explosions.

- Novae; they produce several gamma-ray lines of interest which may put constrains on theoretical understanding of these objects. Most important are 511 keV line from e^+–e^- pairs annihilation, 478 keV from ^{7}Be decay and 1275 keV from ^{22}Na decay.

- Gamma-ray lines from long lived radioactive isotopes; e.g. ^{26}Al and ^{60}Fe are produced and ejected into the interstellar medium by massive stars. Their lifetimes are of the order of 10^6 years, comparable to the evolutionary time scales of the OB associations and the stars contained within. The presence of these isotopes traces the regions where massive stars formed recently. Further, by mapping the ^{26}Al in the Galactic plane, we could see at which locations star formation happens and where the large-scale outflow from these regions transports matter, energy and momentum within the Galactic disc.

- Gamma-ray bursts; overall study of gamma-ray bursts through spectroscopy and polarimetry in the MeV range may explain the physics of GRB jets as well as particle acceleration and emission.

- Blazars and Active galactic nuclei (AGNs); most AGNs discovered so far emit in the MeV range, thus MeV astronomy can boost the discovery of new AGNs, placing constraints on physical models, determining the energy output.

- MeV emission from neutron-star and black-hole binaries; both inflows and outflows in accreting black-hole binaries can produce continuum MeV emission. Relativistic electrons appear to be present in accretion flows in both hard and soft spectral states. MeV

[2] see, e.g., the AstroMeV website at `http://astromev.in2p3.fr/?q=aboutus/science`.

tails due to their Compton emission have been discovered in Cygnus X-1 and a number of other sources. Jets of those systems are known to contain relativistic electrons and can produce MeV emission via both synchrotron and Compton processes. Thus, studying the MeV emissions we could understand both the jets and accretion flows in those systems.

- Gamma-ray emission from magnetars and rotation-powered pulsars; magnetars are neutron stars with extremely powerful magnetic fields. It is still not clear which processes, in such extreme fields, produce the non-thermal soft gamma-rays emission, nor do we understand the connection between the pulsar and magnetar population. More sensitive and extensive study of the pulsar emissions in the MeV range, can help identify the sources of these emissions and understand pulsar population.

- Gamma-ray emission from the active Sun; lots of questions related to solar flares such as the mechanisms of energy release and the acceleration of particles may be resolved by observation of various gamma-ray lines emitted from the Sun, e.g. 4.44 MeV from ^{12}C and 6.13 MeV from ^{16}O are prompt lines produced in nuclear collisions during the solar flares. Further examples of solar gamma-ray activity include, the 2.2 MeV line from neutron capture on hydrogen or delayed lines produced by radioactive isotopes synthesized during flares, such as 847 keV from ^{56}Co, or still unobserved ^{52}Mn line predicted at 1434 keV.

- Terrestrial Gamma-Ray Flashes; study of recently discovered terrestrial gamma-ray flashes (TGFs). Their emission spectrum goes up to 100 MeV and contains a 511 keV annihilation line as well. The process of TGFs creation is not yet explained and is believed to be connected to particle acceleration during thunderstorms. More information on the topic would greatly improve our understanding of atmospheric phenomena and climate in general.

1.4.2 Gamma-ray interaction with detector material

Primary principle of detecting gamma rays in the MeV range is based on exploiting main gamma-rays interaction mechanisms with matter.

As seen on Figure 1.9, depending on the incident energy, gamma rays may undergo several processes: photoelectric absorption, Compton scattering and e^+–e^- pair production.

1.4.2.1 Photoelectric absorption

Photoelectric effect is the dominant interaction for X-ray and gamma-ray energies from several keV up to several hundred keV. An incoming gamma-ray interacts primary with a bound atomic electron, transferring its total energy to the interaction material and disappearing in the process. In order for photoelectron to be emitted from the material, the energy of the gamma-ray has to be higher than the binding energy of an electron. The photoelectric effect can be followed by fluorescent emission which can further lead to secondary photoelectric effect. The energy of the created photoelectron E_{e^-} is given by the formula:

$$E_{e^-} = h\nu - E_{\mathrm{ION}} \tag{1.1}$$

where $h\nu$ is the energy of the original gamma-ray and E_{ION} is the ionization or binding energy of the electron in the atomic shell. Essentially, E_{ION} is also absorbed in the interaction material, as X-ray radiation and due to Auger effect following the photoelectric absorption. The

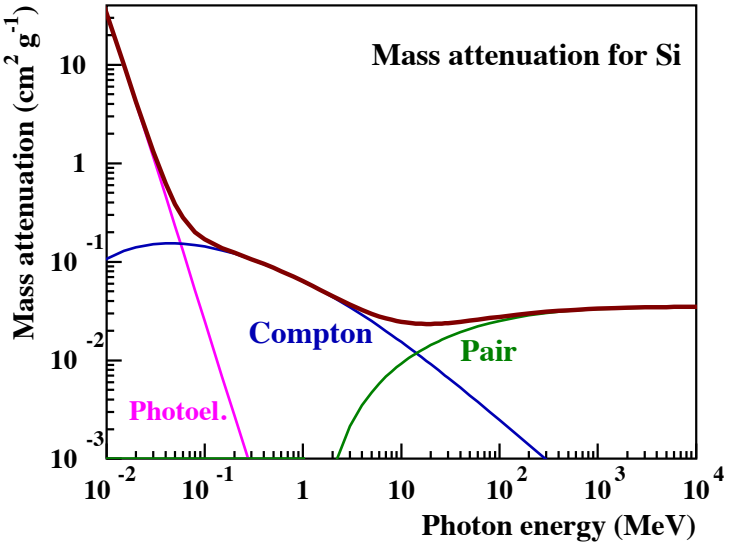

Figure 1.9: Cross-sections for different interactions of gamma-rays with matter, calculated for Si, depending on the energy of an incident gamma-ray.

probability for the photoelectric effect scales roughly as:

$$p_{\text{photoelectric}} \propto \frac{Z^n}{(h\nu)^3}\,, \tag{1.2}$$

where Z is the atomic number of the target material and the exponent n ranges from 3 to 4 depending on the energy.

1.4.2.2 Compton Scattering

The probability for Compton interaction increases for gamma-rays above 100 keV and becomes the dominant interaction at ∼1 MeV. The effect is illustrated on Figure 1.10. An incident gamma-ray is scattered on an electron and thus changes its original trajectory and energy. An electron, called Compton electron, receives a part of the gamma-ray's energy and also changes its trajectory. The energy of the scattered γ-ray is given by the classical Compton formula:

$$E'_\gamma = E_\gamma \frac{1}{1 + \frac{E_\gamma}{m_e c^2}(1 - \cos\Theta)}\,, \tag{1.3}$$

where m_e is the mass of an electron at rest and scattering angle Θ may take any value from 0 to 2π.

The differential cross section of Compton scattering for unpolarized photons scattering off unbound electrons is given by the Klein-Nishina formula:

$$\frac{d\sigma}{d\Omega} = \frac{1}{2}\alpha^2 {r_c}^2 f(E_\gamma,\Theta)^2[f(E_\gamma,\Theta) - f(E_\gamma,\Theta)^{-1} - 1 + \cos\Theta^2]\,, \tag{1.4}$$

where α is a fine structure constant, $r_c = \frac{\hbar}{m_e c}$ is the reduced Compton wavelength and $f(E_\gamma,\Theta) = \frac{E'_\gamma}{E_\gamma} = \frac{1}{1+\frac{E_\gamma}{m_e c^2}(1-\cos\Theta)}$. The above equation is also called the unbound Compton cross section since the electron is assumed to be not bound to an atom and therefore to be at rest. Because this is not the case for any detector material used in Compton telescopes today, the Klein-Nishina cross section constitutes an approximation.

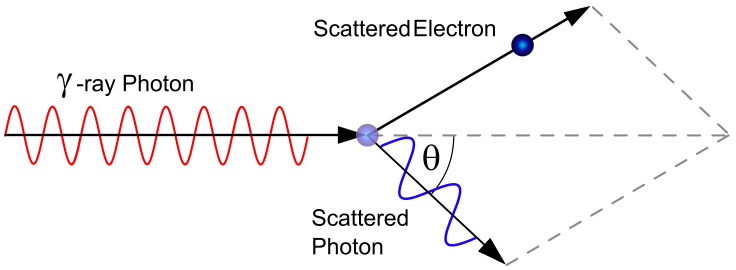

Figure 1.10: Simple representation of a Compton effect. The incident gamma-ray (in red) hits an electron at rest and scatters with lower energy (in blue). The noted angle Θ is the angle between the original and scattered direction of the gamma-ray, and is called Compton scattering angle. A part of energy is also given to the electron, called Compton electron, which scatters in a different direction, defined by the electron scattering angle.

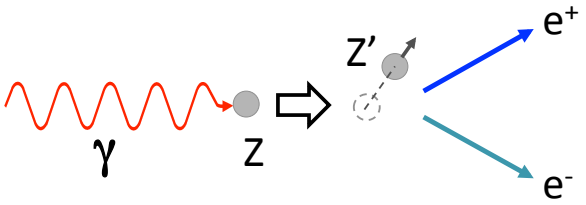

Figure 1.11: Representation of an electron-positron ($e^- e^+$) pair production in the electromagnetic field of a nucleus of charge Z. Noted with Z' is the nucleus of the same charge but with change in momentum due to occurred interaction.

1.4.2.3 Pair production

When a gamma-ray possesses an energy above 1.022 MeV (double energy of an electron at rest) it can interact with matter via pair production. The interaction usually occurs in the electromagnetic field of a nucleus and the energy of an incident gamma-ray is transformed to produce an electron-positron pair ($e^- e^+$). The excess of energy of the gamma-ray affects the nucleus, which recoils. The effect is visualized on Fig. 1.11 and described through the following equations of energy and momentum conservation:

$$E_\gamma = E_{e^-} + E_{e^+} + E_n + 2m_e c^2 \tag{1.5}$$

$$\vec{p}_\gamma = \vec{p}_{e^-} + \vec{p}_{e^+} + \vec{p}_n \ . \tag{1.6}$$

Here, E_{e^-}, E_{e^+}, and E_n are the kinetic energies of the electron, positron and recoiling nucleus, respectively, and $\vec{p}_i$ is the momentum of the particle i.

If the photon's energy exceeds four times the rest mass of an electron, pair creation can also happen in the field of an electron. Here the momentum is not transferred to the nucleus, but instead to the target electron. The ratio of the probability for pair production on an electron to that for pair production on a nucleus is given by:

$$p_{\text{electron}} = \frac{1}{CZ} p_{\text{nucleus}} \ , \tag{1.7}$$

where C is a factor depending on the incident gamma-ray energy, e.g. $C = 2.6$ at $E_\gamma = 6$ MeV and $C = 1.2$ at $E_\gamma = 100$ MeV.

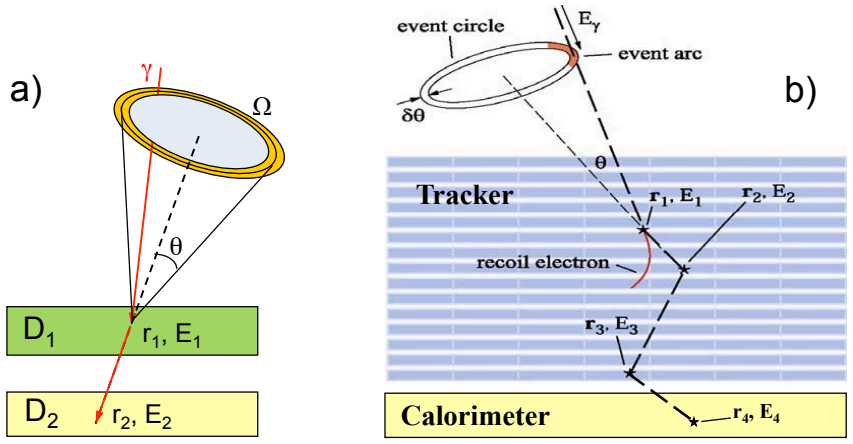

Figure 1.12: a) Principle of a classical Compton telescope made of two detectors D1 and D2. b) An advanced Compton telescope comprising a tracker allowing the tracking of the Compton electron and a 3-D position sensitive calorimeter. Measuring the direction of the recoil electron can constrain the gamma-ray event to an arc of the Compton annulus.

1.4.3 Principle of a Compton telescope

A so-called classical Compton telescope operates on the method of collecting enough data to be able to calculate all of the values from the Compton formula (Eq. 1.3). It uses a double detector plane as shown in Figure 1.12a. The first plane is used to scatter the incident gamma-rays. In order to increase the probability of Compton scattering with respect to photoelectric absorption and pair creation, low-Z materials are used. Indeed, the Compton scattering probability scales as the number of electrons of the target atom, i.e. Z, whereas the probability for the photoelectric effect scales as Z^n with n in the range 3–4 (see Eq. 1.2) and that for the pair production scales as Z^2. After scattering it is possible to capture the photon in the second plane. Here, high-Z materials are used in order to fully absorb the energy of the scattered photon. Combining the energy left in both D1 and D2 we have:

$$E_\gamma = E_1 + E_2 \tag{1.8}$$

and

$$\Theta = \arccos\left[1 - m_e c^2 \times \left(\frac{1}{E_2} - \frac{1}{E_1 + E_2}\right)\right]. \tag{1.9}$$

The above equation gives the scattering angle Θ with respect to the direction defined by the two positions of interaction r_1 and r_2 inside the detector planes D1 and D2 (Fig. 1.12a). The calculated direction of an incoming gamma-ray is thus limited to an event circle in the sky and not a specific direction (i.e. a point in the sky).

Finding interaction position within the detector is possible through two options. The first one is to use highly pixelated detectors, made out from a lot of small detector units. The second is to create one big detector and perform position localization within it, a method we are using in our work and that we shall explain more later on. Finally, it is important to maintain the correct sequence of events, where for one event we should know which interaction, either in detector D1 or D2, is the first and which is the second. This can be done by performing time-of-flight measurements between the two detector planes, as in the COMPTEL instrument of the CGRO mission.

1.4.3.1 Advanced Compton Telescope (ACT)

Shown on Figure 1.12b is an ACT concept. By simple comparison with a classical Compton telescope we note a more compact design, where two detector layers, a tracker and a calorimeter, are next to each other, without any spacing. The tracker is made of multiple layers which allows for detection of events with several Compton interactions, opposed to e.g. single event tracking with COMPTEL. This contributes to a gain in detection efficiency and in field-of-view (FOV) of an ACT, and is allowed by new detector materials.

The main characteristic of an ACT is the use of detectors with a fine sensitivity to the 3D positions of the interactions, in order to track with high accuracy, both, the scattered gamma rays and the Compton electrons. This is important for distinguishing a cosmic gamma-ray photon from a background event produced by, e.g. a cosmic-ray particle impinging the satellite or a radioactive decay from an activated material within the telescope. Taking a full advantage of recent progresses in silicon detectors and readout microelectronics, the tracker of an ACT can be made by a stack of double sided Si strip detectors (DSSSDs) with fine spectral resolution. In general, the possibility to track Compton recoil electrons significantly increases the precision on reconstructing the position of origin of gamma-rays. However, electron tracking is possible only for gamma-rays with energies above about 1 MeV, depending on the thickness of the tracker detectors, as they transfer enough energy for scattered electrons to leave visible tracks in the detector. The benefits of tracking are explained in the next subsection.

Furthermore, an ACT may use two concepts for the calorimeter design, either a highly pixelated detector volume or connected bigger detector blocks with an imaging capability. Both are used to track the impact position of detected gamma-rays. However, new scintillators and electronics allow the creation of monolithic scintillator detector modules with imaging capability in 3D. The 3D first-impact-position reconstruction of a detected gamma-ray, when combined with increase in spectral resolution, results in improving the constraints on reconstruction of Compton events.

1.4.3.2 Compton Imaging

Once a full Compton event is detected, we are able to reconstruct a so-called Compton or event cone, as noted on the Figure 1.12. The properties of the reconstructed event circle or arc, shown on the right panel of Fig.1.12, depend on the performance of the detectors. The more precise they are, the thicker and more intense the event circle (arc) will be. Such general method, used by Compton satellites, of determining the position from which the detected gamma-rays originate is named Compton Imaging and is illustrated on the Figure 1.13.

Image on the left of Fig. 1.13 is a Compton image obtained with a classical Compton telescope. Each cone corresponds to a detected gamma-ray, and, as mentioned, the accuracy on energy and position measurements influence the shape of the cones. By detecting multiple events with the same origin, the intersection of many event cones determines the position of a detected gamma-ray source.

Using an ACT we can benefit from increased precision by employing the mentioned Compton recoil electron tracking. An example is given on the middle image on Figure 1.13. Such image is usually obtained by detecting the gamma-rays of energies between about 1 and 10 MeV, where the Compton electron paths can be tracked. The information gained from knowing electron scattering angle and its energy allows the reduction of an event cone to an event arc, where the precision by which they are measured defines the arc's size. The far right image on the Fig. 1.13 is the case of Compton reconstruction of high-energy events with electron

Figure 1.13: $Left$: A Compton image gained from a classical Compton telescope. $Middle$: An image obtained with a Compton telescope capable of electron tracking. $Right$: Imaging with electron tracking for the case of high-energy events (from: *Zoglauer*, 2006).

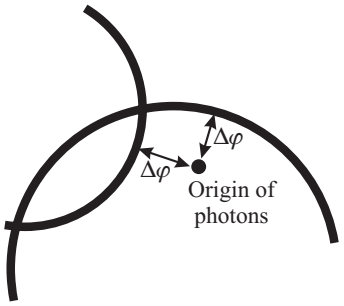

Figure 1.14: The ARM ($\Delta\varphi$) is the measure of the width of the Compton scatter cone or an arc. The $\Delta\varphi_{ARM}$ value can be positive, meaning the real point of origin lays outside the cone and we have an incomplete detection of an recoil electron, or if $\Delta\varphi_{ARM}$ is negative, the point of origin lies inside the cone, and the scattered gamma-ray is incompletely absorbed (*Zoglauer*, 2006).

tracking. Usually, gamma-rays with energies above 10 MeV are not fully detected, meaning the Compton scattering is incompletely absorbed by the instrument. However, for these events the recoil electrons receive high enough energies, so they have a well defined recoil paths. Such paths are easier to track and thus provide an increase in precision on determining the original position of the gamma-ray source.

1.4.3.3 Angular resolution measure

For any Compton telescope, the ability to determine the point of origin (the incoming direction) of a detected gamma-ray, is, as noted before, limited by the uncertainties of the measurement (i.e. energy or position resolution) and additionally by Doppler broadening. Therefore, through a value named Angular Resolution Measure (ARM), we express the precision of an instruments in determining the original direction of the detected events. The ARM is defined as the smallest angular distance between the known point of origin and the Compton cone (*Zoglauer*, 2006). Or in other words, the shortest distance between the known original direction of the photon and the scatter cone reconstructed from the information on the scattered gamma photon. The ARM is illustrated on the Figure 1.14.

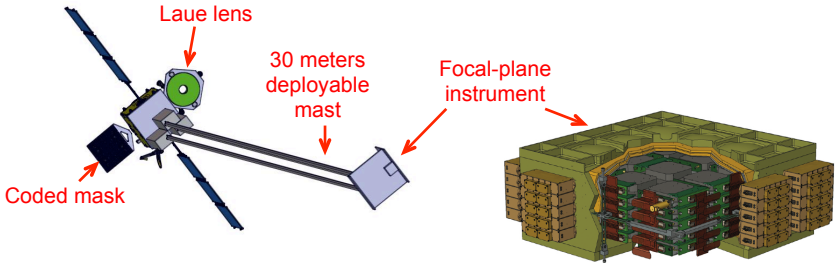

Figure 1.15: DUAL in deployed configuration with a detailed view of the focal plane instrument ASCI (All-Sky Compton Imager) made of a compact array of cross-strip germanium detectors.

1.4.4 New concepts in MeV gamma-ray instruments

To be able to access the science of the MeV range and to overcome the instrumental limits, the MeV scientific community is working constantly on new concepts of instruments and detection, with the goal to gain experience and better prepare for the future missions. I will give a list of several such projects, proposed to the European Space Agency (ESA) over past several years, as they illustrate new ideas and approaches in the field, and then in Chapter 2 give an overview of our project, as a part of these future space mission research and development. In addition, the work presented in the next chapters is a direct continuation of work done for missions such as e.g. GRIPS (detailed below).

1.4.4.1 Gamma-ray proposals of ESA's M3 Call

In 2010, the European Space Agency solicited proposals from the broad scientific community for the competitive selection of mission concepts to be candidate for the implementation of the third medium-size mission ("M3") of the *Cosmic Vision* scientific program for launch in 2025. Three proposals were issued by the gamma-ray community: DUAL (*von Ballmoos et al.*, 2012), CAPSiTT (*Lebrun et al.*, 2010) and GRIPS (*Greiner et al.*, 2012).

DUAL was a proposal which implements a novel type of gamma-ray lens. Using a mosaic of small crystals in Laue geometry (*e.g. see: Section 2, von Ballmoos, 2007)*, allows the focusing of gamma-rays through diffraction on a small detection area. This provides the separation of collection and detection area, reducing background, as less material is used. The concept is shown on Figure 1.15. The focal plane instrument is a Compton telescope made of cross-strip Ge detectors working in the range from 0.1 to 10 MeV. However, the drawback of germanium is the need for a cooling system. In addition to a Laue lens, the main satellite also carries a coded mask. The plan was to use a Soyuz launcher to place the DUAL instrument in an L2 orbit.

Compton And Pair Silicone Timing Tracker (CAPSiTT), illustrated on Figure 1.16, is an all silicon instrument, made from layers of double sided silicon strip detectors (DSSSDs). The operational energy range was from 100 keV up to 100 MeV. It can work as a pair production telescope and Compton telescope, using a 3 Compton technique, where by knowing the energy and position of two consecutive Compton scatterings can give us the incoming direction of the original particle. The advantages include lower mass, which means lower internal background, and the use of a single technology for the whole instrument. However, this concept requires a large number of thick (2 mm) DSSSDs (11520 detectors of $10 \times 10\mathrm{cm}^2$ area), which raises a problem of supply and cost. As for the space deployment, idea was to use a VEGA launcher to send the instrument to an equatorial low-Earth orbit (at about 550 km altitude).

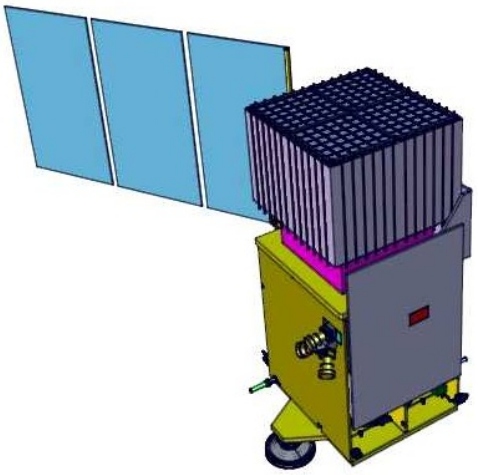

Figure 1.16: View of the CAPSiTT payload made of a stack of double-sided silicon strip detectors, on top of the Sentinel 3 platform developed by Thales Alenia Space.

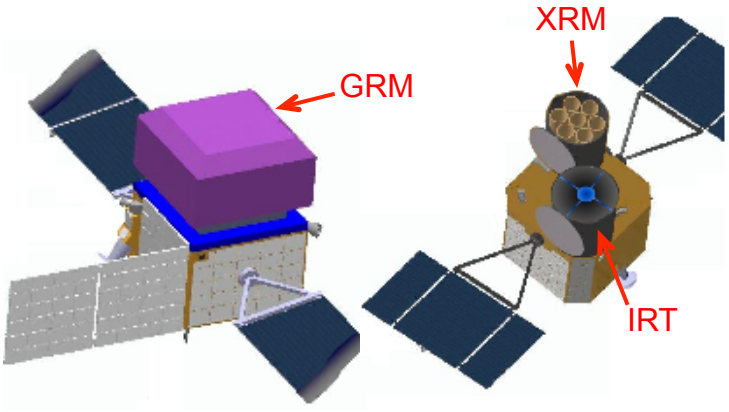

Figure 1.17: GRIPS configuration in the two satellite option, where the Gamma-Ray Monitor (GRM) is on one satellite, and the X-Ray Monitor (XRM) and the InfraRed Telescope (IRT) on the other.

Gamma-Ray Imaging, Polarimetry, and Spectroscopy (GRIPS) (Figure 1.17) was the third M3 ESA mission proposal for a gamma-ray observatory. The main on-board instrument Gamma-Ray Monitor (GRM) is an ACT and a pair-production telescope, meant to operate between 0.2 and 100 MeV. It is designed out of two main detector layers. The first detector is a tracker constructed of 64 layers of 8×8 DSSSDs of $10 \times 10\ \mathrm{cm}^2$ area. The tracker works as a Compton scatterer in the Compton telescope mode, and as a pair production telescope in the high-energy mode, above about 10 MeV. Above 2 MeV the DSSSDs are able to perform a tracking of a Compton recoil electron. The second main GRM detector is a calorimeter made of a very large number ($\sim$ 75000) of small $LaBr_3$:Ce scintillator bars of $5 \times 5\ \mathrm{mm}^2$ cross section with the total mass of ~ 500 kg. The scintillator crystals are read out with Si Drift Diode (SDD) photodetectors and are encasing the tracker volume from all sides, apart the detection plane. The side scintillators are 2 and 4 cm thick, while the bottom one is 8 cm thick and read out on both ends. Such calorimeter enables the GRM to operate in the 'spectroscopy' mode, apart from the 'telescope' mode; this implies performing only spectroscopic measurements of energy deposits inside the scintillators, for e.g. high-level spectroscopy of the GRBs. The whole

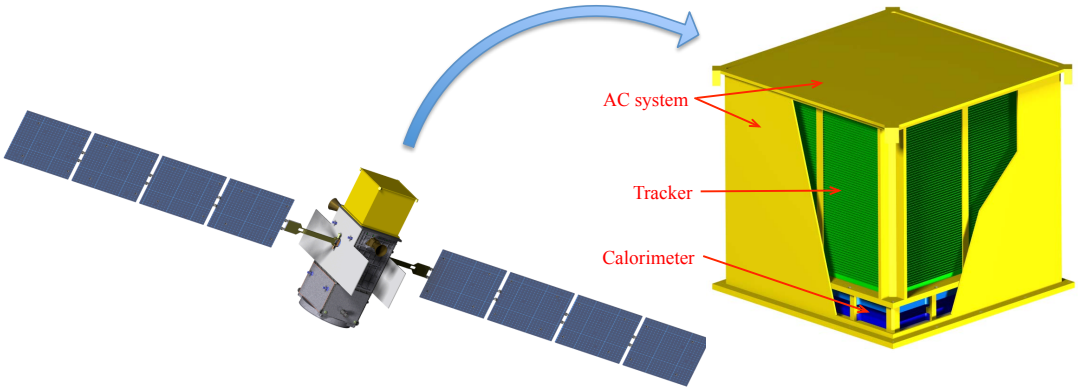

Figure 1.18: $Left$: ASTROGAM satellite with deployed solar panels and radiators. $Right$: Zoom-in on the satellite's payload showing the Silicon Tracker, the Calorimeter and the Anti-Coincidence (AC) system.

GRM instrument is surrounded with an Anti-Coincidence Shielding (ACS) made with plastic scintillators.

GRIPS mission carries two further instruments, an X-Ray Monitor (XRM) and an InfraRed Telescope (IRT). The main purpose of XRM is to gain the precision on the determining the position of the GRBs, where it works in the combination with GRM, and further to observe the GRB emission in the X-ray range from 0.2 to 12 keV. It is a concept made of 7 Walter-I telescopes, identical to eROSITA instrument (*Predehl et al.*, 2014). The IRT is meant to to rapidly identify the GRBs at high redshift. It is a telescope of mirrors with multi-band photometry similar to the EUCLID mission (*Laureijs et al.*, 2010). The GRIPS mission was supposed to be launched to equatorial low-Earth orbit using a Soyuz launcher.

In summary, although quite different in their design (with or without a calorimeter, associated or not to a focusing optics etc.), the three gamma-ray instruments proposed for ESA's M3 Call were all advanced Compton telescopes with some capabilities for electron tracking, characterized by a very large field of view to monitor the poorly known MeV gamma-ray sky.

1.4.4.2 ASTROGAM

ESA's Call for the fourth medium-size mission opportunity in the Agency Science Program was released in August 2014 and the proposal submission deadline was January 15, 2015. This time, the gamma-ray scientific community has responded in a unified manner by working together on a single proposal: the ASTROGAM mission. The main elements of the ASTROGAM payload (Figure 1.18) include a Si Tracker made from 2520 Si DSSSDs arranged in 70 layers of 6×6 tiles, which is coupled to a calorimeter made from 12544 bars of CsI(Tl) scintillation crystals.

The operating modes of such instrument are $Compton\ regime$ from 0.1 to 10 MeV and $pair-production$ regime up to 3 GeV. The Si tracker, similarly to GRIPS or CAPSiTT, is capable of resolving energy deposits and tracking of both the Compton photon and (for the energies above 1 MeV) the recoil electron. While the calorimeter, due to precision and high pixelization, is capable of resolving both the energy and the interaction position of a Compton scattered photon. Combined with an Anti-Coincidence Shielding (ACS) the instrument operates as an Advanced Compton Telescope which performs Compton Imaging and polarimetry. At energies above 10 MeV, the Si Tracker is used as electron-positron pair production medium by gamma-rays interacting with the fields of hit nuclei within the tracker, allowing for ASTROGAM to

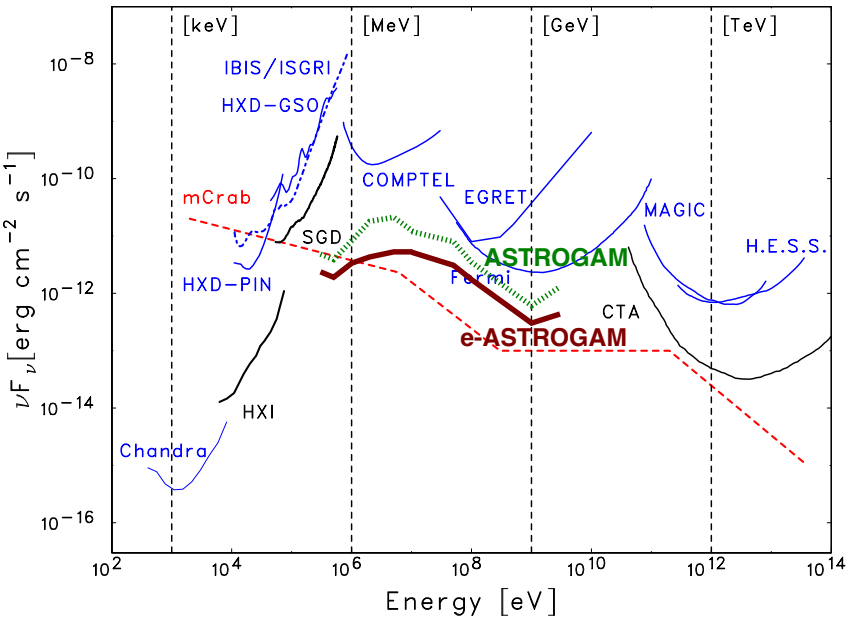

Figure 1.19: Same as Figure 1.8, but with the predicted sensitivity of ASTROGAM for an effective exposure of one year of a high Galactic latitude source. The curve for e-ASTROGAM is the goal sensitivity of the larger scale and enhanced instrument that will be proposed to ESA in 2016 in response of the M5 Call.

function as a pair-production telescope.

Following ESA's guidelines for the M4 Call, the ASTROGAM payload was designed to have a mass of 300 kg. Although the proposed mission concept has been very well evaluated by ESA's Technical and Programmatic Evaluation Panel, it was unfortunately finally not selected for a mission study. For the M5 Call, to be issued in 2016, the ASTROGAM Collaboration is currently working on a larger scale instrument and satellite (the e-ASTROGAM mission), with an estimated payload mass of about one ton. The enabling technologies and processes will be the same as those of the M4 project. Such an extension of the mission concept is aiming at further improving the leap in sensitivity compared to previous missions, especially between 1 and 10 MeV (see Fig. 1.19).

In the preliminary design of e-ASTROGAM, the Si Tracker consists of four units comprising 56 layers of 5×5 DSSSDs. Each DSSSD has a geometric area of 9.5×9.5 cm^2, a thickness of 500 μm, and a strip pitch of 240 μm. The total detection area then amounts to 9025 cm^2 and the total Si thickness to 2.8 cm, which corresponds to 0.3 radiation length on axis. The e-ASTROGAM Calorimeter comprises 8464 parallelepiped bars of CsI(Tl) of 8 cm length (corresponding to 4.3 radiation length) and 10×10 mm^2 cross section. The scintillation light of each bar is collected by two matrices of 4×4 SDDs, which are glued to the crystal at both ends. The new design aims to further significantly improve the sensitivity in the crucial energy range 0.3 – 100 MeV (see Fig. 1.19). The proposed gamma-ray observatory would then open an entirely new window of opportunity for discovery in the evolving energetic Universe.

Chapter 2

A prototype of an Advanced Compton Telescope

2.1 Introduction

The main goal of this thesis is to develop and study a small scale prototype of an Advanced Compton Telescope (ACT). The prototype consists of one to three double sided silicon strip detector (DSSSD) detector planes, that form the tracker, and one Anger-type calorimeter module, made of monolithic scintillator crystal. The tracker and the calorimeter are mounted on a specialized test bench that has been developed at CSNSM (Centre de Sciences Nucléaires et de Sciences de la Matiére) and IPN (Institut de Physique Nucléaire) in Orsay. The project is done in the framework of a collaboration between several research groups. IPNO and APC (AstroParticule et Cosmologie) laboratories are working on the tracker elements, primary on testing the DSSSDs and the corresponding read-out and acquisition systems. Our group at CSNSM is producing a calorimeter based on novel inorganic scintillator detectors, with the following electronics and acquisition system. In parallel, all of the work is connected to international collaboration under ASTROGAM proposals as well as any similar future missions for the MeV gamma-ray astronomy, with the overall goal to improve and push forward the performance of instruments in this range.

2.2 The ACT prototype test bench

The model of an instrument and a designed test-bench aimed for performance testing are presented on the Figure 2.1.

The mechanical device of the telescope is completed and the integration of the LaBr3:Ce module and the first DSSSD is under way. The system comprises supports to accommodate up to three DSSSDs with their associated FEE cards (the two developed at IPNO and the one made by the team of the LabEx UnivEarthS). The instrument is mounted on an X-Y table which allows the full frontal coverage using collimated gamma-ray sources. The complete readout from all detectors is lead to a PC and controlled by NARVAL (*Grave et al.*, 2005) based application. This entire device will be placed in a special black box, designed at IPNO, ensuring both the light sealing and good electromagnetic compatibility of the apparatus. Moreover, some of the test measurements will be performed in a climatic chamber, available at IPNO, at temperatures between -10^o and 20^o C. This will allow us to study the telescope under better operating

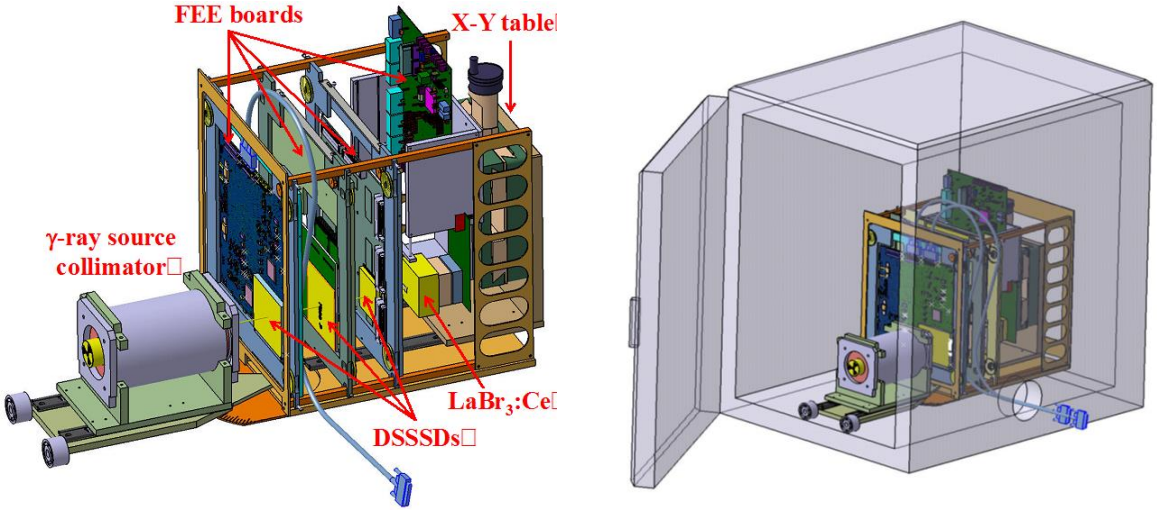

Figure 2.1: $Left$: Mechanical drawing of the gamma-ray telescope concept. $Right$: Presentation of the telescope and the collimator for radioactive gamma-ray sources inside the climatic chamber. The telescope is placed in a black box not shown in this diagram.

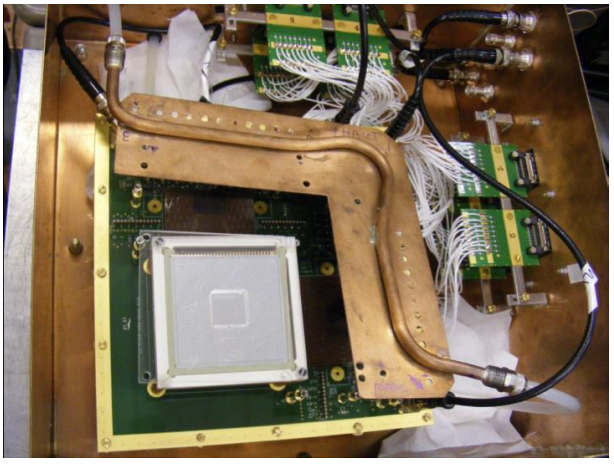

Figure 2.2: Photograph of the BB7 DSSSD test bench around PACI preamplifiers. The detector is mounted in the lower left corner of the electronic readout card. A copper cooling circuit provides temperature control of the preamplifiers.

conditions for the DSSSDs (low leakage current at low temperatures), closer to the expected conditions in space and the upper atmosphere.

2.2.1 Tracker

For the main element of the ACT prototype's tracker, the team studied the spectral response of the DSSSD BB7 version 2 of Micron Semiconductor Ltd, which is a detector of 64×64 mm^2 area, 1.5 mm thickness, and 32×32 strips. Initial tests showed that this detector has the ability to detect low energy deposits. To optimize the electromagnetic compatibility of the detection device, a first test bench, shown on Figure 2.2, was designed and constructed. The bench is dedicated to the reading of DSSSDs around a conventional analog electronics readout. This task required the realization of electronic cards around the PACI (charge preamplifier with additional current output) preamplifiers previously developed at IPNO (*Hamrita et al.*, 2004).

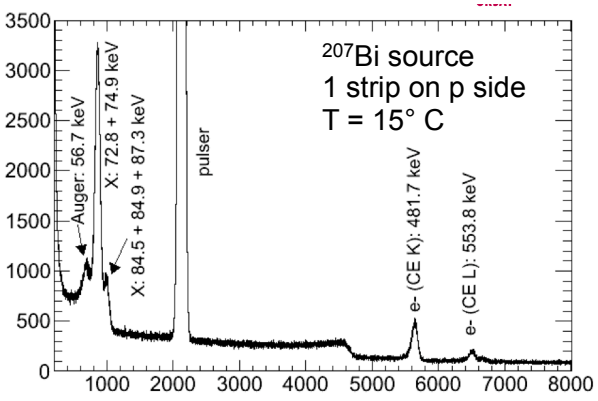

Figure 2.3: ^{207}Bi energy spectrum obtained with the BB7 DSSSD at IPNO, Orsay.

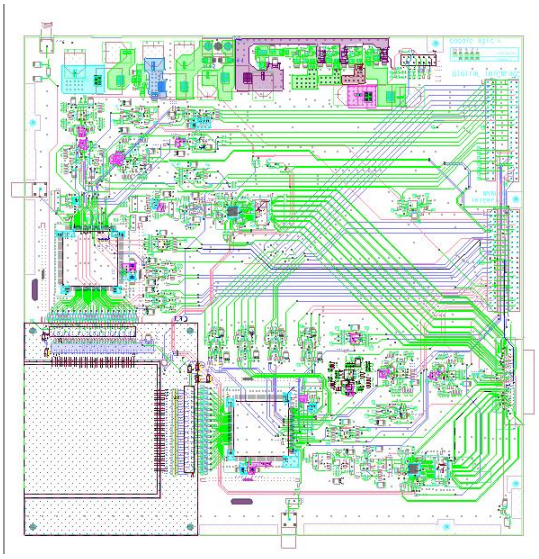

Figure 2.4: Computer-aided design of the FEE card of the BB7 detector.

With this device, the measured energy threshold is 11 keV and the energy resolution obtained is 8 and 10 keV (FWHM) at 59.5 keV (^{241}Am) for the p and n sides of the BB7 detector, respectively, which validates the choice of this sensor for our application. Figure 2.3 shows an example of the BB7 performance obtained with a ^{207}Bi electron source.

For the Compton telescope, the readout of the DSSSD signals is done with a low noise Application Specific Integrated Circuit (ASIC). We originally intended to use the ASIC ATHED, which was developed for the multi-detector of charged particles MUST2[1]. But after a series of tests, it was found that the spectroscopic resolution for the detection of low-energy deposits, with this ASIC, would be unacceptable for our application. After extensive market research, we selected the chip VA32TA7 from the Ideas company[2], which incorporates 32 channels of full electronic processing sensor signals. The Electronics Group of IPNO then designed an electronic board (see Figure 2.4) carrying a sensor BB7, two ASICs VA32TA7 (one for each sensor face), and an interface to a Field-Programmable Gate Array (FPGA) development board (ML605, Xilinx). The card passed the qualification phase and is now coupled to the detector BB7, which allows us to run extensive performance testing.

[1]see: `http://pro.ganil-spiral2.eu/laboratory/detectors/charged-particles/must2`.
[2]`http://www.ideas.no/`

2.2.2 Calorimeter

At CSNSM, we are working on the calorimeter modules made of large monolithic inorganic scintillator crystals (e.g. 50×50 mm^2 area and 1 cm thickness) coupled to position-sensitive arrays of photodetectors. The main focus, while developing these modules, is on achieving the best possible 3D imaging and spectral performances for MeV gamma rays. The goal is to improve the design of a future space calorimeter compared to the approach of the GRIPS and ASTROGAM proposals (Chapter 1), where the gamma-ray hit localization in the calorimeter is achieved with a pixelated detector comprising a large number ($\sim$ 75000 bars of $LaBr_3$:Ce for GRIPS and 12544 bars of CsI(Tl) for ASTROGAM) of thin scintillator bars (of 5×5 mm^2 cross section in both proposals for ESA, see Chapter 1). Using bigger crystals, having 3D imaging capabilities, in modules should allow us to reduce significantly the complexity of the future calorimeter while optimizing the spectral resolution of the instrument. We tested prototype modules made of $LaBr_3$:Ce and $CeBr_3$ scintillators, with the idea to use them as a multiplicative unit for any future large scale instrument. However, we found that the $LaBr_3$:Ce's intrinsic radiation, coming from ^{138}La (half-life: $T_{1/2} = 1.02\times10^{11}$ yr; natural abundance 0.09%) isotope, notably reduces its performance. Therefore, another option would be to try other new scintillator material, such as glass-ceramic scintillator (*de Faoite et al.*, 2015). $CeBr_3$ has no problems with intrinsic radioactivity, but however doesn't outperform the $LaBr_3$:Ce in our study.

The study of the calorimeter modules has been the essential work of this thesis, thus we describe the modules in detail in Chapter 3.

2.3 Simulations of the ACT prototype

2.3.1 MEGAlib

MEGAlib[3] (*Zoglauer et al.*, 2006), stands for the Medium Energy Gamma-ray Astronomy library, and represents a package of tools for simulating and studying the performance and data analysis of Compton telescopes. The necessity for such a package comes from the ever-growing amount of data which needs to be handled in todays instrument designs; time-of-flight or electron tracking are just some examples that have grown more complex in comparison to instruments such as COMPTEL or EGRET.

MEGAlib is completely based on C++ programing language, ROOT (see: *Brun and Rademakers* (1997) and `https://root.cern.ch/`) software and Geant4 (detailed in the next chapter). The idea is to use all the built-in features and apply them to any Compton telescope we wish to simulate. The library includes: different tracking options, multiple designs of Compton telescopes, various strip detectors, scintillators and drift chambers. An example of MEGAlib is given on Figure 2.5 with the original MEGA mission (*Bloser et al.*, 2005). The data analysis process can be separated into 4 main steps:

- *Data acquizition* can be done either by generating data through simulations or using data measured by real detectors.
- *Data optimization* either by calibration or introduction of calculated uncertainties from the real data.
- *Event reconstruction*, which includes recognition of the basic physical process (Compton scattering, pair production etc.), qualification of the events etc.

[3]available from: `http://megalibtoolkit.com/`

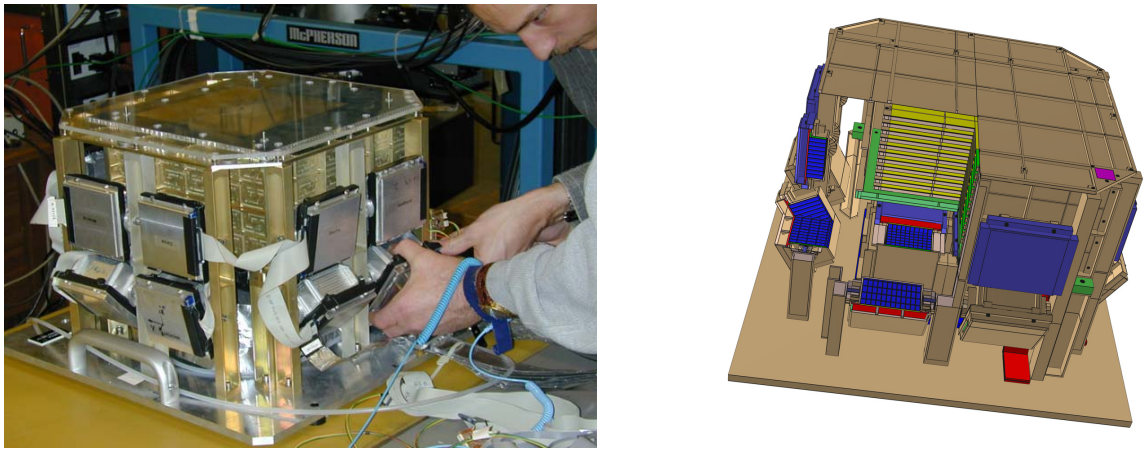

Figure 2.5: Medium Energy Gamma-ray Astronomy telescope (MEGA) mission; $Left$: scaled working prototype. The tracker in gold casing in the middle is made of 11 layers of 3×3 DSSSDs. The tracker is surrounded with 20 CsI(Tl) detectors placed in separate grey aluminium boxes. $Right$: a simulated geometry model corresponding to the prototype.

- $Data\ analysis$, which includes imaging and reconstruction, polarization analysis, sensitivity calculations etc.

In detail, MEGAlib includes the two following sub-packages:

- $GEOMEGA$ - Geometry for MEGAlib is intended to help create the main geometry to be used in MEGAlib and all connected software. It allows definition and visualization of all materials, volumes, detector materials and all other elements in use.
- $COSIMA$ - A Cosmic Simulator for MEGAlib based on Geant4 (*Zoglauer et al.*, 2009), it is intended as universal simulation tool for low and medium energy gamma-ray telescopes which are based on one of the basic gamma-ray interactions with matter (Chapter 1).

2.3.2 Model of the prototype

We have implemented a basic geometry (see Figure 2.6) and detector parameters within MEGAlib to simulate and test the performance of our ACT prototype model. The detector performance (energy threshold, spectral resolution, 3D position resolution) were taken from our experimental results, which are discussed later in Chapter 6.

In red, on Figure 2.6, is a volume which represents one DSSSD. The volume dimensions are: 64×64×1.5 mm^3 and is made of 32×32 Si strips. We use several measured values to place constraints on the parameters within the simulation, therefore for the DSSSD, we take:

- Electronics noise set to 8 keV
- Trigger threshold of 15 keV

On the right side of the image on Fig. 2.6, the calorimeter volume is represented in blue. The calorimeter is simulated using $LaBr_3$:Ce scintillator parameters. The volume is 50.8×50.8×10.0 mm^3 and is defined in MEGAlib as "3D strip" detector i.e. a 2D strip detector with depth resolution. The parameters we implement from measurements (Chapter 6) are:

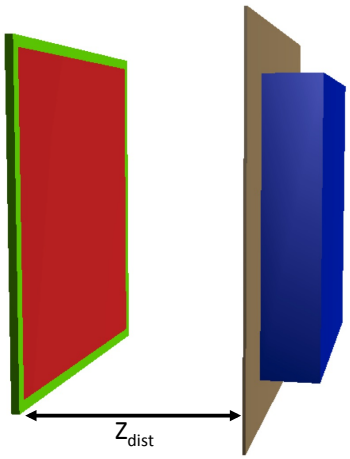

Figure 2.6: Simulated model of the ACT prototype. Separate elements are explained in the text.

- 2D position resolution in XY plane (50.8×50.8 mm^2); $1\sigma_X = 1\sigma_Y \approx 2.4$ mm;
- Depth of interaction (D.O.I.), along the thickness of the detector (10.0 mm), $1\sigma_Z = 2.1$ mm;
- Spectral resolution; FWHM = 3.5% at 661.7 keV;
- Trigger threshold = 15 keV.

The brown volume on Figure 2.6, is the aluminium plate of 0.5 mm thickness, which simulates the entrance window to the $LaBr_3$:Ce detector. The distance between the two main volumes, noted Z_{dist} on the Figure 2.6, is parameter with an effect on the overall performance results. We explored this dependency in a parametric study, presented later in this Chapter.

2.3.3 Simulated performance

The end result of creating MEGAlib simulations is to study and acquire essential performance values of a simulated instrument, which we can compare with the real measured data acquired with the prototype test bench. For this purpose we tested several key abilities by running simulations of our set-up. In Table 2.1 we report the performance of these simulation runs, where we tested the response on the variations of the Z_{dist} parameter. All simulated runs were performed with a collimated radioactive beam, simulated to mimic the one we used during measurements, with an energy of E_γ = 662 keV. The source was placed at the distance of $l = 15\ cm$ from the front side of the DSSSD volume, having a beam opening angle of $\sim 3^o$.

2.3.3.1 Spectral resolution

A typical energy spectrum, produced by one MEGAlib run, used to obtain the 1σ(E) values, is shown on Figure 2.7. The data on the Figure 2.7 represents the total of detected Compton events. The full energy peak, on the right, corresponds to the events in which the incident gamma-ray deposited its total ($E\gamma$ = 662 keV) energy within the prototype, while the data dispersed to the left, comes from events which made only partial energy deposits. From fitting the 662 keV peak we obtained the corresponding 1σ uncertainties, which are listed in the ΔE column of the Table 2.1. From here, we note the dependency of the energy resolution from the Z_{dist}. This is explained by noting several properties of our instrument. First, the DSSSD

Z_{dist}	**ARM FWHM**	**ΔE (1σ)**	**Compton Eff.**	**Full E peak Eff.**
(cm)	(degree)	(keV)	(%)	(%)
1	12.3	9.2	0.64	0.27
4	7.3	10.6	0.20	0.07
7	6	11.5	0.08	0.02
10	4.8	11.9	0.03	0.01

Table 2.1: Energy, angular resolution (ARM) and efficiency obtained with MEGAlib simulation runs using the geometry defined on Fig. 2.6. Each of the recorded values listed are explained in the text. We used a gamma-ray source with E = 662 keV. Furthermore, we varied the Z_{dist} parameter, assigning values of 1, 4, 7 and 10 cm.

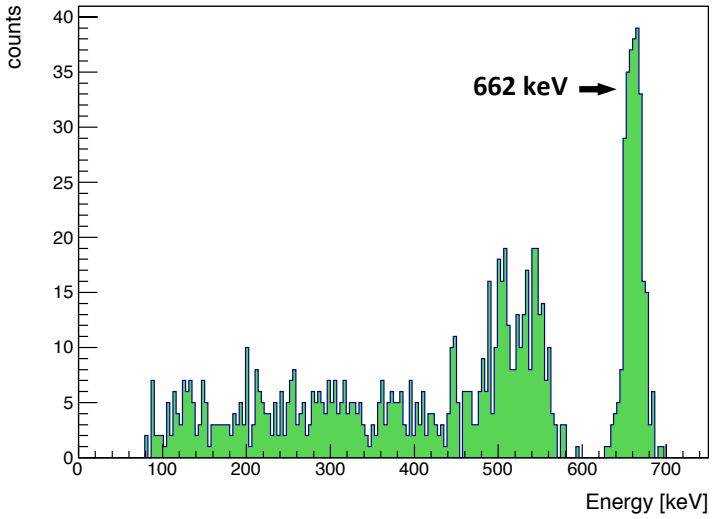

Figure 2.7: Reconstructed spectrum from the simulated data, implementing the prototype geometry with Z_{dist} = 10 cm. All of the counts correspond to detected Compton scattered photons, originating from a radioactive beam of Eγ = 662 keV. The events, which deposited the full energy in the detector are grouped in a noted 662 keV peak, while the uneven distribution to the left is from incompletely detected events. By using the implemented fit tools in MEGAlibg we placed a selection around the full energy peak and performed fitting, obtaining the width (1σ) of a Gaussian fit function.

detector has a better energy resolution than the $LaBr_3$:Ce scintillator; Second, the total energy of one event is calculated by summing up the energy deposits left in both the DSSSD and the calorimeter; Third, from equation 1.3 and Figure 1.10 (Chapter 1): the Compton scattering angle θ depends on the amount of energy a gamma-ray deposits during scattering in the DSSSD. Then, connecting the above: when the Z_{dist} value is lower the calorimeter is able to capture gamma-rays (coming from the DSSSD) with larger scattering angles, such events leave higher energy deposits in the DSSSD, which means that the precision by which we measure their total energies are higher, finally increasing the overall energy resolution; where the opposite is also true. Therefore, we have a spread of ΔE (Table 2.1) values from 9.2 keV to 11.9 keV, when Z_{dist} goes from 1 to 10 cm.

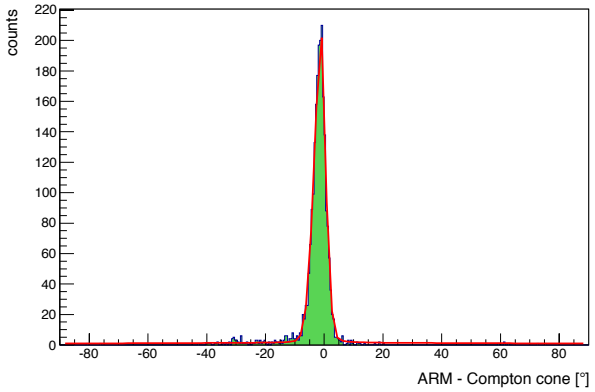

Figure 2.8: ARM spectrum obtained in MEGAlib after a selection on the full energy peak in the energy spectrum (Figure 2.7), with $E_\gamma = 662$ keV and Z_{dist} = 10 cm. The performed fit, from which we obtained the ARM(FWHM)=4.8^o value is noted in red, while the data is given in green.

2.3.3.2 Angular resolution

An example of simulated ARM spectrum, obtained in MEGAlib, is shown on Figure 2.8. The fit (noted in red on Fig. 2.8) is performed automatically in MEGAlib. It is a complex fit function consisting of two Lorentz functions and one asymmetric Gaussian, where right and left wings can have different sigmas (*Zoglauer et al.*, 2011). The FWHM values we obtained are presented in the ARM column of the Table 2.1. Decrease of the FWHM values for higher values of Z_{dist} is again explained by changes in detector geometry i.e. the spacing between the two detectors. As explained in Chapter 1, the ARM is a parameter which represents the precision with which we determine the point of origin of a detected gamma-ray. Therefore, by having a larger distance between the two key interaction points, a gamma-ray scattering location in DSSSD and a gamma-ray capture location in the calorimeter, we are able to better reconstruct their relative position. This directly influences the reconstruction of the scattering angle and the precision on the original position, which reflects in the ARM parameter.

2.3.3.3 Efficiency

Compton and full-energy-peak efficiency dependencies are expressed in the last two columns of the Table 2.1. The Compton efficiency is calculated as the ratio between the number of detected Compton scattering events $N_{scatt.}$ (total number of counts from Figure 2.7) and the known number of gamma-ray photons $N_{tot.}$ we generated from the radioactive source. In the same way, the full energy efficiency is the ratio between the number of Compton events which deposited their complete energy inside the detector N_{fullE} and $N_{tot.}$. In Figure 2.9, we show results from a broader efficiency study, using several different energies: 122 keV, 365 keV and 662 keV. The selected energies corresponding to the characteristic gamma-ray lines from: ^{57}Co, ^{133}Ba and ^{137}Cs sources, respectively. These runs are performed using the same geometry set-up (Fig. 2.6), with the same Z_{dist} variations. It is visible, as for previous values, that the efficiency is strongly dependent of the Z_{dist}, where the closer the two detector volumes are, the more Compton effects we are able to detect because we include Compton events with higher scattering angles, which leads to higher efficiency. In the opposite case, when the two layers are further apart, a lots of gamma-rays which scatter in the DSSSD miss the calorimeter, and are not detected as Compton events. Since both efficiencies are connected (the full energy events

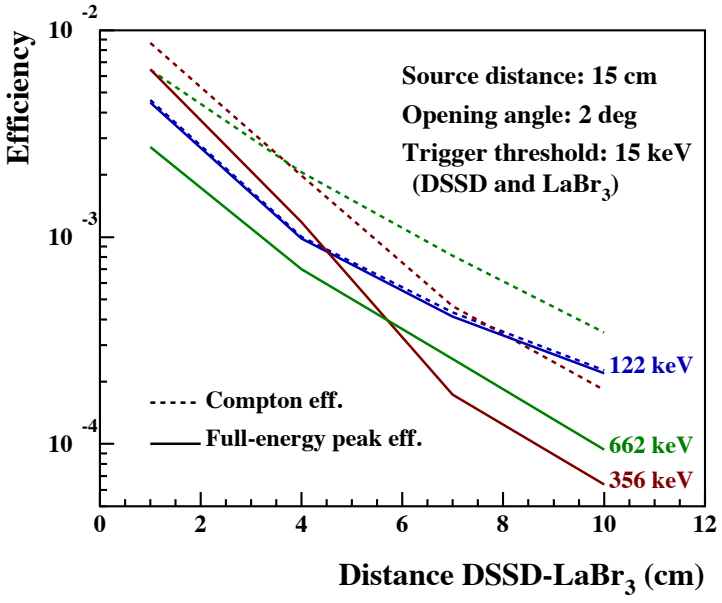

Figure 2.9: Efficiency study using MEGAlib simulations. We note the full-energy peak efficiency with full lines, and efficiency to detect Compton events with dotted lines, for three different source energies: 122 keV (in blue), 356 keV (in red) and 662 keV (in green).

are a part of the total Compton detected events), both express the same Z_{dist} dependency.

2.3.3.4 Compton Imaging

Finally, we show the ability to reconstruct a Compton image (Chapter 1) from the performed simulations, as shown on Figure 2.10. The images are obtained using automated imaging tools within MEGAlib. The utilized imaging algorithm is an iterative process called a List-Mode Maximum-likelihood Expectation-Maximization (LM-ML-EM) (*Zoglauer*, 2006).

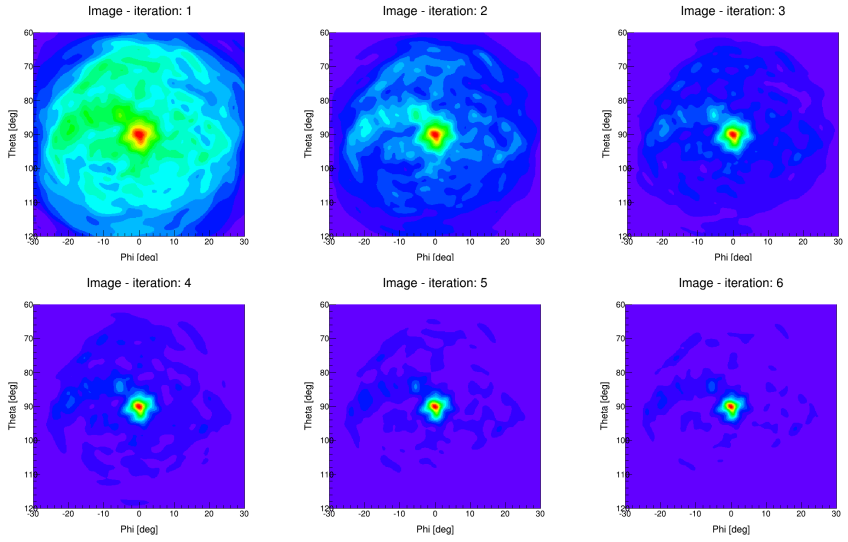

Figure 2.10: Compton Imaging performed with MEGAlib from the obtained simulated data with $E_\gamma = 662$ keV and $Z_{\mathrm{dist}} = 10$ cm. The top left image corresponds to the left image on the Fig. 1.13 (Chapter 1). The final outcome is improved over several iterations, where we note the limit of the method reached after the 4th iteration.

Chapter 3

Development of the Calorimeter testbench

3.1 General view of the test-bench

All experimental work regarding the 3D imaging module, intended as the calorimeter of the Advanced Compton Telescope (ACT) prototype, was carried out on a dedicated test-bench made and operated at CSNSM, Orsay. The setup used is shown on Fig. 3.1;

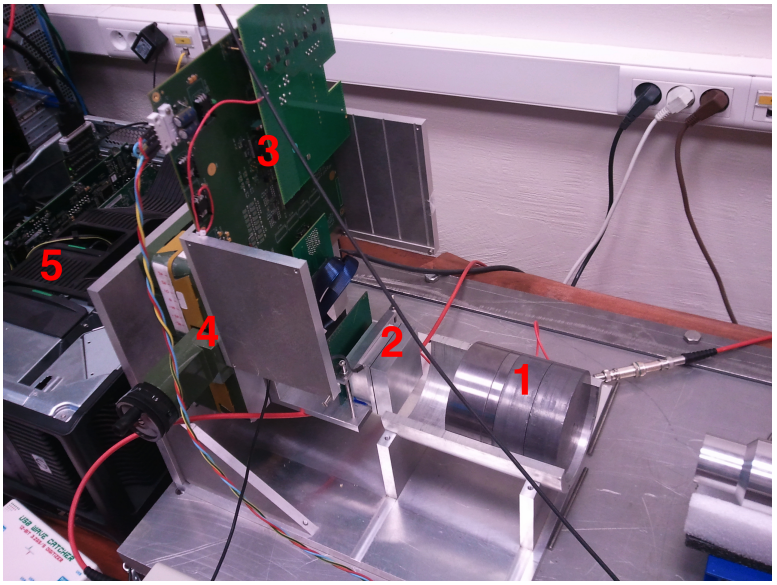

Figure 3.1: Detector test bench at CSNSM Orsay: 1. collimated radioactive source, 2. interchangeable detector module, 3. electronics board, 4. X–Y table, 5. PC.

The setup is shielded, from below with, 4 cm thick, lead bricks and an aluminum plate of 2.5 cm thickness to reduce the environmental background. The mechanical parts include: an X–Y table, holders for electronics board, a detector holder and two source cradles. The detector module was fixed onto the X–Y table, whose horizontal and vertical positions could be accurately adjusted with the help of threaded shafts in a range of about 15 cm. That enabled us to irradiate the full area of the front face of the detector crystal with fixed collimated sources in the front cradle (item 1 on Fig.3.1).The irradiation of the crystal side face was done using a second

cradle (not shown on Fig.3.1), placed perpendicular to the first one at adjustable distance from the detector.

We used several radioactive sources for the purpose of testing: ^{241}Am (430 kBq), ^{133}Ba (40 kBq), ^{137}Cs (4.5 kBq and 3.8 MBq) and ^{60}Co (34.8 kBq). These sources can be collimated with several copper and lead discs with a central hole of 3 mm diameter, which can be settled, together with the source holder disks, in one of the two (front and side) cradles. The sources can be placed at arbitrary distance from the detector.

We tested two detector modules, one with a cerium-doped lanthanum(III) bromide ($LaBr_3$:Ce) crystal and the other with cerium(III) bromide ($CeBr_3$). The two modules are interchangeable and fit in the same position within the bench.

3.2 $LaBr_3$:Ce detector module

A simple scheme of $LaBr_3$:Ce module is presented on Figure 3.2. The $LaBr_3$:Ce scintillator is an inorganic crystal produced by Saint-Gobain Crystals (model: BrillianCe^{TM} 380). The dimensions are: 5.08×5.08 cm^2 front surface and 1 cm thickness. Five sides of the crystal are ground and wrapped in Teflon in order to conserve the maximum of created optical photons. The crystal is hermetically sealed by an optical window made from borosilicate glass (0.5 cm thick with a refractive index $n = 1.472$), and both are encapsulated in an aluminium housing of 0.5 mm thickness. The surface of the crystal coupled to the optical window is polished. The optical window is coupled, via optical grease, to a multi-anode photomultiplier (MAPMT) of 64 (8×8) channels produced by Hamamatsu Photonics (model H8500C). The MAPMT anode gains provided by the manufacturer *Hamamatsu Photonics K.K.* (2011) are in the range: $(1.03 - 2.11) \times 10^6$ for a high voltage of 1000 V.

We first performed a radiography of the detector to check the dimensions of the $LaBr_3$:Ce crystal, from a scan of both the front and side faces of the module using the ^{241}Am collimated source. The crystal dimensions were estimated from the measured count rate as a function of the source position and were found to be consistent with the values provided by the manufacturer. In particular, from a fit of the count rate profile measured from the side, we obtained a crystal thickness of 10 ± 1 mm.

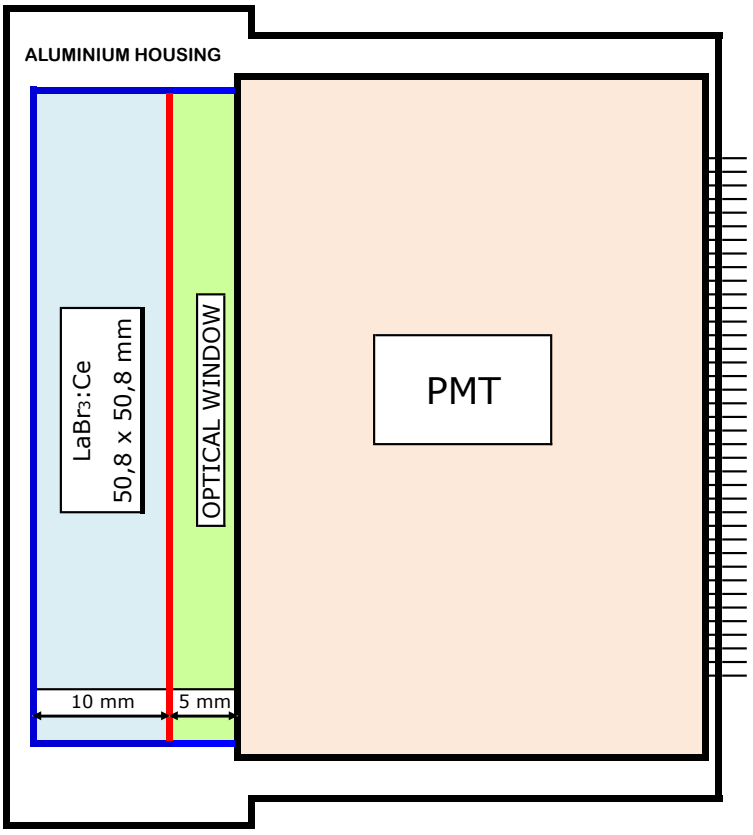

Figure 3.2: Schematic representation of main elements within the $LaBr_3$:Ce detector module. From left to right: $LaBr_3$:Ce crystal is coupled to a borosilicate glass optical window which on the other side connected to the 64 channel MAPMT. The elements are placed in an isolated aluminium protective box.

3.3 $CeBr_3$ detector module

The $CeBr_3$ scintillator (Fig. 3.3) is an inorganic crystal produced by SCIONIX (model V51C10-CeBr-X). The dimensions are: 5.1×5.1 cm^2 front surface and 1 cm thickness. Surfaces of the crystal are again ground and wrapped in Teflon to maximize the conservation of scintillation light. The crystal is coupled via a quartz optical window and, same as $LaBr_3$:Ce, hermitically sealed within a 0.5 mm thick aluminium box. The optical window is 0.15 cm thick, has a refractive index $n = 1.4585$, and is further coupled, using optical couplant Q2-3067 from Dow Corning, to another Hamamatsu 64 channel MAPMT (same model: H8500C). The coupling of this detector to the MAPMT was done at CSNSM. According to the manufacturer, the anode gains of this MAPMT are in the range: $(0.8 - 2.01) \times 10^6$ for a high voltage of 1000 V.

Figure 3.3: $CeBr_3$ module, with the scintillator crystal wrapped in reflective coating and placed in an air-tight enclosure within the aluminum casing. In front of the crystal is an optical window held by a hermetic seal. The module was later coupled, via the surface visible on the figure, to a MAPMT via optical grease.

3.4 Electronics and data acquisition

We used the same acquisition system to read out both tested detector modules.

The front-end electronics (FEE) are based on the latest version of the MAROC (Multi-Anode ReadOut Chip) ASIC (Application-Specific Integrated Circuit), which was initially developed by LAL laboratory (Laboratoire de l'Accélérateur Linéaire) for the LHC/ATLAS experiment at CERN (*Barrillon et al.*, 2006). The MAROC ASIC is a 64-channel input circuit of 4×4 mm^2 area based on AMS Si-Ge 0.35 μm technology, which provides 64 trigger outputs and charge measurement.

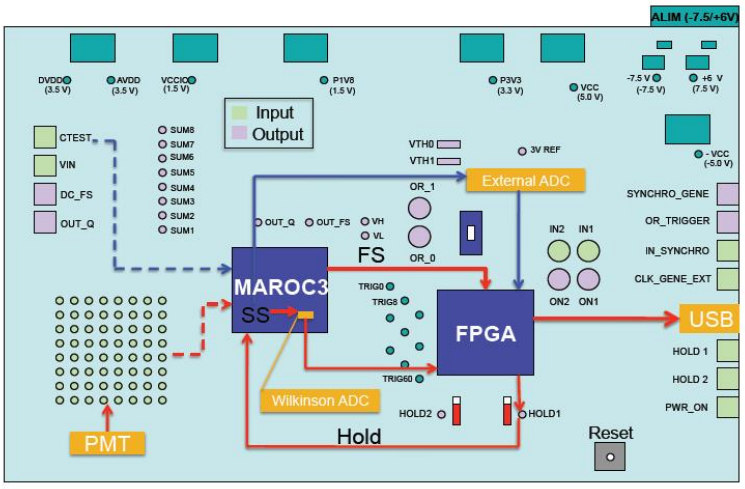

Figure 3.4: The schematic of the electronics test board used to read out the 64 channel MAPMT from the detector module.

In this work, we used the electronics board and associated LabVIEW software developed at

LAL for the chip characterization. This board comprised the following main elements (Figure 3.4):

- C test port: Entrance for input voltage that is used only for testing.
- PMT connector: 64 channels on the electronic board into which the pins of the MAPMT are plugged.
- ASIC MAROC: this contains a preamplifier, a fast shaper, a slow shaper, a discriminator and a multiplexer (see below).
- A digital to analog converter (DAC).
- An external ADC and an internal ADC (Wilkinson).
- An Altera Cyclone 1 FPGA (Field Programmable Gate Array).
- Hold switches, board reset, power supply and an USB port.

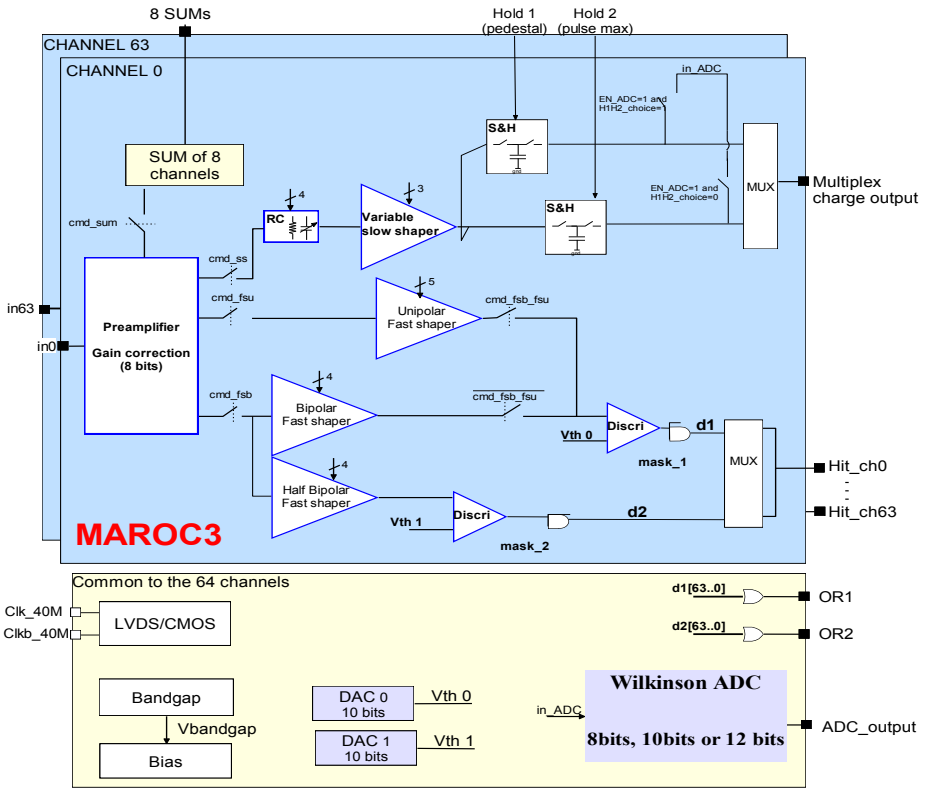

Figure 3.5: Block schematic of the MAROC chip architecture.

The ASIC MAROC is schematically presented in Figure 3.5. The 64 readout signals from the MAPMT are directly connected to the preamplifier input stage of the ASIC. The low impedance preamplifier has a variable 8 bit gain for each channel, which compensates the PM gain dispersion up to a factor of four. Next, each signal (from each channel) is lead to a fast shaper, which is used to generate a trigger signal when the level of the fast shaper goes above a programmable threshold. It is possible to choose between two fast shapers within MAROC: the first one is associated with a low offset discriminator and it allows 100% trigger efficiency rate for input signals close to 10 fC; the second one is a bipolar fast shaper with lower gain, which enables

triggering on higher input charge without saturation. The thresholds are set by two internal 10 bit DACs (Digital-to-Analog Converters). The ASIC also includes 64 slow shapers with independent variable slopes (50-150 ns) followed by two Track-and-Hold functions in order to provide a multiplexed analog charge output.

An external, global, hold signal, with a programmable delay is generated from the ALTERA FPGA (Fast Programable Gate Array) on the FEE board, using a Global Trigger signal, which is the OR signal of the 64 triggers coming out of the MAROC ASIC. The Hold signal from the FPGA (see Figure 3.4) then holds the slow shaper signal and keeps it available until it is digitalized either by a 12 bit Wilkinson ADC (Analog-to-Digital Converter) internal to the ASIC or by an external ADC on the FEE board. All of the results presented in this thesis were obtained using the external ADC. The creation of this digitally-controlled track-and-hold signal from the trigger output was the first step to transform the MAROC test board into an auto-triggered system of charge signal acquisition.

Two back-end electronics (BEE) and data acquisition systems were developed for this project. Initially, after the digitalization, the data were transferred to a PC via an USB connection and recorded with a LabVIEW software (*Gostojic et al.*, 2013). But the data acquisition rate was too limited with this system, being of the order of ten counts per second. So we developed a second system where the data is first stored into an ALTERA FIFO (First In First Out) memory and then transferred into a data merger board based on the Xilinx ML605 evaluation board equipped with a Virtex-6 FPGA. The data block is then time stamped and formatted, using MFM (MultiFrame Metaformat) data header, to a 64 signals data block to create an event data block. The event block is then transferred to a PC via a PCI Express interface. The online acquisition is based on a triggerless system which is controlled via graphical interface with a dynamic configuration based on the NARVAL[1] software. The acquisition system dead time was measured to be less then 20 μs. This system is now used to acquire data from the ACT prototype (Chapter 2), with the merging of the data, from the Tracker and the Calorimeter, being made in the Xilinx ML605 board.

3.5 Calibration of the acquisition system

In 2014, after updating the acquisition electronics to the current configuration, we performed a full calibration of the system. We based the method on experiences from calibrating the previous, LabVIEW-based version of the acquisition system. To generate the test signals we used a programmable pulse generator, ArbStudio 1102, from Teledyne LeCroy. It is an arbitrary waveform generator, with a sample rate of 1GS/s and which comes with a control software, allowing for a versatile choice of output signals. We use a high-precision capacitance, with a nominal accuracy of 1%, to transform the output voltage U from the generator into a charge q feeding the ASIC preamplifier, according to the well-known formula:

$$q = C_{\text{input}} \times U \ . \tag{3.1}$$

The capacitance was connected in series to a customized shielded cable, which was designed with a BNC (Bayonet Neill-Concelman) connector on one side, and a pin output on the other, allowing a direct connection to the MAPMT inputs on the electronics board.

Using the control LabVIEW application for the electronics board, we set the tunable gain of the MAROC preamplifier to an input value of 4 (DAC value) for all measurements. This

[1]See: https://forge.in2p3.fr/projects/ and *Grave et al.* (2005).

corresponds to an analog "gain" of $0.0625\ (= 1/16)$ for the input signal. Such a reduction of the MAPMT signals is needed, in order to match the ASIC bandwidth, which ranges from baseline to 15 pC for the unity analog gain. We adopted the capacitance value $C_{\mathrm{input}} = 273$ pF, which allows exploration of the full dynamics of the ASIC, with generator pulse amplitude ranging from 0 to 1 V.

In practice, using the ArbStudio software for the waveform generator, we created an input test sequence consisting of multiple square signals. In total, we had 28 different signals, with consecutive amplitude values of $U(\mathrm{in\ mV})$ = [10, 20, 30, 40, 50, 60, 70, 80, 90, 100, 150, 200, 250, 300, 350, 400, 450, 500, 550, 600, 650, 700, 750, 800, 850, 900, 950, 1000]. The duration of each signal was 100 μs in total, specifically 50 μs of full amplitude, followed by a null signal (zero amplitude) of 50 μs. To acquire statistics, each signal was repeated 250 times.

Afterwards, each of the 64 channels (channel numbering between 0 and 63) was fed by the described test sequence and as a result, we collected a set of output signals in the form of ADC (analog-to-digital converter) values. Each ADC value corresponding to one input signal (amplitude) from the sequence. We then determined the mean $\mathrm{ADC_m}$ and standard deviation σ_{ADC} for each of the ADC value distributions, and proceeded to fit the obtained $\mathrm{ADC_m}(q)$ data points with three separate functions: a third order polynomial function,

$$f_1(\mathrm{ADC_m}) = aq^3 + bq^2 + cq + d\ , \tag{3.2}$$

a sigmoidal function,

$$f_2(\mathrm{ADC_m}) = \frac{s_1}{1 + 10^{(s_2 - q)s_3}} \tag{3.3}$$

and for the highest values a linear function,

$$f_3(\mathrm{ADC_m}) = eq + f\ . \tag{3.4}$$

Here, a, b, c, d, e, f, s_1, s_2, and s_3 are the fitted function coefficients and q is the input charge. The function boundaries, named $B1$ and $B2$, were calculated for charge values of $q(B1) = 80$ pC and $q(B2) = 150$ pC. Examples of fit functions with fit residuals are shown in Figure 3.6 for four channels, where f_1, f_2, and f_3 are presented in orange, green, and blue, respectively.

Once obtained, we implemented the fitting data in our data analysis code. Starting from the known $\mathrm{ADC_m}(q)$ functionality (Fig.3.6), we implemented a routine which calculates the inverse dependency q($\mathrm{ADC_m}$). More specific, the routine is solving, for q taken as unknown, the three following equations (corresponding to the three fit functions f_1, f_2, and f_3):

$$0 = aq^3 + bq^2 + cq + (d - \mathrm{ADC_m}) \tag{3.5}$$

$$0 = \frac{s_1}{1 + 10^{(s_2 - q)s_3}} - \mathrm{ADC_m} \tag{3.6}$$

$$0 = eq + (f - \mathrm{ADC_m})\ . \tag{3.7}$$

A full cubic equation, given in the general form, as in eq. 3.5, has multiple different solutions (roots). The type of solutions can be determined by calculating the $discriminant\ \Delta$, which for the case of a third order polynomial is in the form:

$$\Delta = b^2c^2 - 4ac^3 - 4b^3d' - 27a^2d'^2 + 18abcd'\ . \tag{3.8}$$

Here, $d' = d - \mathrm{ADC_m}$ (see eq. 3.5). Depending on the Δ value, we have three possible cases: 1) $\Delta < 0$ – the cubic equation has one real and two complex solutions; 2) $\Delta = 0$ – a special case

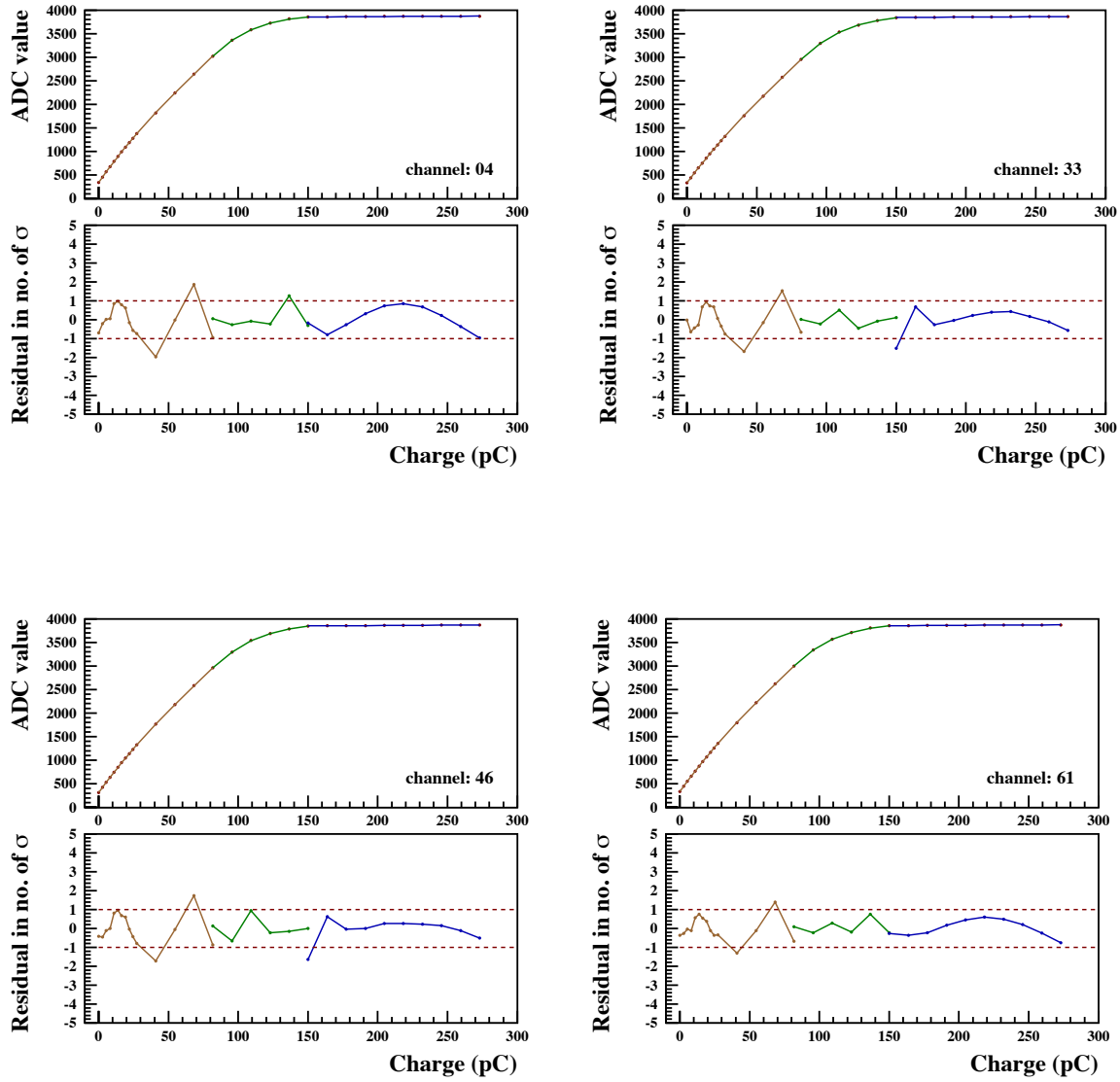

Figure 3.6: Examples of results used for the calibration of four different channels numbered: 04, 33, 46 and 61. *Top panels*: measured $\mathrm{ADC_m}(q)$ data points, presented as red dots, were fitted with three different functions: f_1 (eq. 3.2) in orange, f_2 (eq. 3.3) in green and f_3 (eq. 3.4) in blue. The functions are taken in intervals defined by borders $q(B1) = 80$ pC and $q(B2) = 150$ pC. *Bottom panels*: corresponding fit residuals for each of the three fit functions.

where all three roots are real and equal; and 3) $\Delta > 0$ – there are three, different real solutions. In our case, all of the coefficients a, b, c and d' are known from the fitting functions and for each of the fitted 64 channels they are similar and give a discriminant which is negative, thus we only needed to calculate the single real solution for the case of $\Delta < 0$:

$$q = -\frac{1}{3a}\left(b - C - \frac{\Delta_0}{C}\right), \tag{3.9}$$

with

$$C = \sqrt[3]{\frac{\Delta_1 + \sqrt{\Delta_1^2 - 4\Delta_0^3}}{2}} \,, \tag{3.10}$$

and

$$\Delta_0 = b^2 - 3ac \;\;,\;\; \Delta_1 = 2b^3 - 9abc + 27a^2d' \;\;, \text{ and } \;\; \Delta_1^2 - 4\Delta_0^3 = -27a^2\Delta \,, \tag{3.11}$$

where Δ is the discriminant given in equation 3.8.

Solving the inverse sigmoidal function, within the borders $B1$ and $B2$ is straightforward:

$$q = s_2 - \frac{\log_{10}\left(\frac{s_1}{\mathrm{ADC_m}} - 1\right)}{s_3} \,, \tag{3.12}$$

with s_1, s_2, and s_3 being known fit coefficients. Above the $B2$ border, the solution of equation 3.7 for q is also obvious:

$$q = \frac{\mathrm{ADC_m} - f}{e} \tag{3.13}$$

with known coefficients e and f.

Finally, by knowing all of the fit functions with their according inverse solutions, we are able to calculate any unknown charge deposit, and thus the corresponding energy, from the detected gamma-rays having the ADC values from the acquisition system.

3.6 Scanning measurements

We performed several series of measurements, with both detector modules, to study the localization of γ-ray hits within the crystals from measured distributions of the scintillation light. We used gamma-ray lines at 59.5 keV, ≈360 keV and 661.7 keV, from radioactive sources of ^{241}Am, ^{133}Ba, and ^{137}Cs, respectively[2]. The sources were placed inside the γ-ray collimator (see Fig. 1). In all these measurements, the front side of the collimator was located at ~ 1 cm from the front side of the detector module. Collimation was done with different materials for different sources: 1 Cu disk of 0.5 cm thickness for ^{241}Am, 2 disks of Pb of 2.85 cm thickness for ^{133}Ba and 3 Pb disks for ^{137}Cs. All the collimator disks have a central hole with a diameter of $d = 3$ mm, which gives a beam spot diameter of approximately 4.0, 3.4, and 3.2 mm for the three sources, respectively. The corresponding beam opening angle is of 17°, 2.85°, and 1.6° from the beam axis, respectively.

We scanned the surface of the detector by moving the mechanical holder with the detector in steps of ± 5 mm in front of the stationary collimated sources. We performed horizontal, vertical and diagonal series of measurements, starting from the central position (on the front face of the detector), noted by the coordinates $X_{\mathrm{POS}} = Y_{\mathrm{POS}} = 0$ mm. We later on used this data to compare two methods of position reconstruction: one based on an Anger logic algorithm and the other on an Artificial Neural Network (ANN, Chapters 5 and 6). An example of such measurements is given in Figure 3.7.

Furthermore, each measurement is corrected during the analysis for the non-uniformity of the MAPMT anodes. Each of the 64 MAPMT channels has a slightly different gain for which we had to compensate by adjusting the collected charge, using the anode non-uniformity matrix provided by the manufacturer (Hamamatsu) in the technical documentation (this correction is further discussed in Sect. 3.8 below). In Figure 3.8 we see an example of such correction on the overall distribution of the collected charge from one measurement run.

[2]The observed line at ≈360 keV from ^{133}Ba is composed of two lines at 356.0 and 383.8 keV, of relative intensity 62.05% and 8.94%, respectively.

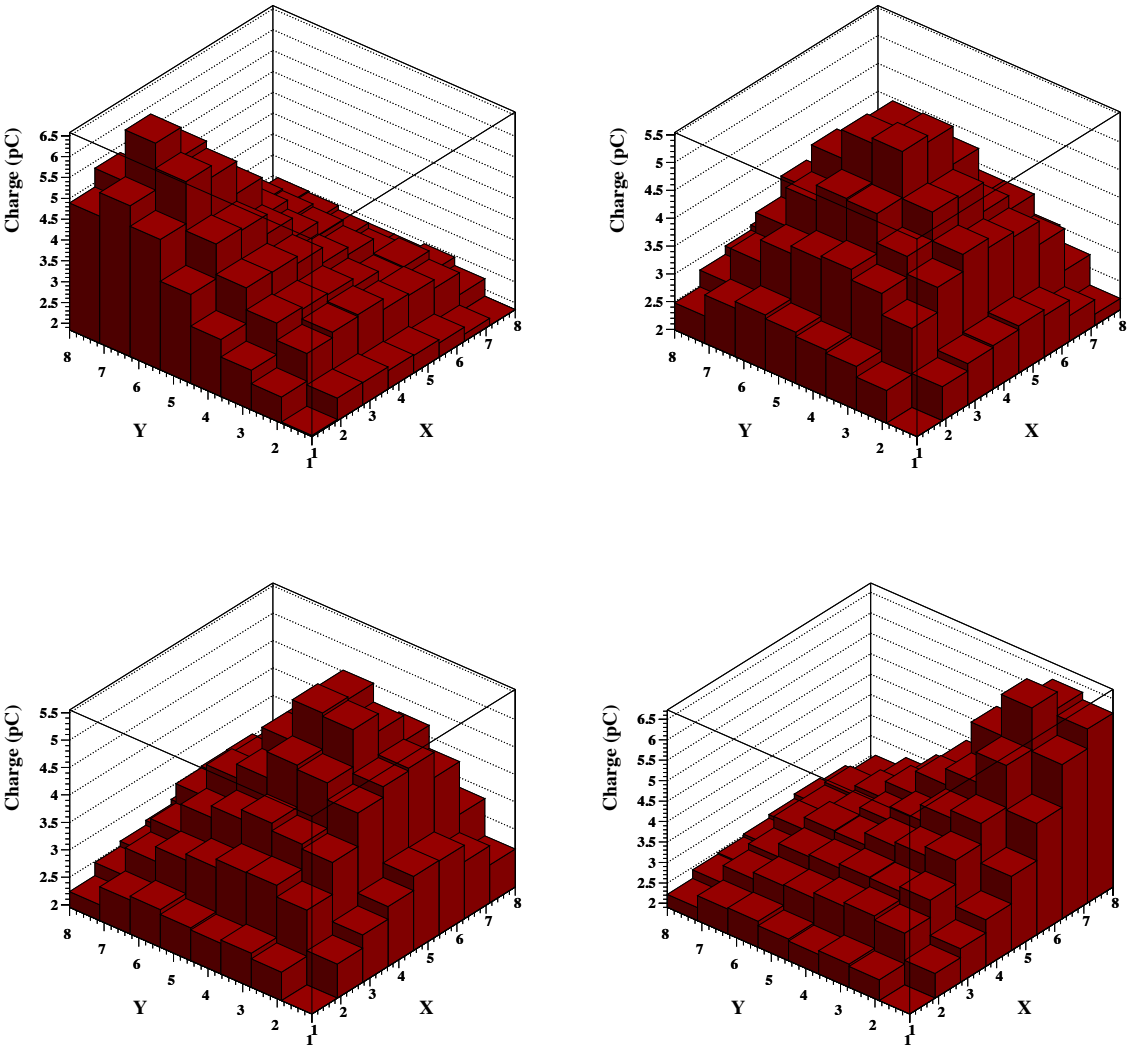

Figure 3.7: Charge distribution dependency on the radioactive beam position. All four cases are measured with a collimated ^{241}Am source and selecting the full energy 59.5 keV gamma-rays in the analysis. The respective beam positions, relative to the central position of the detector, are: $X_{\mathrm{POS}} = Y_{\mathrm{POS}} = -20$, $+00$, $+05$, and $+20$ mm, for each panel respectively, from the top left to the bottom right.

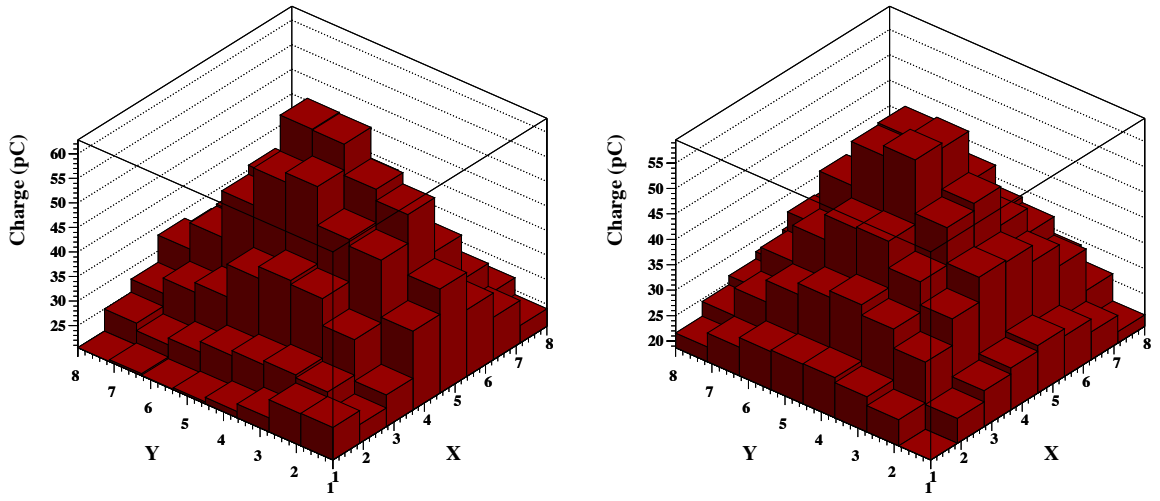

Figure 3.8: *Left*: Uncorrected total charge distribution over the 64 channels of the MAPMT. *Right*: After correction for the non-uniformity of the MAPMT anodes. Both panels correspond to the same measurement run, performed with collimated gamma-rays of 662 keV from a ^{137}Cs source. The beam is aimed at the central position of the $LaBr_3$:Ce detector, $X_{\mathrm{POS}} = Y_{\mathrm{POS}} = 0$ mm.

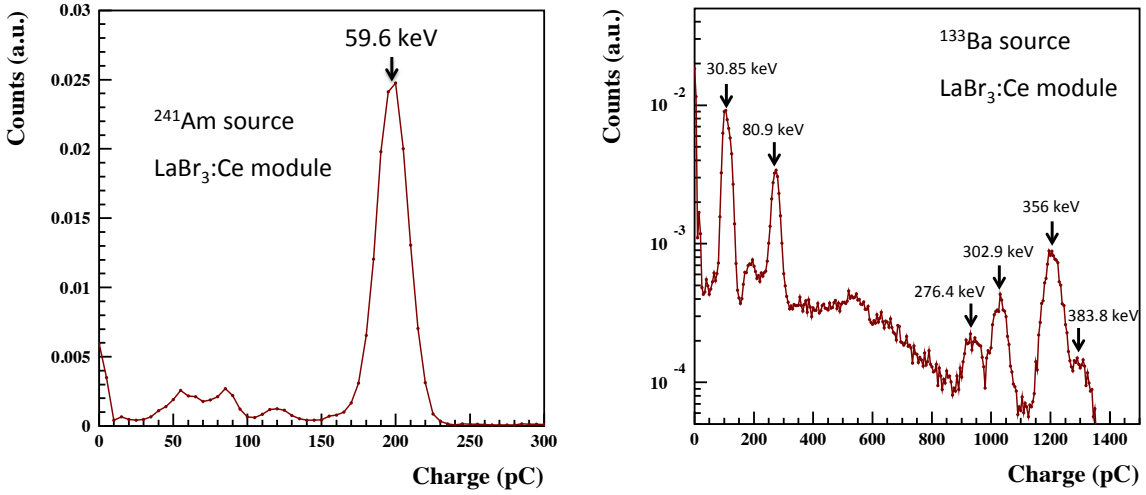

Figure 3.9: Two energy spectra, with marked energy peaks, obtained with the $LaBr_3$:Ce detector. *Left*: ^{241}Am radioactive source, in linear scale. *Right*: ^{133}Ba radioactive source, in logarithmic scale.

3.7 Energy measurements

To characterize the energy response of our detector modules, we used the three radioactive sources mentioned in the previous section (^{241}Am, ^{133}Ba, and ^{137}Cs), as well as a ^{60}Co source for the high-energy end of the explored range. To extend the energy calibrations to lower energies, we also used Ag X-rays induced by irradiation of a silver plate of 0.5 mm thickness by a slightly collimated source of ^{241}Am. The produced Ag fluorescence line emission results from the merging of the Ag Kα and Kβ lines at 22.1 keV and 25.0 keV, respectively. A complete list of radioactive sources with corresponding lines will be discussed in Chapter 6, when discussing the results. We performed some measurements with the γ-ray collimator, and others with uncollimated sources. Figure 3.9 shows examples of the full energy spectra obtained in these runs.

3.8 One photoelectron calibration

The purpose of the calibration of the MAPMT to one photoelectron (phe$^-$) was twofold: the first aim was to verify if the detection setup consisting of the MAPMT and the FEE board with the chosen parameters was able to provide a detection of 1 phe$^-$. Second, this calibration enables an independent check of the MAPMT anode uniformity as measured by Hamamatsu Photonics.

The measurements were made at the APC (AstroParticule et Cosmologie) laboratory, University Paris 7, in a black box regularly used for the calibration of optical modules of the ANTARES experiment (*Gauchet and Creusot*, 2012). The black box features a pulsed LED light source of near ultraviolet (UV) photons ($\lambda = 380$ nm) controlled by five motors to set position and direction of the photon beam, which had an opening of $\Delta\Theta = 5°$. The photon flux (pulse width of a few ns) can be adjusted with the help of a calibrated NIST diode attached to the light source. The light source pulse frequency was set to 100 kHz and the intensity to 0.05 photons per pulse. Such a low intensity results in a negligible probability of 2-and-more phe$^-$ events. Most of the pixel spectra were taken with both the local acquisition system and the prototype MAROC board. From the spectra, we obtain the value for quantum efficiency of the photocathode of approximately 25%, which is in agreement with the value of 27% provided by Hamamatsu Photonics.

We present in Figure 3.10 a comparison between measured gain values and values provided by Hamamatsu Photonics for 15 different pixels. The number of the chosen pixels is shown on the X-axis. We see that the relative gains we measured correspond reasonably well to the values given in the test sheet provided by the manufacturer, while there is a difference in absolute gains.

The gains provided by Hamamatsu Photonics (in red) were obtained with a PMT high voltage of HV $= 1000$ V and according to Hamamatsu data sheet (*Hamamatsu Photonics K.K.*, 2011), these values should be lower by a factor of approximately 1.7 than the values obtainable with the PMT high voltage of HV $= 1100$ V. However, we tested this by comparing our measurements, done with PMT high voltage of HV $= 1100$ V, with the Hamamatsu provided data and, as shown in Fig. 3.10, the difference is only by a factor of approximately 1.3.

We thus conclude that the total gain of the MAPMT is $\approx$25% lower than the value given in the test sheet provided by Hamamatsu Photonics, which can be explained by the different technique of measuring the gain by the manufacturer (measurement of the total current from bundling all 64 anodes produced by illumination of the MAPMT by a white light source).

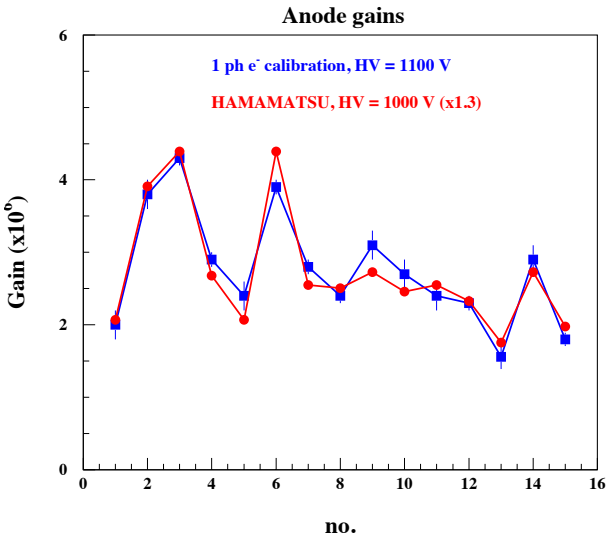

Figure 3.10: Result from one photoelectron calibration of the MAPMT. In blue is the measured gain for each of the anode (in total 15 different anodes out of 64), while in red are scaled ($\times 1.3$) values from the test sheet provided by Hamamatsu Photonics.

In this calibration, we also observed a cross-talk of about 10% between adjacent anodes of the MAPMT. This cross-talk probability is taken into account in the detector simulation presented in the next Chapter.

Chapter 4

Geant4 simulation of the Calorimeter modules

4.1 Introduction to Geant4

Geant4 is one of the most used toolkits for simulating the interaction of particles with matter. The wide range of options and functionalities, paired with a high level of customization, makes it adoptable to multitude of physics applications (nuclear and particle physics, medical and space science...). To begin, it comprises libraries of materials which allow the user to select or define properties of materials and create volumes of choice. This enables a complete modeling of any geometry used in real life experiments. Regarding the physics, it is possible to define all of the fundamental particles, e.g. by implementing Particle Data Group tables (*Olive and Particle Data Group*, 2014) and to take into account corresponding physical processes to describe interactions related to chosen particles. The Geant4 scope is valid in the energy range from 250 eV up to several PeV (10^{15} eV). In general, it is possible to choose within major groups of physical processes:

- Electromagnetic interactions
- Hadronic interactions
- Particle decay processes
- Gamma-nuclear and lepto-nuclear processes
- Optical photon processes

In addition, Geant4 includes two processes that deal with particle transportation and simulation parametrization.

Next, Geant4 is capable of generating primary processes and tracking the propagation of particles through matter and electromagnetic fields. It allows creation of sensitive detector elements and full visualization of the experimental experience. This includes creating the particles and following their trajectory through or recording their interactions with any simulated experimental geometry. Furthermore, Geant4 generates the event data and has the capability to store all the events and tracks. This means that it is possible to capture and analyze the data at any desired moment and with a very high level of details if necessary. Finally, Geant4 is created

and maintained by a worldwide collaboration which results in constant addition of new content and functionalities. It is used in different physics fields: nuclear physics, particle physics, astrophysics, accelerator and detector construction, medical physics and others. The software is object oriented and based on C++ programing language.

For this thesis we used the 4.9.4 version of Geant4. We created several Geant4 based simulations of the experimental set-ups we tested via the test bench at CSNSM. The need for such simulations was threefold. First, the simulation let us check our knowledge about the properties of the detector modules. Thus, we studied if inputing all known physical and optical properties of the scintillator in the simulation would give simulated results comparable to the measured ones. Second, having a precise simulation enabled us to perform various physical testings, which were practically impossible to perform in any other way. For example, to test the effect of the thickness of the optical window through which the scintillator is coupled to the MAPMT, it would require purchasing of 4–5 detector modules, each with different thickness of the window. Finally, we needed a large set of data in order to set up and prepare our Artificial Neural Network (ANN) software (Chapter 5). Such data set is experimentally hard to achieve, due to high statistics requirement, and physical and/or time limitations involved. For example, doing one measurement per each 1 mm^2 of the detectors surface, would require 2500 experimental runs. Therefore we decided for the option to simulate the required data.

4.1.1 Simulating optical light propagation and tracking

While preparing the project, we discussed several software options for simulating the optical photons and their behavior within the scintillator. A first option was to use $Litrani$ (*Gentit*, 2002) which is a Monte-Carlo tool for simulating light propagation in any type of geometry based on ROOT (*Brun and Rademakers*, 1997). Another option was to use GATE (*Jan et al.*, 2004), a toolkit focused on numerical simulation of various medical imaging techniques, such as: Emission Tomography (Positron Emission Tomography - PET and Single Photon Emission Computed Tomography - SPECT), Computed Tomography (CT), Optical Imaging (Bioluminescence and Fluorescence) and Radiotherapy experiments. However, as GATE is similar to Geant4 and implements Geant4 physics lists, and as Litrani lacks the ability to simulate the high-energy physics processes, we finally opted for Geant4 as the most versatile toolkit.

Big part of the Geant4 work was dedicated to selecting the best parameters to define the optical propagation of the scintillation light created in the scintillating $LaBr_3$:Ce and $CeBr_3$ crystals. This directly influences the output of the simulation and thus the compatibility of simulated and experimental results. The scintillation light in our detectors is near ultraviolet (UV) photons with wavelengths approximately between 300 and 400 nm. For such case Geant4 offers two different models: GLISUR and UNIFIED. Both are implemented within the toolkit and can be used to simulate the propagation, behavior and interactions of optical photons at the boundaries or borders of geometry volumes. Moreover, within these models, we can choose various different settings for the properties of interfaces between volumes and the behavior of optical photons at surface boundary. The nature of the interfaces between two volumes can be defined as $dielectric\_metal$ or $dielectric\_dielectric$. The $finish$ of a surface may be defined as $polished$ – perfectly smooth surface or as $ground$ – the surface is rough, covered with small irregularities (micro-facets). An example of $ground$ surface is shown on the right of Figure 4.1[1]. Even more specific for our case are the available options for the surface reflectivity, within the UNIFIED model. When a $ground$ surface option is selected, there are four sub-options to select a types of radiant intensity (*Gumplinger*, 2002):

[1]Image taken from: *OpenGATE Collaboration* (2014).

1. Specular lobe for reflection probability about the normal of micro facet;
2. Specular spike for reflection probability about the average surface normal;
3. Diffuse reflection for internal Lambertian reflection;
4. Backscatter for several reflections within a deep groove with the ultimate result of exact backscattering.

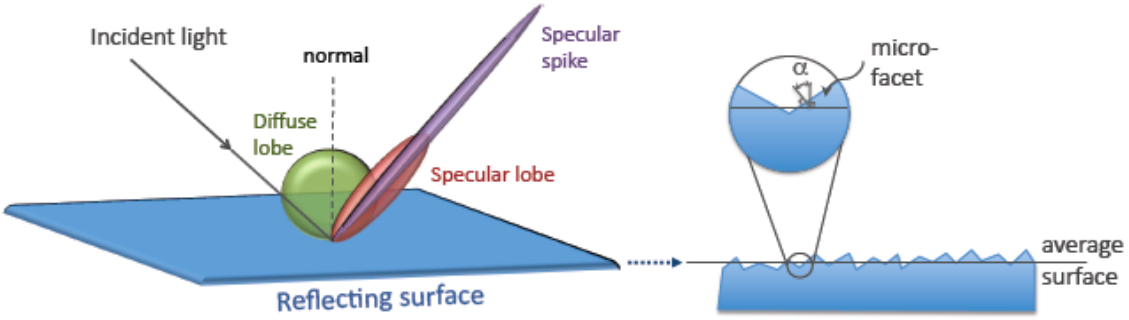

Figure 4.1: *Right*: representation of a ground surface with micro-facets. The inclination of each micro-facet is defined by the angle α from the normal of the average surface. *Left*: different cases of photon reflection as defined in the UNIFIED model. The *Lambertian* reflection is represented on the figure by the *Diffuse Lobe*. The *Backscatter* reflection is when the reflected photon propagates in the opposite direction from the *Incident light*.

All four cases are illustrated on the Figure 4.1. It is possible to mix several of these options at the same time with given probability. Further, the distribution/orientation of micro-facets (small imperfections or bumps on the surface) is defined through parameter named $SigmaAlpha$ (σ_α). Formally, σ_α is the standard deviation of a Gaussian distribution of the micro-facet orientations around the average surface normal (*Geant4 Collaboration*, 2013, Section 5.2.5). The angle α is defined on the right of Figure 4.1. Note that a surface defined as ground with $\sigma_\alpha = 0$ is equivalent to a polished surface. We use an additional parameter called $reflectivity$ in the tracking of optical photons, which defines light absorption at the surface and stands for the fraction of light that does not get absorbed (that is either reflected from or transmitted through the surface). Finally there are options for reflector coating: $backpainted$ or $frontpainted$, which can be combined with the $polished$ and $ground$ surface options.

4.2 Simulating the $LaBr_3$:Ce and $CeBr_3$ detector modules

We started by creating a very detailed simulation of a $LaBr_3$:Ce detector module and then later adjusted the simulation to be able to test the $CeBr_3$ module. In general, the simulation of our experimental setup includes: the γ-ray source, an optional adjustable γ-ray collimation, the detector module with the scintillator crystal coupled to an optical window, and a PMT volume with the photocathode inside. The simulation also includes the tracking of the scintillation photons produced in the crystal and, as mentioned above, a detailed parametrization to control this propagation. Additionally, first results, from the extensive simulation work, were previously presented in (*Gostojic et al.*, 2015).

4.2.1 $LaBr_3$:Ce simulation configuration

This section provides the main parameters and configuration we use to simulate the $LaBr_3$:Ce detector module. First, we create an $LaBr_3$:Ce crystal volume of 50.8×50.8 mm^2 area and 10 mm thickness, with the optical properties taken from (*van Dam et al.*, 2012). In particular, from these authors we use the experimentally determined mean refractive index of $LaBr_3$:0.5%Ce^{3+} as a function of wavelength (e.g. $n_m = 2.25$ at 380 nm). From this paper we also take the intrinsic emission spectrum of this material, as well as the attenuation, absorption and scattering lengths of the near-UV photons as a function of wavelength. The scintillation light yield of the crystal is set to 63 photons per keV, in accordance with the known light yield of the $LaBr_3$:Ce. The emission spectrum is defined from 320 to 420 nm, having a maximum at 360 nm. The absorption and reemission of the scintillation light are simulated with the Geant4 process developed to model Wavelength Shifting (WLS) fibers, attributing the WLS properties to the whole scintillator volume. The absorption and reemission spectra, together with the absorption length, are also taken from the publication of van Dam et al. (*van Dam et al.*, 2012). Light scattering within the scintillator volume is taken into account with the Rayleigh scattering process of Geant4 and the wavelength-dependent mean free path given in Ref. (*van Dam et al.*, 2012). The optical window is defined as a volume of glass with an index of refraction $n = 1.472$ for $\lambda = 380$ nm (private communication from Saint-Gobain Crystals).

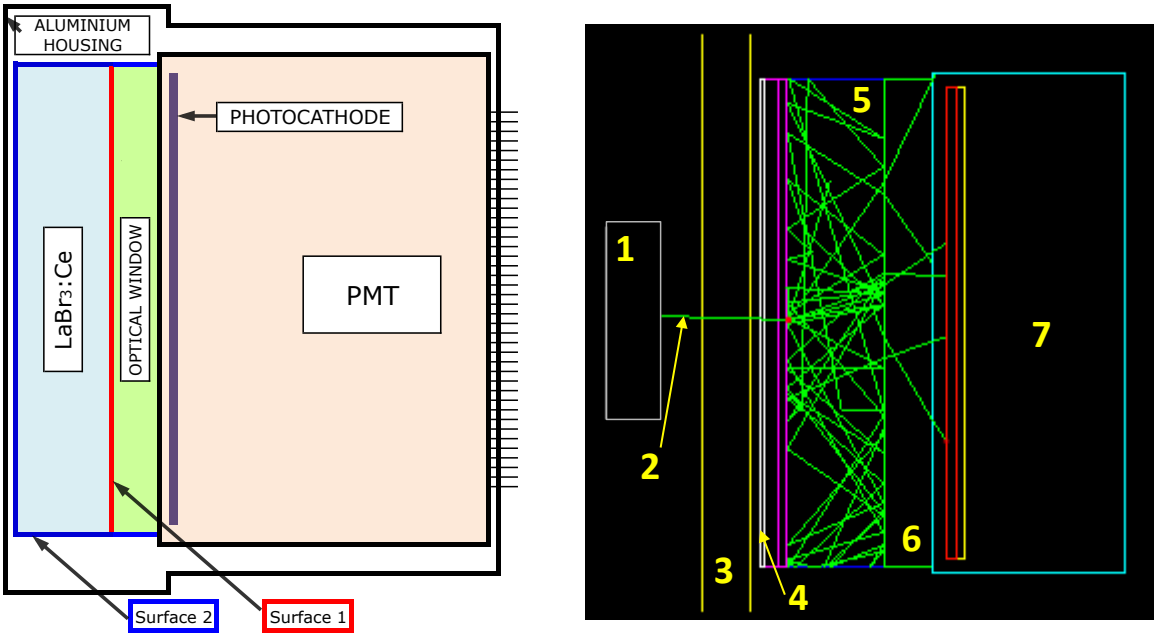

Figure 4.2: *Left*: Schematic representation of volumes and surfaces within the $LaBr_3$:Ce detector module: *Surface 1*, shown in red, is the coupling surface between the $LaBr_3$:Ce crystal and the optical window; *Surface 2*, shown in blue, includes the border sides of both the $LaBr_3$:Ce crystal and the optical window. *Right*: Image from Geant4 visualization with simulated elements: 1 – ^{241}Am radioactive source, 2 – radioactive beam, 3 – Cu collimator, 4 – aluminium entrance window modeling the aluminium housing, 5 – $LaBr_3$:Ce scintillator (with produced scintillation light in green), 6 – optical window, 7 – MAPMT volume with photocathode (red) and active detector volume (yellow). Note that, for clarity, we reduced the $LaBr_3$:Ce's light yield from 63 to 0.1 photons per keV, which resulted in detecting only 1 simulated photon.

All of the surfaces and borders were defined in our simulations through the UNIFIED model. The surface between the crystal and the optical window (hereafter "Surface 1"; see

Fig. 4.2) is set as $dielectric\_dielectric$ and $ground$, with $reflectivity = 1.0$ (i.e. 100% transparent).

The optical window is coupled to a PMT volume through a surface defined as: $dielectric\_dielectric$, $polished$, with $reflectivity = 0.97$. This value reflects the expected light transmission of the optical adhesive used by the manufacturer (Saint-Gobain Crystals, private communication). The PMT volume is a 52.0×52.0 mm^2 area and 20 mm thick cuboid made of borosilicate glass with an index of refraction: $n = 1.5$. The photocathode is modeled with a volume made of aluminium of 49.0×49.0 mm^2 area and 1 mm thickness, placed within the PMT glass volume, at 1.5 mm depth (from the side coupled to the optical window, see left panel on Fig. 4.2). The border sides of the crystal and the border sides of the optical window, represented in blue on the left panel of Fig. 4.2, are implemented into one group, named hereafter "Surface 2", and are considered to have identical optical properties, apart for the reflectivity. The crystal is wrapped in Teflon, for which we adopt a reflection coefficient of 97% (*Janecek*, 2012), while the optical window is surrounded by a hermetic seal of unknown composition, which we also define as Teflon in the simulation, but with 70% reflectivity (*see also: Ulyanov et al., 2013)*. Surface 2 is set as $dielectric\_dielectric$ and $groundbackpainted$.

The photocathode surface is simulated with a complex index of refraction in order to take into account the angular dependence of the photocathode reflectance and absorption. We use $n^\star(\lambda) = n(\lambda) + \mathrm{i}k(\lambda)$ with $n(\lambda) = 1.92$ and $k(\lambda) = 1.69$, which are the best-fit values obtained by *Motta and Schonert* (2005) for a bialkali KCsSb photocathode at the photon wavelength $\lambda =$ 380 nm. We further take the photoelectron efficiency to be $PE = 0.46$, which results in a mean (i.e. angle-averaged) quantum efficiency of ∼27% at 380 nm, as given by Hamamatsu Photonics for the MAPMT H8500C (*Hamamatsu Photonics K.K.*, 2011).

Given the above assumptions, the only remaining parameters that need to be defined are: the values of σ_α for the ($ground$) Surface 1 and Surface 2, and the type of reflection ($specularspike$, $specularlobe$, $Lambertian$, or $backscatter$) for Surface 2. These parameters were carefully studied from a comparison of simulated and experimental data.

4.2.2 Parametrization of the $LaBr_3$:Ce simulation

Two variables are used to compare quantitatively simulation and experimental results:

(a) Least squares (LS) is the sum of squares of differences between the simulated and experimental values of charge for each channel ($i = 1...64$), where the maximum values are normalized to 1.0. Similarly to *Garcia de Acilu et al.* (2012) we define:

$$LS = \sum_{i=1}^{64} [\frac{q_i^{\mathrm{exp}}}{q_{\mathrm{max}}^{\mathrm{exp}}} - \frac{q_i^{\mathrm{sim}}}{q_{\mathrm{max}}^{\mathrm{sim}}}]^2 \, . \tag{4.1}$$

Here, q_i^{exp} and q_i^{sim} are the charge values for one corresponding channel ($i = 1...64$) and $q_{\mathrm{max}}^{\mathrm{exp}}$ and $q_{\mathrm{max}}^{\mathrm{sim}}$ the maximum charge value for the experiment and simulation, respectively.

(b) Contrast is the ratio between the average value of the four channels (anodes) with most collected charge (q_i^{max}) and the average value of the eight channels with least collected charge (q_i^{min}):

$$Contrast = \frac{\sum_{i=1}^{4} q_i^{\mathrm{max}}/4}{\sum_{i=1}^{8} q_i^{\mathrm{min}}/8}. \tag{4.2}$$

We introduced the $Contrast$ parameter to compare simulations and experiments, because it was found to be more sensitive than LS parameter to the modeling of optical properties of surfaces in Geant4.

We ran a large number of simulations to study the optical properties of the border sides of the $LaBr_3$:Ce crystal and optical window (Surface 2), as well as the interface between the crystal and the optical window (Surface 1). In practice, we varied the two σ_α parameters of Surface 1 and 2 (SigmaAlpha 1 and SigmaAlpha 2) among seven values: 0.1, 0.3, 0.5, 0.7, 0.9, 5.0, and 10.0 rad[2]. We also considered the four possible types of reflection for Surface 2 ($specularspike$, $specularlobe$, $Lambertian$, or $backscatter$). Thus, for a given simulation setup defined by the characteristic energy of the gamma-ray source (^{241}Am, ^{133}Ba, ^{137}Cs) and the gamma-ray beam position (i.e. the values of $X_{\rm POS}$ and $Y_{\rm POS}$), there are $7 \times 7 \times 4 = 196$ possible combinations of parameters. We compared simulation results with measurements performed with the three radioactive sources for the three positions: $X_{\rm POS} = Y_{\rm POS} = 0$ mm, $X_{\rm POS} = Y_{\rm POS} = +15$ mm, and $X_{\rm POS} = Y_{\rm POS} = +20$ mm from the center of the crystal. The best simulated optical parameters were then found by computing the LS and $Contrast$ parameters, as well as the total simulated charge, and comparing them with the experimental values.

4.2.3 Simulation versus experiment for the $LaBr_3$:Ce detector

To compare the measured charge with the number of photoelectrons "detected" in the simulation, we took an overall PMT gain of $G_{\rm PMT} = 1.6 \times 10^6$, which is 24% less than the value given in the manufacturer test sheet (2.11×10^6). Such a gain reduction is consistent with the one-photoelectron calibration performed at the APC laboratory (Chapter 3). With the adopted PMT gain, the number of detected photoelectrons[3] for fully-absorbed 662-keV γ-rays from the ^{137}Cs source is $N_{\rm phe^-} = Q_{\rm mes}/(eG_{\rm PMT}) = 8837$, where $Q_{\rm mes} = 2265$ pC is the measured charge and $e = 1.602 \times 10^{-19}$ C. We can then compare the measured detector resolution, 3.6% FWHM at 662 keV (Chapter 6), with the expected, theoretical resolution (*Khodyuk et al.*, 2013):

$$R = \sqrt{R_M^2 + R_S^2}, \tag{4.3}$$

where R_M is the statistical contribution,

$$R_M = 2.35 \times \sqrt{\frac{1 + \nu(M)}{N_{\rm phe^-}}} = 2.8\%, \tag{4.4}$$

with $\nu(M) \sim 0.25$ the variance in the overall gain of the PMT, and R_S is the intrinsic resolution of the scintillator. We obtain from the measured resolution $R_S = 2.3\%$, which is consistent with the results of *Khodyuk et al.* (2013) and *Quarati et al.* (2013).

We first simulate the effect of 59.5 keV γ-rays from the ^{241}Am source. The reason to choose low-energy γ-rays to start with is because they produce less scintillation light within the scintillator, which significantly reduces the required computation time for tracking of the near-UV photons. At this energy, we tested the 196 possible combinations of parameters and systematically compared the simulation results to the experimental data. Examples of such parametrization test results are given in Figure 4.3, where we can see that the $specularspike$ reflection option provides a much better agreement with the data than the $backscatter$ option.

[2] Note that in general SigmaAlpha (σ_α) may take any value, as it is the standard deviation of a Gaussian, where SigmaAlpha = 10 rad corresponds to a nearly flat distribution.

[3] The number of photoelectrons produced by the interaction of scintillation photons with the PMT photocathode that reach the first dynode.

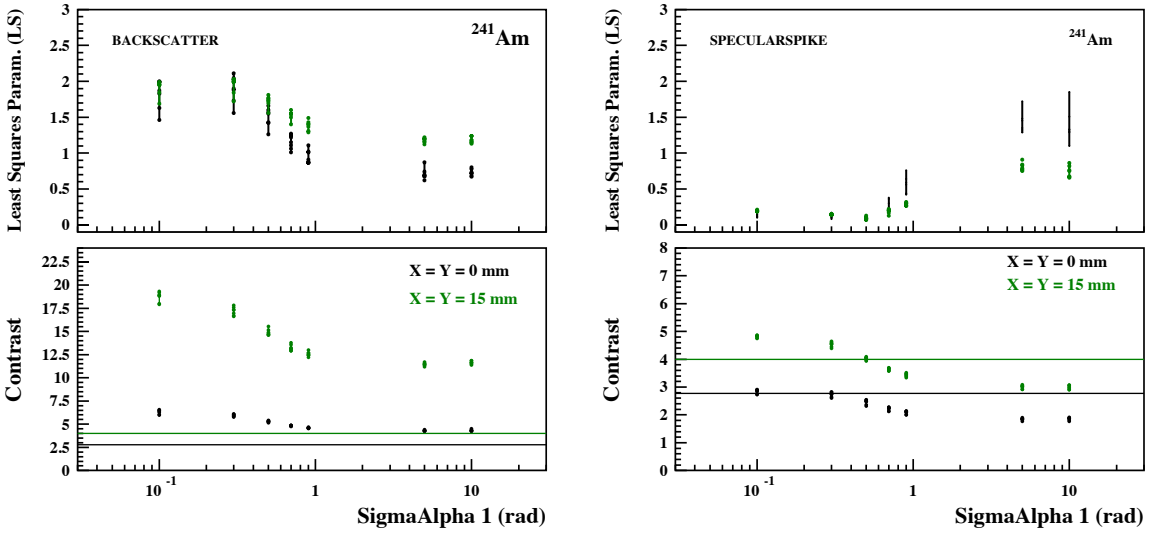

Figure 4.3: $Left$: LS and $Contrast$ parameters derived from Geant4 simulations with different combinations of σ_α and with the reflection type from the sides of the crystal and optical guide (Surface 2) set to be 100% $backscatter$. The horizontal lines in the lower panels show the values of $Contrast$ from the experimental measurements, for the two beam positions. Vertical data lines with points, corresponding to simulated data, show the variation depending on different values of SigmaAlpha 2 (the σ_α parameter for the border sides of the crystal and optical window). SigmaAlpha 1 is the σ_α parameter for the interface between the crystal and the optical window. Data points corresponding to beam positions $X_{\rm POS} = Y_{\rm POS} = 0$ and $+15$ mm are given in black and green, respectively. All simulations and measured data are for 59.5-keV γ-rays from the ^{241}Am source. $Right$: Same as on the left panel, but for the reflection type from Surface 2: 100% $specularspike$.

Thus, the minimum least-squares parameter for the $specularspike$ case is $LS_{\rm min} = 0.06$ for $X_{\rm POS} = Y_{\rm POS} = 0$ mm and $LS_{\rm min} = 0.07$ for $X_{\rm POS} = Y_{\rm POS} = +15$ mm, both values being obtained with SigmaAlpha $1 = 0.5$ rad (the dependency of this result with SigmaAlpha 2 is negligible), while for the $backscatter$ case $LS_{\rm min} = 0.62$ and 1.13 for the two positions, respectively. Furthermore, we see that the $specularspike$ option with SigmaAlpha $1 = 0.5$ rad gives a good match to the measured $Contrast$ for the two tested positions. This is not the case with the $backscatter$ option, for which the simulated contrast for $X_{\rm POS} = Y_{\rm POS} = +15$ mm significantly overestimates the measured value (minimum $Contrast = 11.2$ for the simulation whereas $Contrast = 4.02$ for the experiment).

Figure 4.4 shows the results obtained when setting the reflection type from Surface 2 as $Lambertian$ (*left panel*) and $specularlobe$ (*right panel*). By studying the least-squares parameter for these two options, we can first note that for the $specularlobe$ option, the LS values strongly depend on SigmaAlpha 2 for $X_{\rm POS} = Y_{\rm POS} = +0$ mm, ranging from ~ 1 up to ~ 6, when SigmaAlpha 1 > 5 rad. Contrary, this dependency is negligible for the case when $X_{\rm POS} = Y_{\rm POS} = +15$ mm (which on its own would be a fairly good result, but however we needed of course an option to work for any beam position). On the other hand, the LS parameters obtained with the $Lambertian$ option are systematically lower then $LS = 2$, for both beam position, and in addition, they converge to a minimum for values of SigmaAlpha 1 = 0.7 and 0.9 rad. The overall minimum values for $Lambertian$, $LS_{\rm min} = 0.04$ for $X_{\rm POS} = Y_{\rm POS} = +0$ mm and $LS_{\rm min} = 0.09$ for $X_{\rm POS} = Y_{\rm POS} = +15$ mm, are comparable with minimum values obtained with the $specularspike$ option, as the lowest values with best consistency. The $Contrast$ distri-

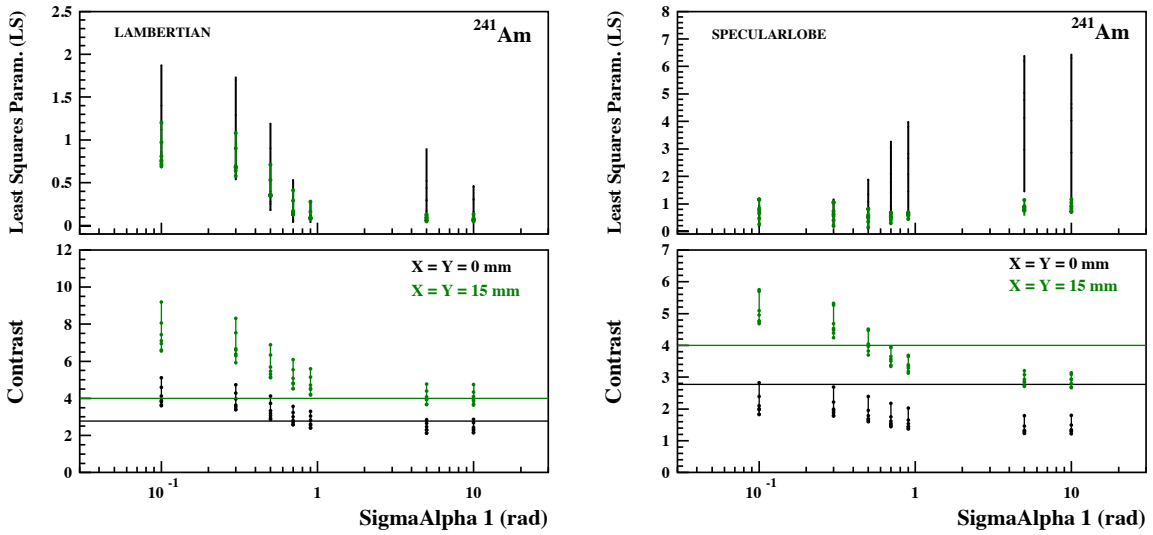

Figure 4.4: Same as Figure 4.3, but for the reflection type from Surface 2: 100% $Lambertian$ (*left panel*) and 100% $specularlobe$ (*right panel*).

butions for both $Lambertian$ and $specularlobe$ are similar, with $Lambertian$ (*left panel on Fig.4.4*) values being slightly higher. Nevertheless, for $Lambertian$ case, when SigmaAlpha 1 > 0.7 rad, we see good matching with the experimental values ($Contrast_{\rm exp} = 2.77$ for the beam position $X_{\rm POS} = Y_{\rm POS} = +0$ mm and $Contrast_{\rm exp} = 4.02$ for $X_{\rm POS} = Y_{\rm POS} = +15$ mm). For the cases when Sigma Alpha 1 > 5 rad, we obtain, for SigmaAlpha 2 = 0.3 rad, $Contrast_{0mm} \approx 2.66$ and $Contrast_{+15mm} \approx 4.37$, or for SigmaAlpha 2 = 0.5 rad $Contrast_{0mm} \approx 2.45$ and $Contrast_{+15mm} \approx 4.09$, all of which are within 12% error comparing to the measurements.

In summary, from this set of simulations, we find acceptable combinations of parameters with the $specularspike$ and $Lambertian$ options, but not with the $backscatter$ and $specularlobe$ options.

We then study the $specularspike$ and $Lambertian$ options for fully-absorbed γ-rays of 356 keV (^{133}Ba source) and 662 keV (^{137}Cs source). Contrary to the γ-rays emitted by the ^{241}Am source, which are mostly absorbed within the first millimeters of the $LaBr_3$:Ce crystal, those of 356 and 662 keV have sufficient energy to penetrate the full volume of the crystal. Results for the ^{133}Ba source are shown in Figure 4.5. The left panels show the LS and $Contrast$ parameters as a function of $\mathrm{SigmaAlpha\ 2}$ in the $Lambertian$ case, and for a fixed value of $\mathrm{SigmaAlpha\ 1} = 10$ rad (see footnote[2]), which is the best-fit value obtained from the simulations at 59.5 keV.

The right panels of Figure 4.5 show the $specularspike$ results as a function of SigmaAlpha 1, for $\mathrm{SigmaAlpha\ 2} = 10$ rad. We see that in the $Lambertian$ case, for $\mathrm{SigmaAlpha\ 2} \sim 0.5$ rad the simulated contrast is in fair agreement with the measured one for $X_{\rm POS} = Y_{\rm POS} = 0$ and $+15$ mm, but it slightly overestimates the experimental result for $X_{\rm POS} = Y_{\rm POS} = +20$ mm ($Contrast = 4.5$ and 3.5 for the simulation and measurement, respectively). In the $specularspike$ case (right panels), the experimental contrast for the most extreme beam position can be reproduced with a high value of SigmaAlpha 1, but the simulation of the central position is then bad (see the high values of the LS parameter for $\mathrm{SigmaAlpha\ 1} = 5$ and 10 rad).

From a detailed examination of all available data, we finally selected two possible combinations of simulation settings giving us reasonable results.

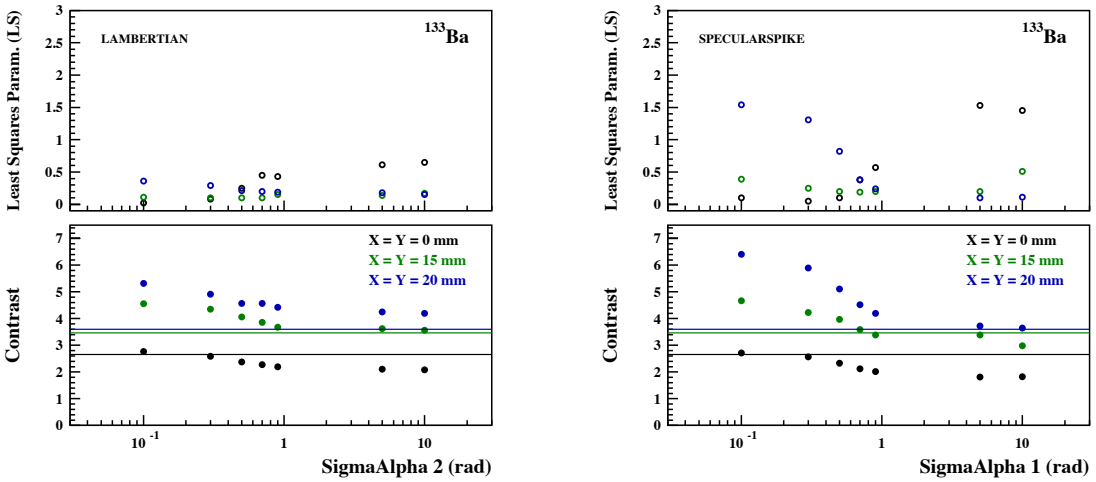

Figure 4.5: $Left$: LS and $Contrast$ parameters as a function of SigmaAlpha 2 (the σ_α parameter for the border sides of the crystal and optical window in the Geant4 simulation), for $\mathrm{SigmaAlpha\ 1} = 10$ (the σ_α parameter for the interface between the crystal and the optical window) and the reflection type from Surface 2 set to be 100% $Lambertian$. The horizontal lines in the lower panel show the measured $Contrast$ for the three beam positions. Simulated data points corresponding to beam positions $X_{\mathrm{POS}} = Y_{\mathrm{POS}} = 0$ mm/+15 mm/+20 mm are given in black,green and blue, respectively. All simulations and data are for 356-keV γ-rays from the ^{133}Ba source. $Right$: LS and $Contrast$ parameters as a function of SigmaAlpha 1, for $\mathrm{SigmaAlpha\ 2} = 10$ and the reflection type from Surface 2 set to be 100% $specularspike$.

- "Simulation 1" uses the $specularspike$ reflection type from Surface 2 with $\mathrm{SigmaAlpha\ 1} = 0.5$ rad and $\mathrm{SigmaAlpha\ 2} = 10$ rad.
- "Simulation 2" uses the $Lambertian$ reflection type from Surface 2 with $\mathrm{SigmaAlpha\ 1} = 10$ rad and $\mathrm{SigmaAlpha\ 2} = 0.6$ rad.

Table 1 summarizes the simulated and experimental results for these two best simulation configurations. We see that Simulation 1 reproduces the measured total charge within a few percent for all γ-ray energies and beam positions. But it significantly overestimates the measured contrast for the beam position $X_{\mathrm{POS}} = Y_{\mathrm{POS}} = 20$ mm (by a factor of 1.3, 1.5, and 1.6, for the ^{241}Am, ^{133}Ba and ^{137}Cs sources, respectively). Simulation 2 provides a better overall matching for the contrast. But it systematically underproduces the measured charge by 15–20%.

Figure 4.6 shows a comparison of simulated and measured distributions of charges for fully-absorbed 662-keV γ-rays irradiation of the LaBr$_3$:Ce detector at the position $X_{\mathrm{POS}} = Y_{\mathrm{POS}} = +15$ mm. We applied to the measured charge distribution a correction for the non-uniformity of the gain of the PMT anodes, for which we use the response matrix provided by Hamamatsu Photonics. We see that the agreement between the theoretical and experimental results is good for both simulations, although Simulation 2 underproduces the measured total charge by $\sim 17\%$.

4.2.4 Simulation of the CeBr$_3$ detector

To simulate the CeBr$_3$ detector, we start from the LaBr$_3$:Ce simulation and redefine the geometry and some physical parameters of the materials to match the new module. The optical and

Detector: $LaBr_3$:Ce		Charge [pC]			Contrast		
Source	Beam Position [mm]	Experiment	Simulation 1	Simulation 2	Experiment	Simulation 1	Simulation 2
^{241}Am	+00, +00	198	200	168	2.77	2.36	2.46
	+15, +15	190	196	162	4.02	3.93	4.06
	+20, +20	189	195	160	4.06	**5.22**	4.74
^{133}Ba	+00, +00	1186	1200	996	2.68	2.34	2.31
	+15, +15	1158	1190	968	3.48	3.93	3.83
	+20, +20	1134	1176	951	3.46	**5.14**	**4.52**
^{137}Cs	+00, +00	2234	2250	1867	2.61	2.25	2.39
	+15, +15	2174	2190	1814	3.26	4.10	3.93
	+20, +20	2148	2184	1785	3.25	**5.12**	**4.61**

Table 4.1: Comparison between experimental data and two Geant4 simulations (see Sect. 3.4) for the $LaBr_3$:Ce detector. The selected γ-ray energies are: 59.5 keV (^{241}Am), 356 keV (^{133}Ba) and 662 keV (^{137}Cs). The γ-ray beam position is given as the distances X_{POS} and Y_{POS} from the center of the detector. The simulated contrast values in bold are those differing by more than 25% from the experimental ones.

Detector: $CeBr_3$		Charge [pC]			Contrast		
Source	Beam Position [mm]	Experiment	Simulation 1	Simulation 2	Experiment	Simulation 1	Simulation 2
^{241}Am	+00, +00	138	157	144	3.17	3.66	3.78
	+15, +15	131	152	138	4.21	**6.45**	**7.11**
	+20, +20	129	150	134	5.03	**9.03**	**9.20**
^{133}Ba	+00, +00	881	941	860	3.34	3.62	3.64
	+15, +15	855	923	828	4.26	**6.43**	**6.80**
	+20, +20	828	901	802	4.54	**8.98**	**8.66**
^{137}Cs	+00, +00	1647	1760	1596	2.75	**3.56**	**3.56**
	+15, +15	1619	1714	1537	3.33	**6.38**	**6.59**
	+20, +20	1589	1674	1497	3.41	**8.85**	**8.34**

Table 4.2: Same as Table 1, but for the $CeBr_3$ detector.

physical properties of $CeBr_3$ are taken from *Quarati et al.* (2013), *Drozdowski et al.* (2008) and *Schotanus* (2015). The light yield is set to 45 photons per keV, acquired from *Quarati et al.* (2013) as it also relates to the $CeBr_3$ crystals grown by the same manufacturer as the one we use. While some sources (*Wei et al.*, 2014; *Hellma Materials GmbH*, 2014) report higher values for the light yield of $CeBr_3$, we found the value of 45 photons per keV, approximately 25% less than that of $LaBr_3$:Ce (*Drozdowski et al.*, 2008), to be in good agreement with the total charges we obtain from the measurements. The maximum of emission spectrum is at 370 nm. Additionally, due to the lack of measured data in literature, we adopt the absorption and reemission spectra of the optical light measured for the $LaBr_3$:Ce crystal *van Dam et al.* (2012). These mechanisms are simulated using WLS shifting fibers option in Geant4. Likewise, we use the same values for the absorption length as for $LaBr_3$:Ce simulation. The $CeBr_3$ crystal volume is again coupled to the optical window via Surface 1, but now the optical window is a 1.5 mm thick quartz with a refractive index of $n = 1.4585$. Surface 2, the photocathode and the crosstalk between PMT anodes are defined the same as for $LaBr_3$:Ce. Additionally, we estimate the total gain of the MAPMT the same way we did it for $LaBr_3$:Ce: we reduce the gain value of 2.01×10^6 provided by Hamamatsu by 24%, which gives us a PMT gain of 1.53×10^6.

For the $CeBr_3$ detector, we do not study in detail the optical properties of Surfaces 1 and 2, but adopt the two best simulation configurations found previously for the $LaBr_3$:Ce detector. The corresponding results for the $CeBr_3$ module are given in Table 2. We see that the two simulations reproduce well the measured total charge, with a slight overproduction of 5–15% in the

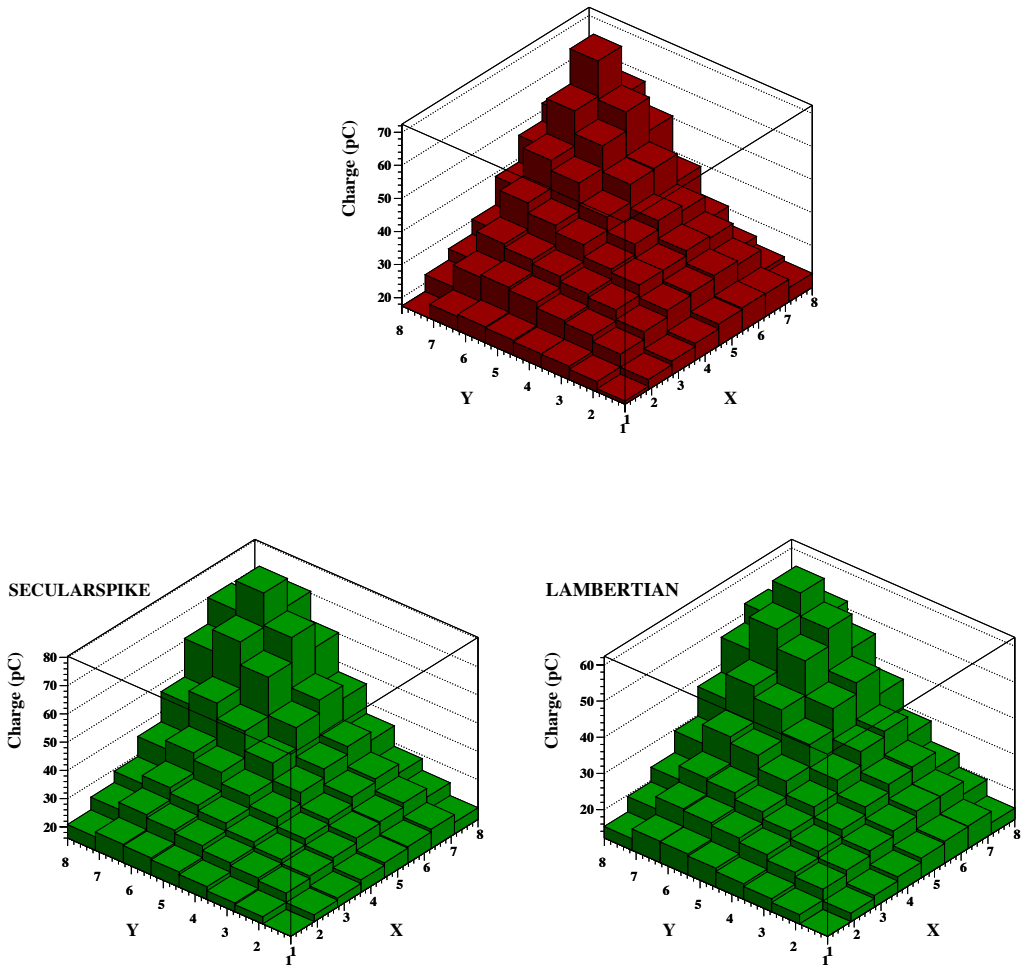

Figure 4.6: Comparison of (top) measured and (bottom) Geant4 simulated distributions of charges for the $LaBr_3$:Ce detector, and for fully-absorbed 662-keV γ-rays emitted by a collimated ^{137}Cs source pointing at the position from the detector centre $X_{\rm POS}$=$Y_{\rm POS}$=+15 mm. The bottom left panel shows the simulated distribution for the $specularspike$ case of "Simulation 1", while the bottom right panel is for the $Lambertian$ case of "Simulation 2" (see text). The measured total charge is Q_{exp}=2174 pC, while the simulated ones are Q_{sim}=2190 and 1814 pC for Simulations 1 and 2, respectively (see Table 1).

first configuration, and within $\approx$ 5% for the second. Concerning the shape of the distribution, we have fair results for the central position of the γ-ray beam, with less than 30% difference for the $Contrast$ parameter compared to the experiment. But the agreement between the simulation and the experiment is not as good for the off-center positions ($X = Y = +15/+20$ mm), where the simulated contrast can be up to a factor of 2.5 higher than the measured value. This can be improved in the future by studying in more detail the optical properties of the module at surface boundaries and the corresponding parametrization in Geant4. Graphical examples of measured and simulated charge distributions for the $CeBr_3$ module are given in Figure 4.7.

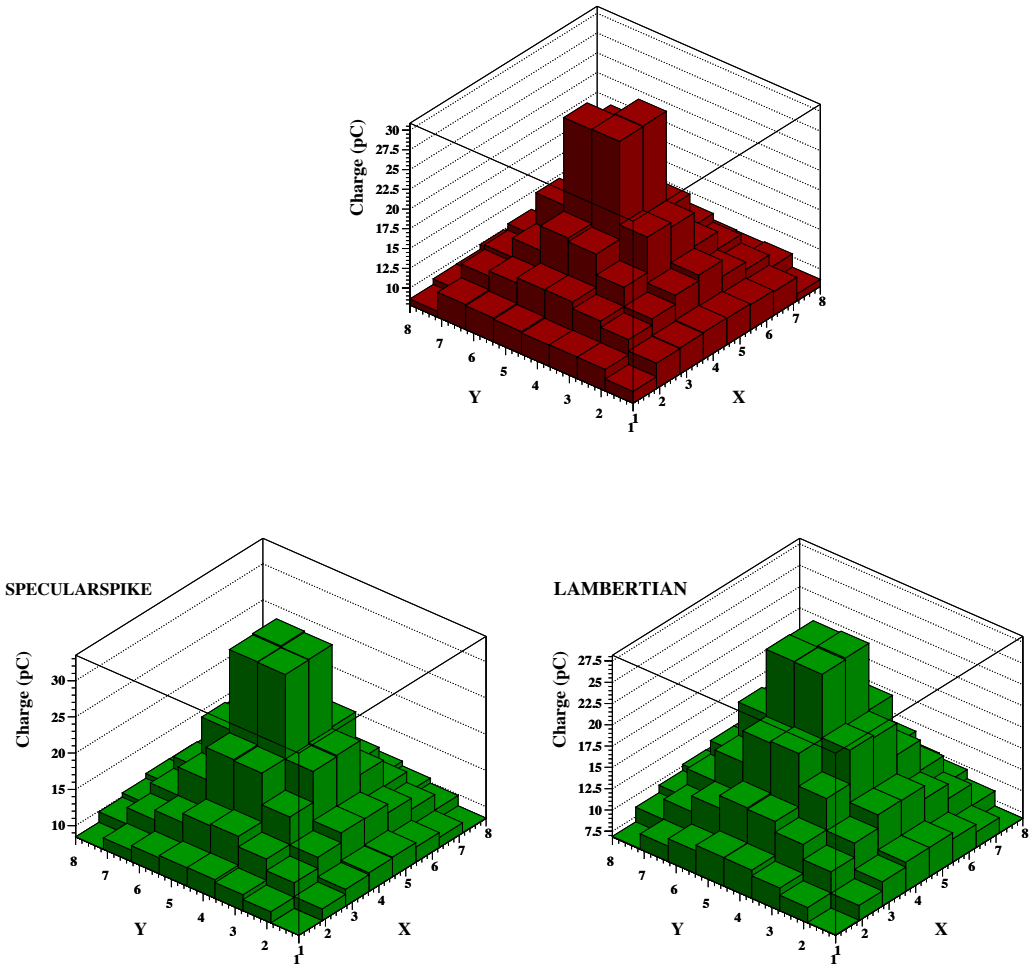

Figure 4.7: Comparison of (top) measured and (bottom) Geant4 simulated distributions of charges for the $CeBr_3$ detector, and for fully-absorbed 356-keV γ-rays emitted by a collimated ^{133}Ba source pointing at the detector centre ($X_{\rm POS}$=$Y_{\rm POS}$=0 mm). The bottom left panel shows the simulated distribution for the $specularspike$ case of "Simulation 1", while the bottom right panel is for the $Lambertian$ case of "Simulation 2" (see text). The measured total charge is $Q_{\rm exp}$=881 pC, while the simulated ones are $Q_{\rm sim}$=941 and 860 pC for Simulations 1 and 2, respectively (see Table 2).

Chapter 5

Gamma-ray tracking with an Artificial Neural Network

5.1 Introduction

5.1.1 Artificial Neural Network

Artificial Neural Networks (ANNs) are being developed since 1940s, with *McCulloch and Pitts* (1943) being the first work to introduce an idea of an artificial neuron, today known as a McCulloch-Pitts unit. The basic idea was to represent the structure of biological neurons and the interconnected structure of neurons featured in brains. The first artificial neuron was a simple binary unit, capable of logical operations e.g. $a\ and\ b$ or $a\ or\ b$, by producing a binary (0 or 1) output. It also had a simple threshold step function θ, allowing for an artificial neuron to "fire" (activate) when the integrated input value was above the threshold. The work on the ANNs continued over the years, with the introduction of perceptron (*Rosenblatt*, 1958) being an important advancement in the field. Perceptron was based on McCulloch-Pitts units and represented a first model of supervised learning. In modern terms a perceptron is considered a single-layered neural network.

In 1986, the "backwards propagation of errors" or the $backpropagation$ method was introduced as a new way of learning of the ANNs (*Rumelhart et al.*, 1986). The backpropagation method proved to be much faster than previous learning methods, allowing the ANN to be used in solving a wider range of problems. Up until today, the backpropagation, used with an optimization method such as gradient descent (see Sect. 1.2), remains one of the main methods of supervised learning of the ANNs. By supervised it is implied that the network is provided with an example of known inputs and the linked desired outputs.

Presently, thanks to the increased structural and functional complexities, the ANNs are used in a number of fields, including machine learning, robotics, medicine, neurobiology, cognitive science and others. In detail, ANNs are applied in signal processing, pattern recognitions, speech or vision recognition, navigation, modeling of human brain, various data processing (finance, analysis), games and decision making etc.

The ability to solve complex, non-linear problems and find non-linear functional dependencies and the adaptiveness to solving tasks using unknown sets of data were the reasons we decided to utilize the ANN algorithm as a method for 3D imaging with our detector modules. Ultimately, it is a tool which should allow us to reconstruct the first interaction positions of

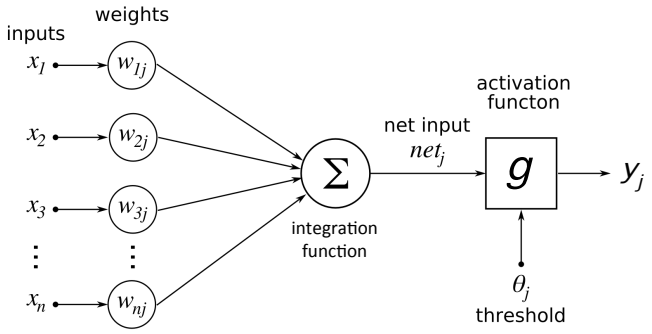

Figure 5.1: A representation of an artificial neuron - a main computational unit of the ANN. The $x_{1\dots n}$ are the input values with corresponding attributed weights $w_{1j\dots nj}$, Σ is an integration function reducing the number of inputs to a single net input value, g is the activation function of the neuron, with θ_j being the threshold value attributed to g and y_j are the corresponding output features.

detected unknown gamma-rays from the corresponding recorded read-out of our acquisition system.

A schematic representation of an artificial neuron (node, unit), modeled on a structure of a biological neuron, is represented on Figure[1] 5.1.

The neuron (Fig. 5.1) receives real input values x_i from multiple ($i = 1 \dots n$) input channels which represent biological dendrites. The inputs are integrated inside the neuron and are processed by an arbitrary selected function g named neuron activation function. The integration is usually very simple, e.g. involving only addition. Additionally, there is a possibility to assign weights w_{ij} to each input value x_i through multiplication: $x_i w_{ij}$ (*Chapter 1, Rojas, 1996)*. The output y_j, representing the axon of a biological neuron, is given as a combination of all weighted inputs:

$$y_j = g\left(\sum_{i=1}^{n} x_i w_{ji}\right) \tag{5.1}$$

Neurons are used as a main building block in forming the interconnected, network structure. Several neurons connected to each other can form a so-called layer, comprising a simple neural network. Today the complexity of the ANN is arbitrary and can involve inclusion of several layers each containing a large number of nodes.

5.1.2 JETNET 3.0

Our main choice for the ANN algorithm is the software toolkit JETNET 3.0 (*Peterson et al.*, 1994), which is implemented through FORTRAN 77 programming language. JETNET 3.0 is a powerful package based on a feed-forward multilayer perceptron neural network.

The feed forward ANN is the simplest type of the neural network, in which the data flow is linear - the connections between the units do not form any loops or cycles. In other words, the information moves in a single direction through the network, from input to the output.

A multilayer perceptron (MLP) refers to an ANN structure consisting of multiple layers each including a number of nodes (e.g. as on Figure 5.2), while perceptron is a single-layered

[1]Image: Chrislb, CC BY-SA 3.0, `https://commons.wikimedia.org/w/index.php?curid=224555`.

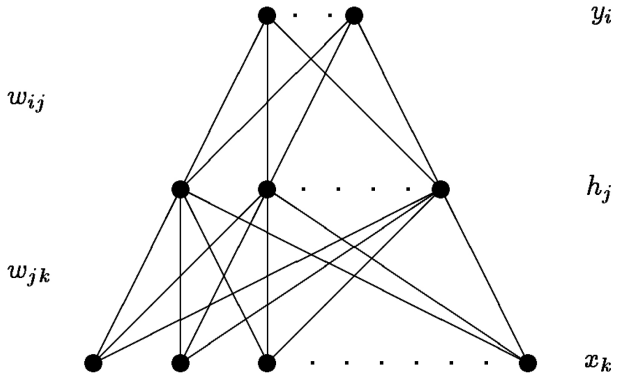

Figure 5.2: A schematic representation of a multilayer perceptron structure available with JETNET 3.0. We can see an ANN with one input layer made out of x_k nodes, one hidden layer containing h_j nodes and one output layer with y_i nodes. The nodes are connected through weights w_{jk} and w_{ij}, where i,j and k denote the index of nodes in each layer, respectively.

model of an ANN introduced by *Rosenblatt* (1958). On the other hand, the multilayer perceptron is an ANN with a more complex structure. The benefits of the MLP are the ability to approximate any continuous functional mapping as opposed to single perceptrons which have limitations on the range of functions they can represent (*Chapter 4, Bishop, 1995)*.

An example of an ANN structure is represented on Figure 5.2. Three layers of an MLP ANN are shown, where each layer contains multiple neurons and forms an interconnected structure of nodes. The first layer from the bottom, x_k, represents the input layer. These are the values which we provide to the network, and may represent some observed variables. To be able to select some desired features of interest y_i, from the known variables, selections need to be implemented. A group of such selections is represented by a set of feature functions F_i, with the ANN being an automated process for finding the optimal values of these functions.

$$y_i = F_i(x_1, x_2, ...) = F_i(\vec{x}) \ . \tag{5.2}$$

In fact, the function F_i, also called the network function, represents the network structure of the complete ANN (see *Bishop*, 1995, *Chapter 4)*. It is usually given as a composition of other functions (g) and can be expressed by e.g. a nonlinear weighted sum. For the JETNET 3.0 example, shown on Fig. 5.2, the network function is:

$$F_i(\vec{x}) = g[\frac{1}{T}\sum_j \omega_{ij} g(\frac{1}{T}\sum_k \omega_{jk} x_k + \theta_j) + \theta_i] \ . \tag{5.3}$$

Here, ω_{ij} and ω_{jk} are the weights, which in practice are parameters fitted to the data distributions, and the $g(x)$ is the non-linear activation function of a node, T is so called "temperature" and sets the gain of $g(x)$ (*Lönnblad et al.*, 1992), θ_j and θ_i are the activation function threshold values for layers h_j and y_i.

Further in JETNET, the non-linear node activation function is typically given by:

$$g(x) = \frac{1}{2}[1 + \tanh(x)] = (1 + e^{-2x})^{-1} \ . \tag{5.4}$$

The middle layer, noted with h_j in Figure 5.2, is the hidden layer. It enables the non-linear modeling of the input data. In practice, it is possible to choose the number of hidden layers

and their structure thus adjusting the complexity of the network structure. The top layer, noted y_i on Figure 5.2, is the output layer, which returns the requested features y_i.

The optimal values of weights (parameters), ω_{ij} and ω_{jk}, are found by minimizing the error (loss) function E, which is a mean square error between the output features y_i and the targeted values for these features t_i with respect to the weights.

$$E = \frac{1}{2N_p} \sum_{p=1}^{N_p} \sum_{i} (y_i^{(p)} - t_i^{(p)})^2 \tag{5.5}$$

The targeted values t_i are the values we selected and provided to the network. A loss function E is the measure of how good "predictor" is the network. For linear problems it is possible to find an exact solution, but for a non-linear problems, as in our case, the solution is found by an iterative process (minimization). Once the fitting of the weights is completed a network is ready to be used in modeling the unknown data, i.e. to perform the "generalization".

The backpropagation for MLPs solves the problem of not knowing the targeted (desired) outputs of the hidden layers. Backpropagation is done in several steps. Looking at Fig. 5.2, the first step is a straight forward calculation of all of the network values and finding the desired output values y_i. Next, by comparing the outputs y_i with target values t_i, we can calculate the errors of these outputs, e.g. the function E (equation 5.5). Next step is returning (thus backpropagation) the calculated errors of the output layer to the hidden h_j and then to the input layer x_k. This enables the calculation of according errors of outputs from these two layers. This information is then used to adjust the weights i.e. w_{jk},w_{ij}, and the process is repeated until the error function (E) is minimized.

In JETNET 3.0 the minimization of equation 5.5 is done using the "gradient descent" method together with so-called Langevin updating. Gradient descent is a way to find the local minimum of a function by moving in steps, where each step is proportional to the negative (thus descent) gradient of the function:

$$\omega_{t+1} = \omega_t + \Delta\omega_t \ , \tag{5.6}$$

where

$$\Delta\omega_t = -\eta \frac{\partial E_t}{\partial \omega} = -\eta \nabla E_t \ . \tag{5.7}$$

Here, ω represents the whole vector of weights used in the network, $\Delta\omega$ is the weight update, η is the learning rate – a parameter which shows by how much we change the weights ω at each step – and ∇E is the gradient of the error function E with respect to ω_t.

Furthermore, to stabilize the learning and solve the "flat-spot" problem, when the nodes become oversaturated, and the derivative which is propagated backwards becomes zero (*please check: Johansson et al., 1991; Fahlman, 1989)*, we used Langevin updating method (*Rögnvaldsson*, 1994) – an option available within JETNET 3.0. Langevin updating is done by introducing an extra term to the minimization process:

$$\Delta\omega = -\eta \nabla E + \sigma \ , \tag{5.8}$$

where σ is the key factor in this method and represents a Gaussian noise term. The main contribution of Langevin updating is the improvement of the minimization process performance, which is done by introducing the noise directly to the weights during the weight optimization process of the ANN.

5.2 ANN configuration and training

Regarding our work, the benefits of the ANN include its rather simple utilization after completing the training process and the ability to do a reconstruction of the position of the first interaction of gamma-rays in scintillation crystals in 3D, thus, also providing us with the information on the depth of interaction (DOI), noted as the coordinate Z. To be able to use the ANN, we had to perform several preparation steps, including the choice and configuration of the ANN parameters, and the completion of the ANN training process. We performed systematic testing of the parameters, finally adopting a configuration which enabled proper representation of the non-linear transfer function of the detector, all the while limiting the complexity of the ANN structure and thus the computation time.

First, we had to decide on the general ANN structure. We started by defining the general format of the ANN, similarly to the one shown in Figure 5.2.

We begun with considering the format of the input layer i.e. which information to provide to the ANN. We started to study reconstruction of the 2D position of the gamma-ray first interaction in the detector frontal plane. For this, to compare the ANN performance with that of a simple Anger logic algorithm (explained in Chapter 6), we first fed the network with the center of gravity of truncated charge distributions using only the N pixels with the highest charge value, with $N = 4, 9, 16, 25$ or 36. However, we concluded that in such way we would lose valuable information contained in the output of the 64 MAPMT channels (e.g. the charge distribution), so using the center-of-gravity values to train the ANN should not provide the most optimal results. Thus, we tested another option, that is to use directly the 64 values from the MAPMT output as the ANN input values. This resulted in better ANN performance, e.g. the ANN trained with center-of-gravity inputs provided a root-mean-square error of the reconstructed 2D position of $\sigma \approx 3$ mm, while when we used the 64 charge values as ANN input we obtained $\sigma \approx 2.5$ mm. Therefore, we selected the 64 charge values as our preferred ANN input format.

Next, we proceeded with testing the other parameters of the ANN, starting with the number of hidden layers and the number of nodes in each layer. We tried the options of having one, two or three hidden layers, increasing the networks complexity. However, the optimal results were obtained by using the configuration with two layers, as using only one layer was insufficient leading to bad ANN performance. The other test, using three hidden layers, required considerably longer computational time, without granting a significant performance improvement. The option of using two layers was also in accordance with (*Peterson et al.*, 1994; *Lippmann*, 1987).

Similarly, we tested the number of nodes within the hidden layers, from several to several tens, eventually settling on 10 nodes per each hidden layer. In a similar way having just 3 – 5 nodes was not sufficient enough to give optimal performance, while using 20, 30 or 40 nodes increased the ANNs training time considerably, without having any significant impact on the final results. Furthermore, using a more complex network with a large number of nodes, might lead to a negative effect of "overfiting" the network (*Peterson et al.*, 1994). Therefore, we opted for the choice of 10 nodes per layer.

Final optimization testing was performed on the number of "epochs" i.e. the number of iterations of the ANN learning process, where we decided on setting this value to a maximum of 1000 (e.g. see Figure 5.3). Even more, we run additional tests going up to 10^4 iterations, which provided us with no improvement of the gamma-ray hit position reconstruction obtained after the training process.

To be able to perform the training of the ANN, we needed to provide a large amount of data to the ANN in order to generate the proper weights. For this purpose, we used the Geant4 simulation configurations we found are the best in representing the experimental results. As discussed in Chapter 4, we studied two Geant4 simulation configurations: "Simulation 1" uses the $specularspike$ type of reflection for treating the reflection of optical photons from the sides of the scintillator and the optical window, while for "Simulation 2" we adopted the $Lambertian$ type of reflection for the same surface. Also, we used different gamma-ray energies, $E_\gamma = 59.5,\ 356$ and 661.7 keV, corresponding to gamma-ray lines from ^{241}Am,^{133}Ba and ^{137}Cs radioactive sources, respectively. The beam position was defined as perpendicular to the detector entrance surface and its X–Y position was randomized for each event in order to uniformly irradiate the full detector area. During the simulation we selected the events that fully deposited their initial γ-ray energy within the crystal. Additionally, for all of these "good" events, we recorded the first 3D interaction position and energy deposited in each hit. For each run (defined by the simulated module, the simulation configuration, and the γ-ray energy), we generated typically $(5\text{–}10) \times 10^4$ simulated good events.

After the training process is completed, the ANN returns a file containing the generated weight values, which in our case is a single file with corresponding values for the weights between each of the layers and the threshold values for the two hidden layers and the output layer. This enabled us to finally be able to introduce unknown data to the ANN and use it to obtain the results of the 3D position reconstruction method.

5.3 ANN performance using simulated data

5.3.1 X–Y position reconstruction

Figure 5.3 shows an example of the 1σ error of the three position coordinates of the first gamma-ray hit (noted with X_1, Y_1, Z_1 in the figure), returned by the ANN, as a function of the number of iterations in the training process. Each value on the figure is a root-mean-square (RMS) error of the reconstructed position, calculated using the 3D position of the first interaction of all of the simulated events. We see that the 1σ values meet asymptotic values ($\sigma_X \approx \sigma_Y \approx 2.5$ mm and $\sigma_Z \approx 2.2$ mm) after about 500 iterations.

In Figure 5.4, we show the standard deviations σ_X and σ_Y ($\equiv \sigma(X_1)$ and $\sigma(Y_1)$) returned by the ANN from the validation process, as a function of the number of simulated events used in the training process. For a number of training events between $\sim 3.5{\times}10^4$ and $6.5{\times}10^4$, we have $\sigma_X \approx \sigma_Y \approx 2.5$ mm. In the following, the studied networks are trained with typically $6{\times}10^4$ events during 1000 iterations.

Furthermore, in Figure 5.5, we show the two-dimensional distribution of the RMS error of the reconstructed position, again returned by the ANN after the training process. The $10{\times}10$ values represented in Figure 5.5 are average values of the two standard deviations σ_X and σ_Y. We can see that these values are worse in the corner positions or near the sides ($\sigma > 2.5$ mm), when one or both coordinates have maximal values: $X_{\rm POS}$ and/or $Y_{\rm POS} \geq 2$ cm. On the other hand, in the middle positions the 2D sigma values can go as low as $\sigma = 2$ mm.

5.3.2 Depth of interaction reconstruction

Another result, obtained using the ANN, was the testing of reconstruction of the depth-of-interaction (DOI, Z coordinate) of the first interaction position of gamma rays inside the module. It is important to state that we had no experimental ways to measure the DOI using our

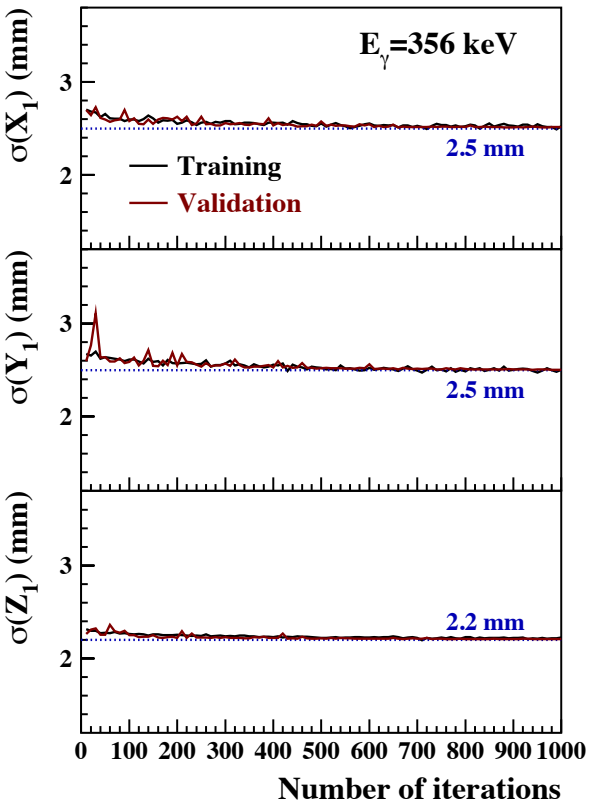

Figure 5.3: RMS deviations of the reconstructed 3D position of gamma-ray hits from the training and validation processes of the ANN as a function of the number of iterations in the training process. The three panels correspond to three position coordinates of the first γ-ray hit in the $LaBr_3$:Ce crystal. The ANN training and validation processes are done with 6×10^4 and 3×10^4 simulated events, respectively. The Geant4 simulation is performed for incident γ-rays of energy $E_\gamma = 356$ keV using the configuration of "Simulation 2" (see text).

test bench. In Figure 5.6 we present the results, obtained with two different fully trained ANNs. Both ANNs were trained with the same Geant4 configuration (Simulation 2), but we trained the first one using events simulated with $E_\gamma = 59.5$ keV (^{241}Am source) and the second one using events simulated with $E_\gamma = 356$ keV (^{133}Ba source) radioactive beam. Furthermore, to test the ANNs performance we used $80{\times}10^3$ simulated events with $E_\gamma = 59.5$ keV and $30{\times}10^3$ simulated events with $E_\gamma = 356$ keV.

Figure 5.6 shows the two studied cases of the DOI for the two energies of gamma rays (59.5 and 356 keV) used to train the ANN:

- $Left\ panel$; We show the first 1 mm of the $LaBr_3$:Ce scintillator crystal and clearly see that the majority of the interactions from the simulated (Geant4) $E_\gamma = 59.5$ keV gamma-rays (black line) occur within the first 0.5 mm of the crystal, while the recorded distribution corresponds to an exponential decline. Such trend is as expected for the low energy gamma-rays, as their energy is insufficient for them to penetrate deeper within the detec-

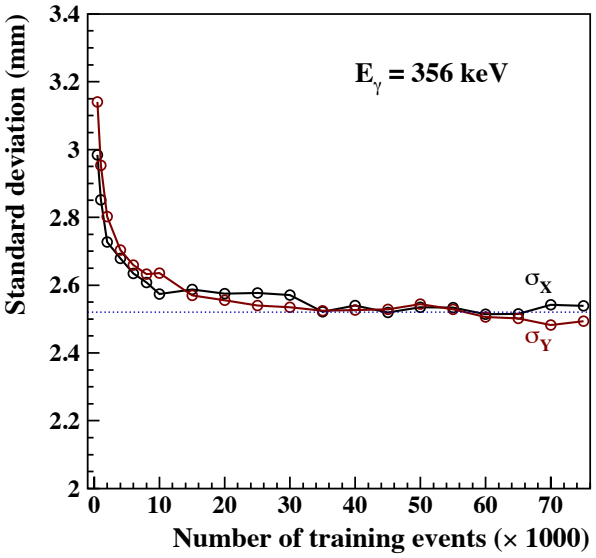

Figure 5.4: Standard deviations of X_1 and Y_1 from the ANN validation process, as a function of the number of training events. The ANN training configuration is as for Fig. 5.3. The number of iterations in the ANN training process is 1000.

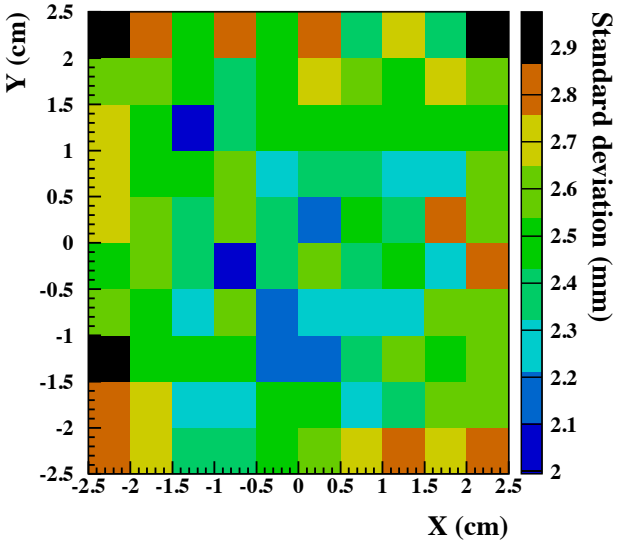

Figure 5.5: Distribution of the RMS error of the reconstructed X–Y position, averaged for both coordinates X and Y, as a function of position on the front plane of the crystal. The values are obtained from the ANN readout after the training and validation processes. The ANN training configuration is the same as for Figures 5.3 and 5.4.

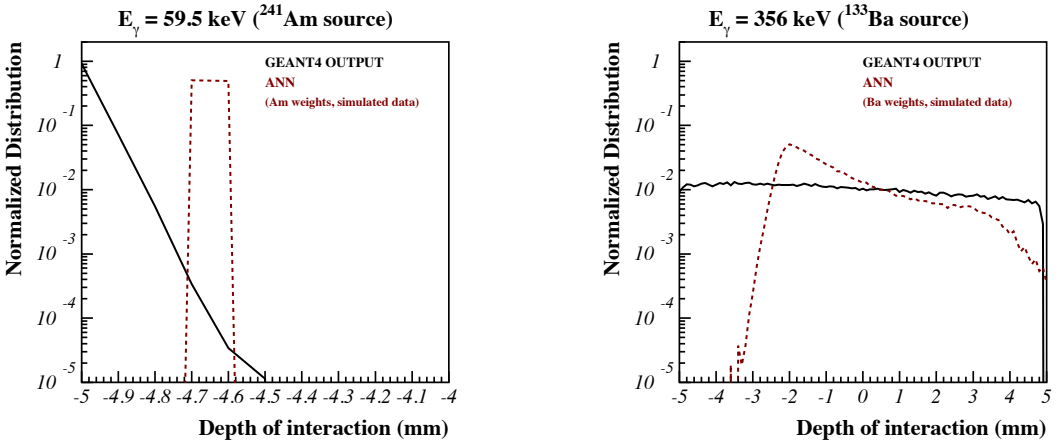

Figure 5.6: Study of the ANN performance on the reconstruction of the depth-of-interaction (DOI) of the first interaction position of the incident gamma rays within the $LaBr_3$:Ce detector. Full black lines are direct DOI output from the Geant4 simulations, while in red we give reconstructed DOI values from the ANN. $Left$: ANN trained with E_γ = 59.5 keV gamma rays; $Right$: same study for the case of E_γ = 356.5 keV.

tor. The small inconsistency in the distribution, seen at ∼4.6 mm, is caused by the low statistics. However, we also see that the results obtained from the ANN are shifted deeper inside the crystal, by several tenths of a millimeter. The shift comes from the imperfect ANN performance, with the ANN having problems reconstructing positions near the edges of the crystal, because the scintillation light distribution is essentially independent of the DOI for $Z_1 < 1$ mm.

- *Right panel*; Here we present a case where the ANN, trained with E$_\gamma$ = 356 keV gamma-rays, was used to reconstruct the DOI from the data simulated with the same energy. The noted shift of 1–2 mm and a peak in the reconstructed DOI (in red) is, again, most likely due to poorer ANN performance near the crystal edges. However, for both distributions (red and black) we find expected behavior for gamma rays of higher energy (E_γ = 356 keV): the interaction depth is distributed evenly through the crystal volume as the gamma rays are energetic enough to pass through the full thickness of the detector.

5.3.3 Module design optimization

With the ANN, we have also explored the possibility to use different Geant4 simulation configurations, which differ from the real experimental detector module geometry, in order to study the performance and the possibilities of different construction concepts. In this way, we were able to gain insight on how optimal is the physical design of our detector modules and if changing some of the elements would improve the performance.

An example of one of such tests was to use the same Geant4 simulation as for the training process explained above ("Simulation 2" configuration and geometry from Chapter 4) but changing the thickness of the optical window from $d = 5$ mm to $d = 0.5$ mm. We defined a gamma-ray beam as perpendicular to the central position $X_{\mathrm{POS}} = Y_{\mathrm{POS}} = 0$ mm, of the $LaBr_3$:Ce crystal, and with energy $E_\gamma = 356$ keV (^{133}Ba source). In such manner we generated $\approx 50 \times 10^3$ events. We used this data to train the ANN and through training acquired the values

for the RMS errors of the three coordinates: $\sigma_X = 2.3$ mm, $\sigma_Y = 2.3$ mm and $\sigma_Z = 1.9$ mm. These values are comparable with the values shown in Figure 5.3 and show a similar dependency from the number of iterations used in the training process. The fact that there is no big improvement on the RMS errors of the reconstructed positions shows that the thickness of the optical window is in fact not the main parameter limiting the position resolution.

The main limitation of the imaging performance of the $LaBr_3$:Ce detector module is most likely due to the propagation of the scintillation light within the scintillator crystal, previous to their collection on the photocathode of the MAPMT. The optical photons produced during gamma-ray interactions can either have relatively direct paths from the interaction positions to the photocathode of the MAPMT or they can first undergo numerous reflections from the surfaces within the detector. If the number of optical photons with complex trajectories is not negligible, this influences the final distribution of the readout charge from the 64 channels of the MAPMT, producing an almost uniform background, thus influencing the position reconstruction precision. As recently proposed by *Iltis and Snoussi* (2015), a possible way to improve the position resolution in a monolithic $LaBr_3$:Ce crystal would be to perform timing measurements of the arrival of scintillation photons at the photocathode with an accuracy of about one hundred picosecond, in order to be able to distinguish unscattered photons from those detected after several reflections.

We also note that the detector readout is done with 64 MAPMT channels covering the detector area of 50×50 mm^2, thus each channel covers an area of 6.25×6.25 mm^2. As the obtained RMS errors on the 2D position reconstruction, σ_X and σ_Y, are generally in the range 2 – 2.5 mm, it means that the position resolution obtained through the ANN is of the order of $1/3$ of the readout channel (pixel) size. Such pixel size limitation may have a larger influence on the final results than the thickness of the optical window within the detector module. One possible way of improving the position resolution in the future would be to use a higher pixelization readout system, e.g. the Hamamatsu H9500 16×16 channels MAPMT, at the cost of increasing the number of readout electronics channels.

Chapter 6

Experimental results

6.1 Position reconstruction

An important goal of the thesis work is to study the accuracy of localization of γ-ray hits inside the scintillator crystal using the distribution of charges onto the 64 anodes of the PMT (see, e.g., Figs. 4.6 and 4.7 in Chapter 4). Studying the shape of these distributions via different algorithms can give us information on the position of interaction on the front plane of the detector (2D position reconstruction in the X–Y plane), as well as on the depth of interaction Z inside the crystal (*Tatischeff et al.*, 2010).

We first developed a simple center-of-gravity method (Anger logic) to test the 2D position reconstruction. We then used an Artificial Neural Network (ANN) to estimate the 3D position of the gamma-ray hits, as explained in Chapter 5. The results of the two methods are compared thereafter.

6.1.1 Anger logic algorithm

The Anger logic algorithm is based on a center-of-gravity calculation that gives the location of the highest charge accumulation within the distribution of outputs from the 64 MAPMT channels (see, e.g., Fig. 4.6). We test the position reconstruction using experimental data from the collimated ^{241}Am source, which we obtain as explained in Chapter 3, Section 3.6, and study only the 2D position reconstruction (in the X–Y frontal plane of the detector).

We start by calculating the center of gravity of truncated charge distributions using only the N pixels with the highest charge value, with $N = 4$, 9, 16, 25 or 36. The mean reconstructed positions obtained for each measurement are shown by the open symbols in Fig. 6.1 for both the $LaBr_3$:Ce and $CeBr_3$ detectors. We show in this Figure only one coordinate of the reconstructed position on the detector front plane ($X_{\rm POS}$), the results obtained for the other coordinate ($Y_{\rm POS}$) being almost identical. For a given value of N and by using a simple linear interpolation, we then obtain a relation which gives the "real" (i.e. known) position as a function of the reconstructed position.

In the second step, we calculate for each event the center of gravity of the charge distribution – this gives a first reconstructed position – and then estimate the real position by using the relation obtained at the first step. An example of a corresponding distribution of events is shown by the green histogram in Fig. 6.2. We see that the peak of this distribution ($X_{\rm POS} = +5.60$ mm) is in better agreement with the experimental position ($X_{\rm POS} = +5$ mm)

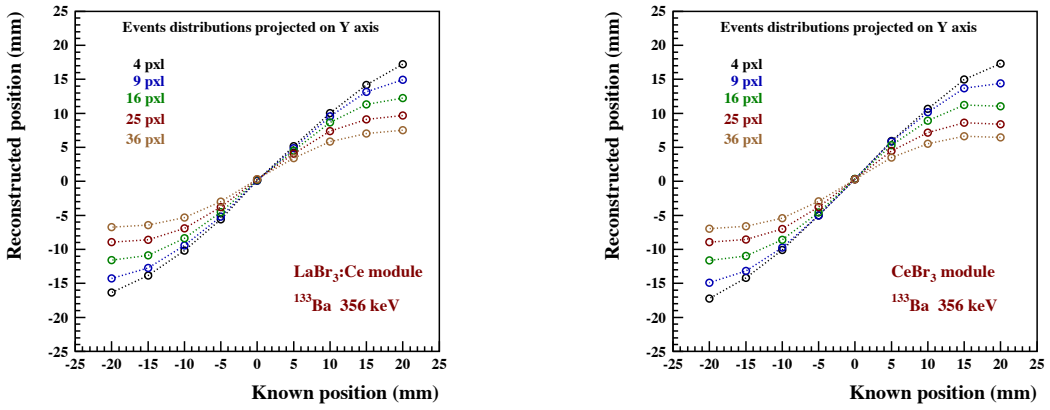

Figure 6.1: First reconstructed position obtained by a center-of-gravity method as a function of the experimental irradiation position (open symbols). Different experimental points are obtained for different number of pixels utilized for the truncated charge distributions. *Left:* $LaBr_3$:Ce; *Right:* $CeBr_3$ module.

than the mean value of the first-step distribution ($X_{\rm POS} = +3.76$ mm). But the associated error in the reconstructed position is larger after the second step (FWHM $= 7.55$ mm versus 5.29 mm), due to the compaction (flattening) of the reconstructed positions when moving away from the detector center (see the S-shape of the curves shown in Fig. 6.2).

The position resolution obtained with this method is shown in Figure 6.3. The resolution results from both the width of reconstructed position histograms and the offset of the distributions compared to the "real" positions of irradiation (see Fig.6.2). While the dispersion of the data is more important to the final resolution for irradiation in the central region of the detector, typically for $X_{\rm POS} \leq 10$ mm, the offset becomes dominant near the edges, and it increases with the utilized number of pixels. A good compromise between the resolution obtained close to the borders and the one in the middle of the crystal is achieved using $N = 9$ pixels.

We also see in Figure 6.3 that the reconstructed position resolution for the $CeBr_3$ module is not as good as for the $LaBr_3$:Ce detector. This is partly because $CeBr_3$ is producing less scintillation light (45 ph keV^{-1} versus 63 ph keV^{-1} for $LaBr_3$:Ce; compare also the charges in Tables 4.1 and 4.2), but it is most likely due also to intrinsic properties of the modules: possible inhomogeneities within the crystal, finish on the crystal surfaces, reflector coating etc..

6.1.2 ANN performance with experimental data

In Figures 6.4 to 6.6, we show some examples of reconstructed X-Y positions applying the ANN method to data acquired by the scanning measurements (Sect. 3.6).

We use diagonal series of measurements with all sources, and additionally a horizontal scan and a vertical scan of the $LaBr_3$:Ce detector with the ^{133}Ba source. The results shown in Figure 6.4 for three γ-ray energies (59.5 keV, $\sim$360 keV, and 662 keV) were obtained with a single ANN, independent of energy, which was trained with Geant4-simulated data for incident γ-rays of energy $E_\gamma = 356$ keV using the configuration of "Simulation 2" (see Chapter 4). We see that the data are generally well clustered around the gamma-ray beam positions, which illustrates the goodness of this position reconstruction method (the obtained position resolution

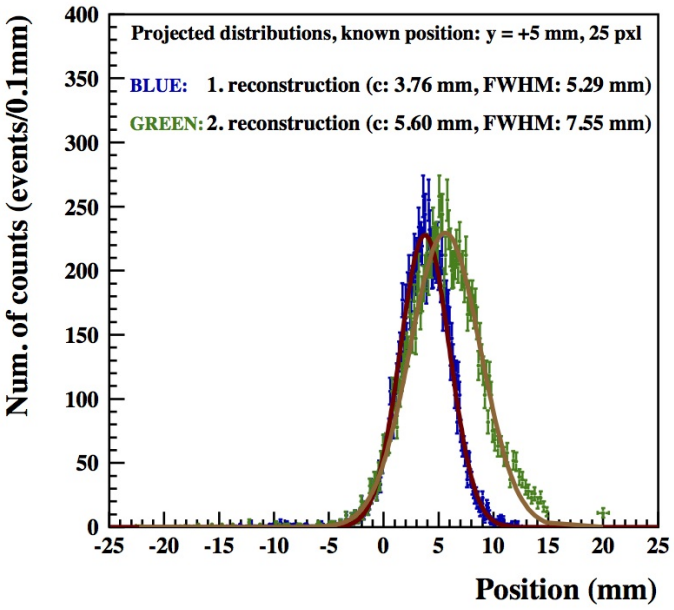

Figure 6.2: Distributions of reconstructed positions for each full-energy event of the measurement with the collimated ^{241}Am source at $X_{\mathrm{POS}} = Y_{\mathrm{POS}} = +5$ mm from the $LaBr_3$:Ce detector middle position, using the 25 pixels with the highest charge value. Blue histogram: first reconstruction step of the center-of-gravity method; green histogram: second reconstruction step after interpolation between the mean values obtained in the first step. The solid curves show Gaussian fits to the data yielding centroid values of +3.76 and +5.60 mm, and FWHM of 5.29 and 7.55 mm, for the blue and green histograms, respectively.

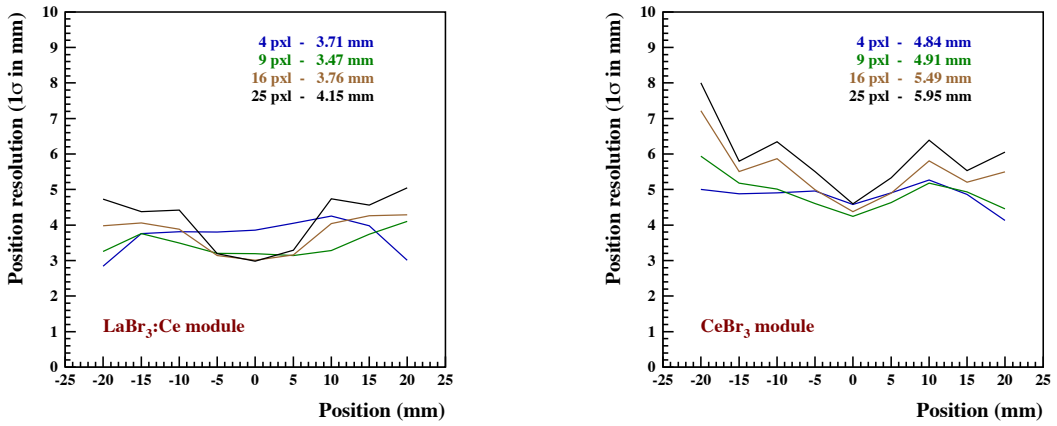

Figure 6.3: Position resolution obtained by the center-of-gravity method – 1σ standard deviation about the experimental position – as a function of projected distance from the center along a diagonal in the front plane of the detector. Each line corresponds to a given number of pixels, as indicated in the panels. The values given in the panels correspond to the mean position resolutions. *Left:* $LaBr_3$:Ce; *Right:* $CeBr_3$ module.

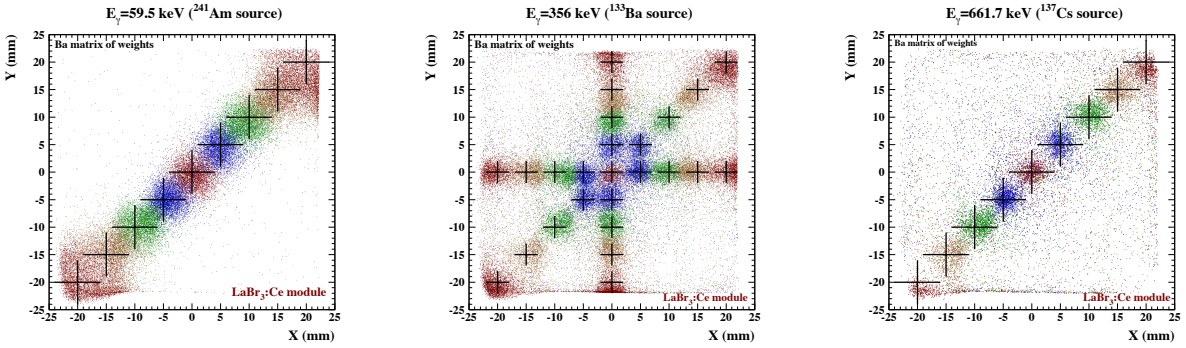

Figure 6.4: Reconstructed X-Y position of the first γ-ray hit in the $LaBr_3$:Ce crystal using the ANN method. From left to right, the data are for fully-absorbed 59.5-keV γ-rays (^{241}Am source), $\sim$ 360-keV γ-rays (from the lines at 356 and 384 keV from the ^{133}Ba source), and 662-keV γ-rays (^{137}Cs source). The black crosses note the γ-ray beam positions during the measurements; they change in steps of ± 5 mm for $X_{\rm POS}$ and $Y_{\rm POS}$ starting from the central position ($X_{\rm POS} = Y_{\rm POS} = 0$ mm). The ANN was trained using 6×10^4 simulated events for incident γ-rays of energy $E_\gamma = 356$ keV, using the configuration of "Simulation 2" (see Chapter 4).

is further discussed in the next section). The clustered data are superimposed on a uniform background covering most of the detector surface, which is mostly due to the internal, self-counting background of $LaBr_3$:Ce. The relative intensity of this background with respect to the emission from the collimated sources depends on the γ-ray energy and source intensity. It is of the order of 1% for the ^{241}Am source (left panel), 10% for the ^{133}Ba source (middle panel), and 25% for the ^{137}Cs source (right panel).

It is remarkable that the γ-ray interaction location in the $LaBr_3$:Ce detector can be fairly well estimated for all γ-ray energies using a single file of weight values from the ANN training process. However, the position reconstruction could in principle be further improved using different weight matrix files for different energies. This is illustrated by the left panel of Figure 6.5, which shows the reconstructed position of ^{241}Am data with an ANN trained at 59.5 keV. By comparing this plot with the left panel of Figure 6.4, we see that, while the improvement for the center of the detector is not obvious, that for the two extreme positions is clear, the data in red being more concentrated around the beam position.

In the middle panel of Figure 6.5, we show the performance of an ANN trained with data simulated using the configuration of "Simulation 1" (i.e. with the $specularspike$ option for the type of reflection from the border sides of the crystal and optical window, see Chapter 4). We see that the results are not as good as those obtained using "Simulation 2" (middle panel of Fig. 6.4), especially near the detector corners. We note also that the background is not anymore uniformly distributed over the detector surface, which further illustrates the bad reconstruction of γ-ray events in the outer area of the detector. This is consistent with the results of Chapter 4 (Section 4.2.3), where we found that "Simulation 1" significantly overestimates the measured contrast for the beam position $X_{\rm POS} = Y_{\rm POS} = 20$ mm (see Figure 4.5 and Table 4.1).

We also studied the possibility of using two different sets of simulated data to train the network, one for γ-ray impacts around the center of the detector and another for the outer area. This was motivated by the results of the Geant4 parametric study (Chapter 4), where we found it difficult to reproduce accurately all the experimental data with a single value of the σ_α parameters. In practice, we used the configuration of "Simulation 2" except for $\mathrm{SigmaAlpha}\ 2$: we created a first set of simulated data covering the square area from the center of the detector

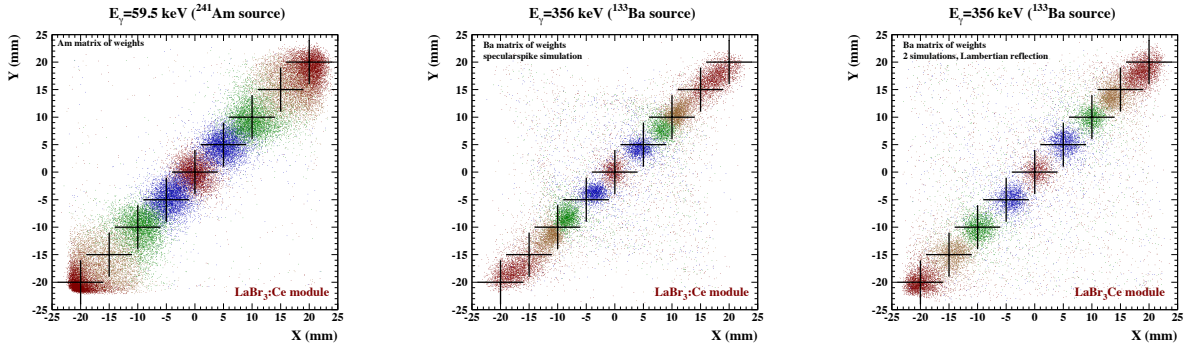

Figure 6.5: Further examples of ANN performance for the reconstructed X-Y position of the first γ-ray hit in the $LaBr_3$:Ce crystal. Left panel: ^{241}Am data reconstructed using an ANN trained with simulated events from 59.5 keV γ rays and with the configuration of "Simulation 2" (see Sect. 3.4). Middle panel: ^{133}Ba data reconstructed with an ANN trained with simulated events from 356 keV γ rays and with the configuration of "Simulation 1". Right panel: ^{133}Ba data reconstructed with an ANN trained with two sets of simulated events, both produced with $E_\gamma = 356$ keV and "Simulation 2", but with two different values of SigmaAlpha 2 depending on the X-Y position (see text).

up to $X_{\rm POS} = Y_{\rm POS} = \pm 14$ mm with $\rm SigmaAlpha\ 2 = 0.5$ rad, and another set of data covering the remaining outer area of the detector with $\rm SigmaAlpha\ 2 = 10$ rad (see the right panel of Figure 4.5). The right panel of Figure 6.5 shows the performance of an ANN trained by these two sets of simulated data. As the position resolution obtained with this ANN was found to be not significantly better than that obtained using "Simulation 2" whatever the impact position of the γ-rays (middle panel of Figure 6.4), we have adopted the latter configuration as our default choice.

Figure 6.6 shows the performance of such an ANN for the position reconstruction within the $CeBr_3$ detector. We see that the results are not as good as those obtained with the $LaBr_3$:Ce detector for the same simulation configuration (middle panel of Figure 6.4). In particular, we observe in Figure 6.6 that the reconstructed data are significantly offset from the experimental beam positions, and that this offset is more important for positive $X_{\rm POS}$ and $Y_{\rm POS}$. Such an asymethry is due to intrinsic properties of our $CeBr_3$ module that cannot be easily taken into account in the Geant4 simulation.

6.1.3 2D position resolution

To estimate the accuracy of the 2D position reconstruction, one needs to take into account the background from the internal radioactivity of $LaBr_3$:Ce. We assumed that for each position measurement performed with this detector, the resulting 2D distribution of reconstructed positions (Figure 6.7, left panel) can be modeled with two functions: a 2D Gaussian representing the emission from the collimated source and a uniform distribution covering the whole detector surface representing the background radiation.

We then developed a Monte-Carlo simulation to fit the measured X–Y position distribution with two free parameters: the width of the Gaussian function ($\sigma = \sigma_X = \sigma_Y$) and the relative intensity of the background emission. We took into account the finite size of the collimated gamma-ray beam at the crystal position by selecting randomly for each event the central position of the Gaussian within a disc of known diameter (depending on the collimation used for

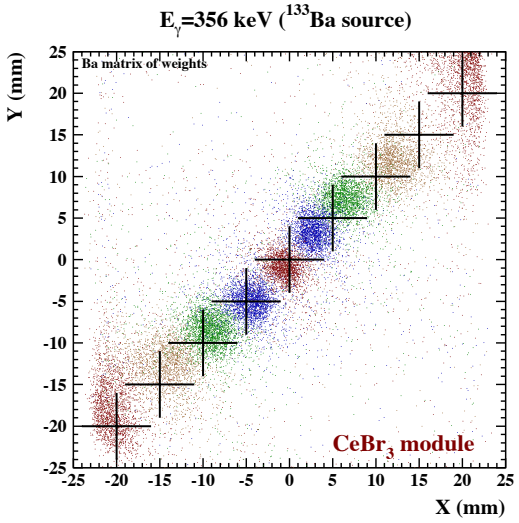

Figure 6.6: ANN performance for the reconstructed X-Y position of the first γ-ray hit in the $CeBr_3$ detector. The data are for fully-absorbed γ rays from the ^{133}Ba source. The ANN is trained with simulated events from 356 keV γ-rays, using the configuration of "Simulation 2" (see Chapter 4).

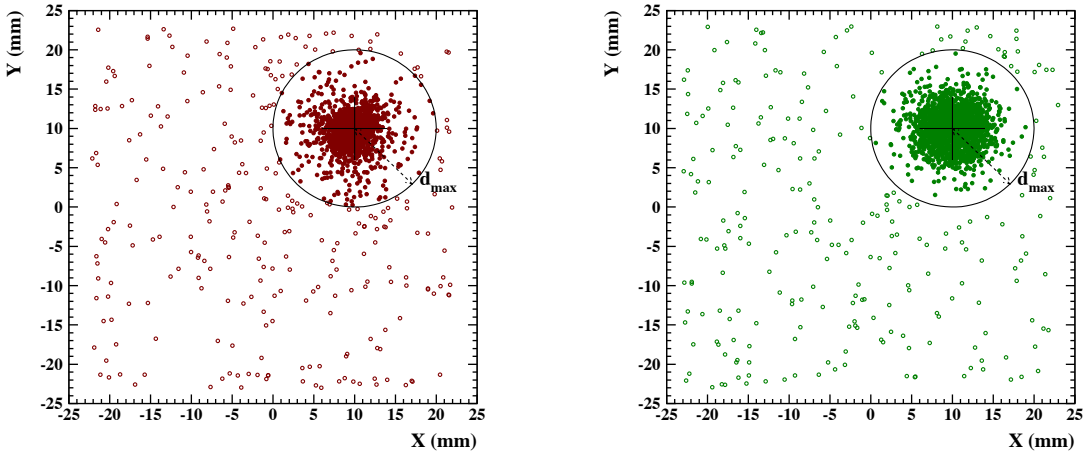

Figure 6.7: Measured (*left*) and simulated (*right*) distributions of reconstructed X-Y positions in the $LaBr_3$:Ce detector, for the ^{133}Ba γ-ray beam at the position $X_{\rm POS} = Y_{\rm POS} = +10$ mm. The position reconstruction uses the ANN trained with Geant4 simulated events from 356 keV γ-ray with the configuration of "Simulation 2". The two distributions were quantitatively compared (see text) by calculating the RMS error of the reconstructed beam position, using only the data within the circle of radius $d_{\rm max}$. For illustrative purpose, we used for this Figure the same number of Monte-Carlo simulated events as measured: 1800. The simulated data were drawn randomly using the best-fit parameters $\sigma = 2.2$ mm and $f_{\rm bg} = 14.5\%$, σ being the standard deviation of the Gaussian function representing the γ-ray emission from the collimated source and $f_{\rm bg}$ the relative intensity of the background emission.

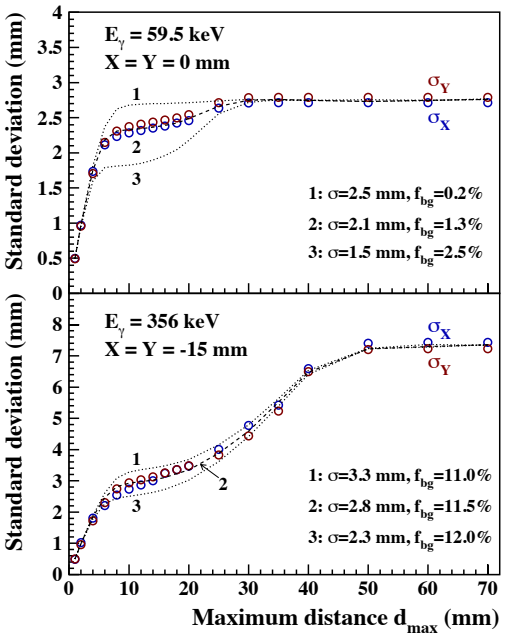

Figure 6.8: Standard deviations of truncated 2D distributions of the reconstructed γ-ray hit position around the experimental position of irradiation, as a function of the maximum distance of the reconstructed position to the γ-ray beam position. The number of events used in the calculations of the 1σ values thus increases with $d_{\max}$. The open symbols are standard deviations for $X_{\rm POS}$ (in blue) and $Y_{\rm POS}$ (in red) calculated with real data, whose positions were reconstructed with the ANN method (see text). The black curves are simulated fitting curves depending on two free parameters: the 1σ width of the Gaussian representing the γ-ray emission from the collimated source, and the relative intensity of the uniform background emission, $f_{\rm bg}$. We show two cases (top and bottom panels) for two different measurements as noted on panels. For each case we give three different fit functions, calculated with different parameters as noted on bottom right of the panels. Functions 1 and 3 are clearly over- and under-producing the data, respectively, while function 2 is the best-fit result.

the various sources, see Chapter 3, Section 3.6). An example of simulated distribution is shown on the right panel of Figure 6.7.

The modeled distributions were then fitted to the measured ones for each radioactive source and position of the collimator by calculating the standard deviations of truncated distributions as a function of the cut-off distance $d_{\max}$ defined in Figure 6.7. Two examples of such fits are shown in Figure 6.8, where both the ^{241}Am data (top panel) and ^{133}Ba data (bottom panel) were reconstructed using an ANN trained with simulated events from 356 keV γ-rays and with the Geant4 configuration of "Simulation 2". We see that the data can be well represented by the simulation.

Furthermore, the levels of background given by the fit (e.g. $f_{\rm bg} = 1.3\%$ and 11.5% for the two cases shown in Figure 6.8) were found to be in very good agreement with the ones estimated from the measured energy spectra. This indicates that our simple fitting procedure is adequate to estimate the uncertainty in the position reconstruction.

Figure 6.8 clearly shows the relevance of taking into account the background radiation

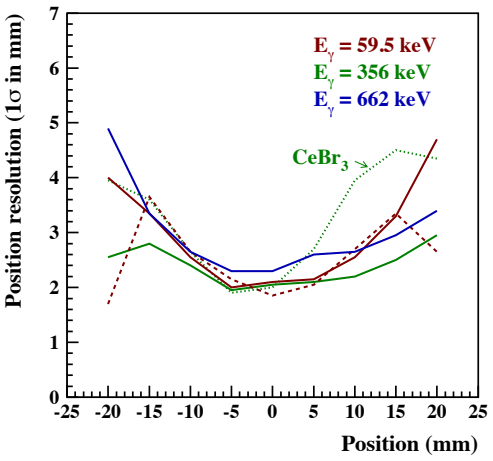

Figure 6.9: Position resolution obtained by the ANN method – 1σ standard deviation about the experimental position – as a function of projected distance from the center along a diagonal in the front plane of the detector. Solid lines: position resolution on data corresponding to measurements at three different energies (noted on the panel), where the γ-ray hit position is reconstructed with a matrix of weights from an ANN trained with simulated $E_\gamma = 356$ keV γ-rays and the Geant4 configuration of "Simulation 2". The red dashed line shows the error in the position reconstruction using simulated $E_\gamma = 59.5$ keV γ-rays (together with "Simulation 2"). The green dotted line gives the position resolution for the $CeBr_3$ detector; it is for ^{133}Ba data reconstructed with an ANN trained with simulated events from 356 keV γ rays and with the Geant4 configuration of "Simulation 2".

when estimating the position resolution. Thus, for the measurement with the ^{241}Am source at the central position (top panel), the standard deviation of the full position distribution using all events, i.e. without background subtraction, amounts to $\sigma_X \approx \sigma_Y \approx 2.8$ mm (the value of the plateau reached at $d_{\max} > 40$ mm in the top panel), whereas the best-fit value of the Gaussian width is $\sigma = 2.1$ mm.

Figure 6.9 shows the position resolution obtained with the ANN method, where the standard deviations as a function of position were calculated as explained above. We see that the resolution is better in the middle of the $LaBr_3$:Ce crystal than near the edges. Thus, in the center of the detector up to $X_{\mathrm{POS}} = Y_{\mathrm{POS}} = \pm 10$ mm, the 1σ values are between ~ 2.0 and 2.6 mm for the three γ-ray energies. The resolution is not as good in the outer area of the detector, especially for the ^{241}Am and ^{137}Cs data when using an ANN trained at 356 keV. As shown by the dashed line in this Figure, using an ANN trained with simulated γ-rays of 59.5 keV can significantly improve the resolution for the ^{241}Am data at the studied extreme positions $X_{\mathrm{POS}} = Y_{\mathrm{POS}} = \pm 20$ mm. However, using different matrices of weights for different energies can be problematic when the method is applied to a Compton telescope, because neither the energy of the incoming γ-ray nor the mechanism of its interaction in the detector (Compton scattering, photoelectric effect leading to a full-energy deposit etc.) are known a priori.

The average standard deviations from Figure 6.9, i.e. along a diagonal in the front plane of the $LaBr_3$:Ce detector, are $\langle\sigma\rangle = 2.9/2.4/3.0$ mm for $E_\gamma = 59.5$ / $\sim$360 / 662 keV, respectively (and $\langle\sigma\rangle = 2.5$ mm for the case of the ^{241}Am data reconstructed with an ANN trained at 59.5 keV). The RMS error in the position reconstruction over the full area of the detector,

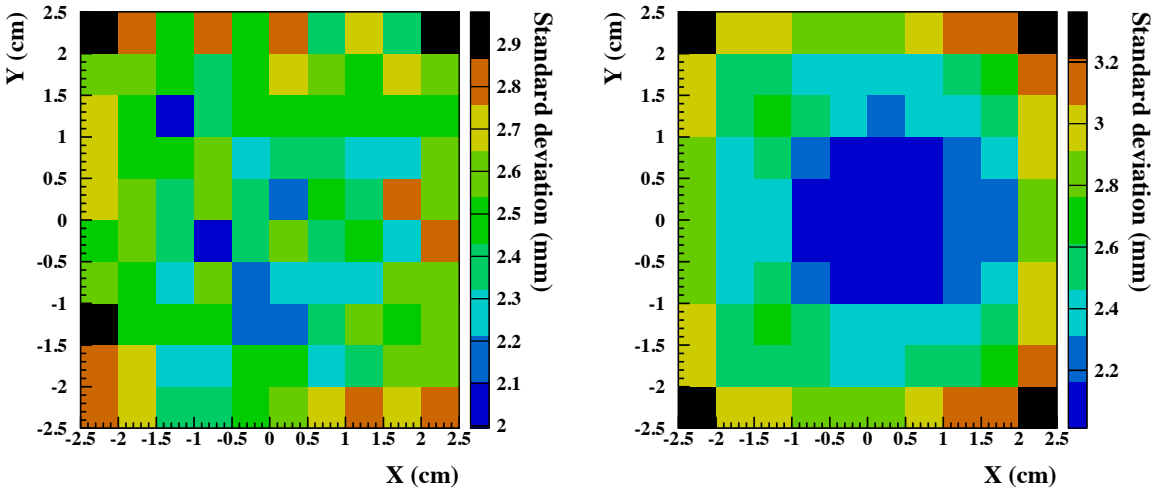

Figure 6.10: 2D distribution of the RMS error of the first gamma-ray interaction position, averaged for both coordinates X and Y, as a function of position on the front plane of the crystal. $Left$: RMS error distribution from simulated data shown in Fig. 5.5 (Chapter 5); $Right$: RMS error distribution obtained using measured data from ^{133}Ba source as in Figure 6.9, and using the same ANN configuration as for the left panel of the current Figure.

shown in Figure 6.10 (right panel), is estimated using also the horizontal and vertical scans of the $LaBr_3$:Ce detector with the ^{133}Ba source (see middle panel of Figure 6.4). The average σ-value over the full area of the detector is estimated to be $\langle\sigma\rangle \approx 2.6$ mm at $E_\gamma \sim 360$ keV. This value is comparable to (but slightly above) that given by the validation process of the ANN using simulated data: $\langle\sigma\rangle = 2.5$ mm (see Sect. 4.2 and Figures 5.3 and 5.4). This confirms that the simulated data are very similar to the experimental ones, and shows that a detailed Geant4 simulation of the $LaBr_3$:Ce detector can give an almost optimal result for the ANN method. In particular, the position resolution obtained with this method is significantly better than that provided by the Anger logic algorithm (see Figure 6.3). The final resolution we obtain is most likely limited by intrinsic properties of the detector, such as the size of the PMT pixels (6.25 mm, see Chapter 5).

Furthermore, we compare in Figure 6.10 the RMS errors of the position reconstruction distributed over the detector front plane for the case of simulated (*left*) and measured (*right*) data. Even though the average RMS error values over the detector surface are almost equal ($\langle\sigma\rangle = 2.5$ mm for the simulated data and $\langle\sigma\rangle = 2.6$ mm for the experimental data), we observe a clear difference in the 2D distributions between the two cases. When using experimental data, the RMS error values are significantly lower within the central $\approx 1\times1$ cm^2 detector area ($\sigma \sim 2$ mm) and higher near the edges and in the corners ($\sigma \sim 3$ mm and above). On the other hand, the 2D distribution from simulated data is more uniform, with the majority of values being close to the average RMS error value of 2.5 mm (green squares in the left panel of Fig. 6.10).

The green dotted curve in Figure 6.9 shows the position resolution we get with the $CeBr_3$ detector using the same ANN training configuration as for the $LaBr_3$:Ce module. The average standard deviation from this curve is $\langle\sigma\rangle = 3.3$ mm, which is significantly worse than the result obtained with the $LaBr_3$:Ce detector ($\langle\sigma\rangle = 2.4$ mm for the diagonal series of measure-

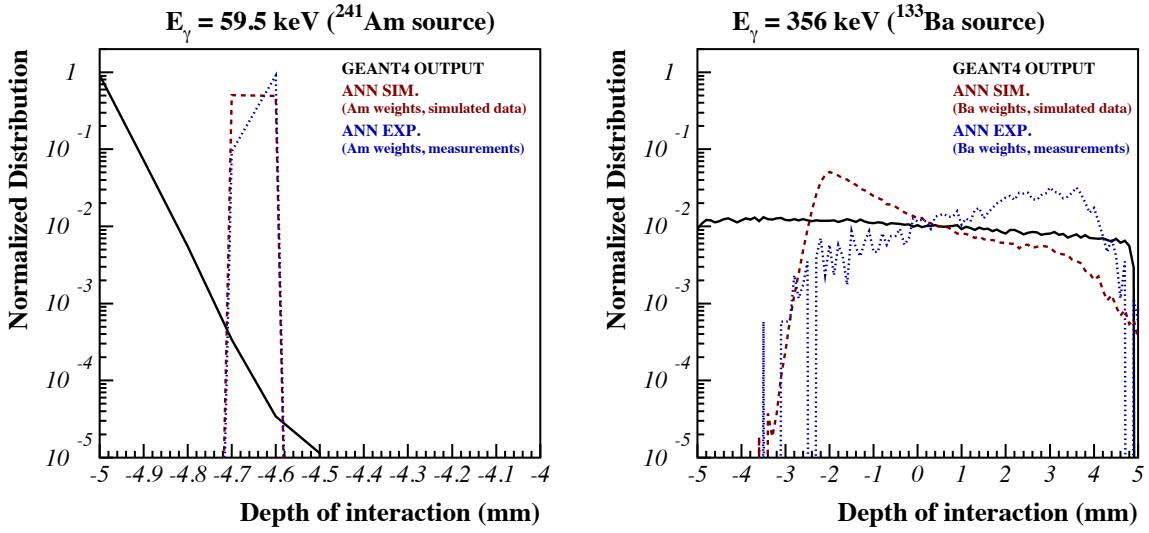

Figure 6.11: DOI of gamma-rays in the $LaBr_3$:Ce module obtained with the ANN method. The black and red curves were already shown in Figure 5.6: they correspond to DOI values obtained from the Geant4 simulation and to those reconstructed from the ANN method, respectively. The blue curves show the reconstructed DOI using experimental data. $Left$: both experimental and simulated data were obtained with $E_\gamma = 59.5$ keV (^{241}Am radioactive source), and the ANN was trained with simulated gamma rays of the same energy; $Right$: experimental data were obtained with $E_\gamma \sim 360$ keV (from the lines at 356 and 384 keV from the ^{133}Ba source), simulated data with $E_\gamma = 356$ keV and the ANN was also trained with $E_\gamma = 356$ keV gamma rays. In both cases, the ANN training was done using the Geant4 configuration of "Simulation 2" (see text and Chapter 5 for details).

ments with ^{133}Ba). In particular, we see that the reconstruction is worse for positive $X_{\rm POS}$ and $Y_{\rm POS}$ than for negative positions, as already identified in Figure 6.6. To improve the position resolution for this detector, it will likely be necessary to modify the ANN training process by using a large set of experimental data, instead of Geant4 simulated data. This will be studied in a future work with a dedicated scanning test bench.

6.1.4 Depth-of-interaction reconstruction

To further test the performance of the ANN in reconstructing the depth-of-interaction (DOI), we used several measured data sets from our scanning measurement series. To study the detector response at low energies, we used gamma rays of 59.5 keV from the ^{241}Am source. The source was collimated giving a radioactive beam perpendicular to the $X_{\rm POS} = Y_{\rm POS}$ = 0 mm position in the detector plane. We recorded approximately $4{\times}10^4$ events during this measurement. However, it is important to emphasize again that we used this experimental data only as an input to test the ANN response for the 3D imaging. We were unable to directly measure the DOI of gamma rays within the detector modules.

The results for 59.5 keV gamma rays are shown in the left panel of Figure 6.11. We see that the ANN performance follows the same trend for both simulated and measured data sets, placing the reconstructed values at several tenths of a millimeter depth within the crystal. As

previously concluded, the shift from the edge, where we see a majority of the interactions occuring in the Geant4 simulation, is due to the limited performance of the ANN near the crystal surface.

The blue curve in the right panel of Figure 6.11 shows the ANN response for the reconstruction of the DOI using measured data with $E_\gamma \sim 360$ from the ^{133}Ba source. The measurement was done in the same way as with the ^{241}Am source, and we recorded approximately 2000 full-energy events. The reconstructed experimental data show a similar trend to the simulated ones, both distributions being shifted by several millimeters from the front face of the detector. The reconstructed distribution from experimental data, although not as flat as the one obtained from Geant4, demonstrates the expected behavior of high-energy gamma-rays to interact within the full volume of the detector.

6.2 Energy characterization

To study the energy response of our detector modules we use several X- and γ-ray lines. The energy spectra are obtained by summing the 64 charge values after applying a correction for the non-uniformity of the gain of the PMT anodes (see Fig. 3.8 in Chapter 3). All sources with respective energies and measured full widths at half maximum (FWHM) for both modules are listed in Table 6.1. The Ag Kα line has been produced by irradiating a silver plate of 0.5 mm thickness with a slightly collimated source of ^{241}Am, in order to induce an Ag fluorescence emission. The observed peak at $\sim$ 23 keV (Fig. 6.12) results from the merging of the Ag Kα and Kβ lines at 22.1 and 25.0 keV, respectively. It has been fitted by two Gaussian functions imposing equal widths and a Kβ/Kα amplitude ratio of 0.19.

The second line from Table 6.1, the Cs Kα line at 30.85 keV is emitted by the ^{133}Ba source (electron capture decay). The observed peak has also been fitted by two Gaussians to take into account the emission of Kβ X-rays at 35.1 keV with imposed amplitude ratio of 0.22 (*Khazov et al.*, 2011).

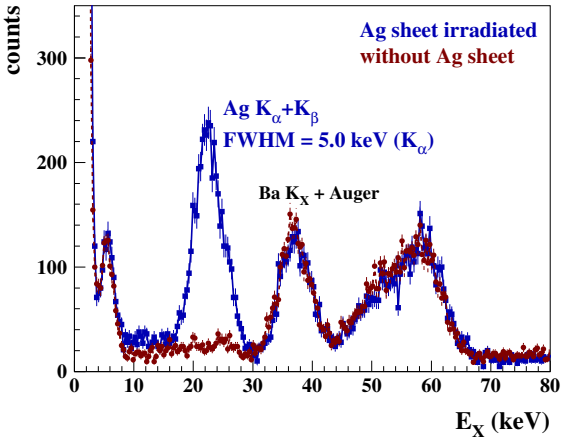

Figure 6.12: Blue symbols: energy spectrum obtained with the $LaBr_3$:Ce detector from the irradiation of a silver plate with a collimated ^{241}Am source. Red symbols: spectrum measured under the same conditions but without the silver plate. The structure above the K X-ray lines of Ag and Ba is due to 59.54-keV γ rays reaching the detector directly and/or indirectly by coherent and incoherent scattering. The two spectra have been obtained with a high-voltage power supply on the MAPMT of HV $= 1000$ V.

The peak composed of Ba K X rays + Auger electrons ($E_X = 37.44$ keV $\equiv$ K-shell binding energy) is observed in the self-counting emission spectrum of $LaBr_3$:Ce and is produced in the electron capture decay of ^{138}La (natural abundance of 0.09%) inside the crystal. This peak is therefore non existent in the background spectrum of $CeBr_3$.

The other lines in Table 6.1 are intense γ-ray lines produced by the standard radioactive sources listed in the first column.

6.2.1 Energy dynamic range

The ability to detect small energy deposits with the $LaBr_3$:Ce detector is illustrated in Fig. 6.12. We see that the Ag K X-ray line at $\sim$ 23 keV can be easily detected. In the same Figure, we additionally see another line just above the electronic noise, which is also observed in measurements without any (external) radioactive source. This line, which is not observed with the $CeBr_3$ detector, is most likely from the internal decay of ^{138}La proceeding by L-shell electron capture. Its centroid is at 5.4 keV, compatible with the range of binding energies of L-shell electrons in Ba (5.25 – 5.99 keV).

We also tried to detect Cu X rays ($E_X = 8$ keV for Kα X rays) by irradiating a Cu disk with the same experimental setup as for the production of Ag K X rays. However, no structure indicating 8 keV photon emission was observed in the recorded spectrum. This may partly be explained by a lower production efficiency of Cu fluorescence X-ray lines with the ^{241}Am source compared to Ag. But the main reason is the strong absorption of 8 keV photons in the housings of both the $LaBr_3$:Ce and $CeBr_3$ detectors: the transmission through 0.5 mm of Al calculated with the photon cross section database of NIST (*Berger et al.*, 2010) amounts to 69% for Ag Kα X rays, but only to 0.13% for Cu Kα X rays. Obviously, for a power supply of the MAPMT of HV $= 1000$ V, the detection threshold of both modules is limited by absorption in the entrance window rather than by the electronic noise.

The response of the detectors to relatively high-energy γ-rays is studied with a ^{60}Co source. We first perform a measurement with the $LaBr_3$:Ce detector and with HV $= 1000$ V that clearly shows two lines at 1173.2 and 1332.5 keV, but with a worse resolution than expected (see Table 6.1 and Fig. 6.15). We interpret this result as due to an electronic saturation of some MAPMT channels and then perform another measurement with HV $= 900$ V. The corresponding spectrum is shown in Figure 6.13 and the observed FWHM of the 1173.2 and 1332.5 keV lines is given in Table 6.1. Thus, for HV $= 900$ V, the $LaBr_3$:Ce detector is working properly between ~ 15 keV and ~ 1.3 MeV, which is a satisfactory dynamics for use in a small Compton telescope.

With the $CeBr_3$ detector, a saturation effect is also observed with HV $= 1000$ V for the γ-ray lines of the ^{60}Co source, but to a lesser extend than with the $LaBr_3$:Ce module. Thus, with the $CeBr_3$ detector, the measured FWHM of the ^{60}Co lines is higher by no more than ~ 25 – 30% than the expected values from a fit to the data at lower energies (see Sect. 6.2.2 below and Fig. 6.15). This is simply because $CeBr_3$ is producing less scintillation light than $LaBr_3$:Ce: 45 photons keV^{-1} for the former versus 63 ph keV^{-1} for the latter.

6.2.2 Energy resolution

To optimize the energy resolution, to each event we apply a correction on the total charge depending on the location of the γ-ray energy deposit inside the crystal. Indeed, we observe, from both the Geant4 simulation and the measurements that less charge is collected by the MAPMT if a γ-ray photon interacts closer to the border of the detector (see, e.g., Tables 4.1 and

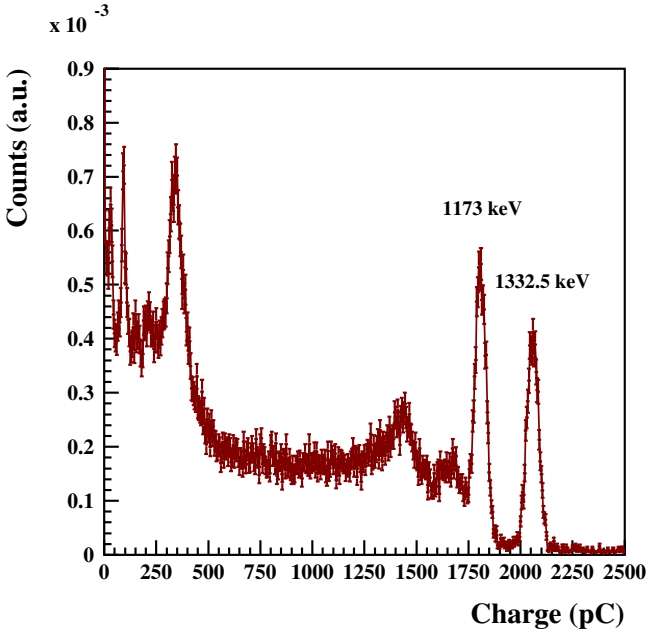

Figure 6.13: Total charge spectrum recorded with the ^{60}Co source. The measurement is done with a high voltage of HV $= 900$ V.

Line origin	Line energy (keV)	$LaBr_3$:Ce FWHM(keV)	$CeBr_3$ FWHM(keV)
Ag Kα X ray	22.1	5.4	7.2
Cs Kα X ray	30.85	6.0	8.31
Ba K X ray + Auger	37.44	5.4	-
γ ^{241}Am	59.54	6.9	10.52
γ ^{133}Ba	80.9	8.3	11.80
γ ^{133}Ba	276.4	16.5	22.23
γ ^{133}Ba	302.9	16.5	22.23
γ ^{133}Ba	356.0	18.2	23.81
γ ^{133}Ba	383.8	18.2	28.81
γ ^{137}Cs	661.7	24.9	31.72
γ ^{60}Co	1173.2	58.5 (36.8)	56.39
γ ^{60}Co	1332.5	63.23 (41.7)	63.75

Table 6.1: Studied X-ray and γ-ray lines with FWHM for both detector modules. In the fit of the ^{133}Ba spectrum, equal Gaussian widths were imposed for the lines at 276.4 and 302.9 keV, and for those at 356.0 and 383.8 keV. All data were acquired with a high-voltage power supply on the MAPMT of 1000 V. The results of a measurement with the $LaBr_3$:Ce detector and HV $=$ 900 V are shown for the ^{60}Co lines at 1173.2 and 1332.5 keV by the values in parenthesis.

4.2). The 2D position of each γ-ray hit is estimated with the Anger logic method described in Sect. 6.1.1. We divide the measured charge by a second-order polynomial correction factor depending on the distance r from the detector center expressed in mm, $r = \sqrt{X_{\mathrm{POS}}^2 + Y_{\mathrm{POS}}^2}$. For the $LaBr_3$:Ce detector, the correction function is given by:

$$f_Q = 1 - 1.76 \times 10^{-3} \times r + 5.82 \times 10^{-7} \times r^2 \,. \tag{6.1}$$

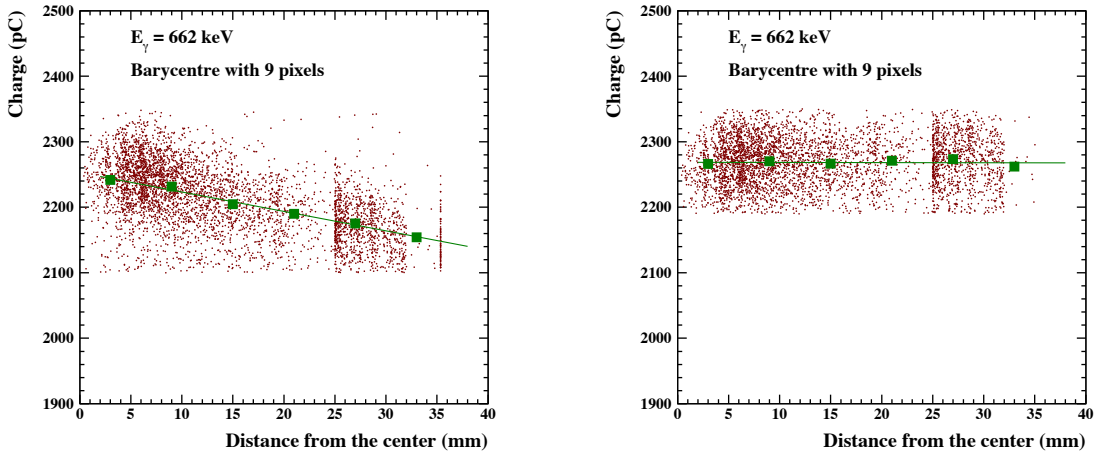

Figure 6.14: Experimentally recorded events from uncollimated ^{137}Cs source. The left panel corresponds to an uncorrected charge spectrum, where we select events from the full energy peak at E_γ=661.7 keV by choosing a corresponding window in the charge spectrum (2100–2350 pC). A clear trend is visible: the larger the distance from the center of the detector r [mm] the less charge is collected. The green points on the graph present the average charge collected for all events with the reconstructed position less than $r = 3, 9, 15, 21, 27$ and 33 mm. After fitting the data we are able to find a correction function f_Q from the fit. On the right is the same plot after the correction is applied. The selection window is narrower (2200–2350 pC), which indicates that the full-energy peak is also narrower. The fit now shows a horizontal flat trend, which directly improves the final energy resolution.

This correction is demonstrated in Figure 6.14. It significantly improves the energy resolution, e.g. at 661.7 keV from 4.9% to 3.6% for the $LaBr_3$:Ce detector and from 5.5% to 4.8% for the $CeBr_3$ module.

The energy resolution obtained after position reconstruction is shown in Figure 6.15. In total we give results for three sets of measurements: the first set is for measurements performed with the $LaBr_3$:Ce detector in summer of 2013 (blue data points), the second is for measurements with the same detector in autumn of 2014 (green data points), and the third is for measurements with the $CeBr_3$ detector in spring of 2015 (yellow data points). The consistency of the results obtained with the $LaBr_3$:Ce detector in 2013 and 2014 demonstrates the good stability of this module over time.

The data for all three sets can be well fitted between 59.5 and 662 keV with functions proportional to $\sqrt{E}$, which shows that the resolution is dominated by the statistical uncertainty in this energy range. At higher energies, the ^{60}Co data points at 1173 and 1332 keV deviate significantly from the general trend, even using HV $= 900$ V for the $LaBr_3$:Ce detector (Fig. 6.15), which is most likely due to a residual saturation of the readout electronics. Below 59.5 keV, the measured FWHM of the Ag and Cs Kα lines at 22 and 31 keV are also above the fitted curve, which is probably due to the nonproportional scintillation response of both $LaBr_3$:Ce and $CeBr_3$ (e.g. *Quarati et al.*, 2013; *Khodyuk and Dorenbos*, 2010).

For the $LaBr_3$:Ce crystal, Saint-Gobain reports a FWHM of 3.0% for the 661.7 keV line from ^{137}Cs, measured with the High Quantum Efficiency PhotoMulTiplier (HQE PMT) Photonis XP5300B, which has a quantum efficiency (Q.E.) of ≈35 %. For the $CeBr_3$ detector, SCIONIX reports a FWHM of 4.6% for the same energy, 661.7 keV, measured with the HQE PMT Hama-

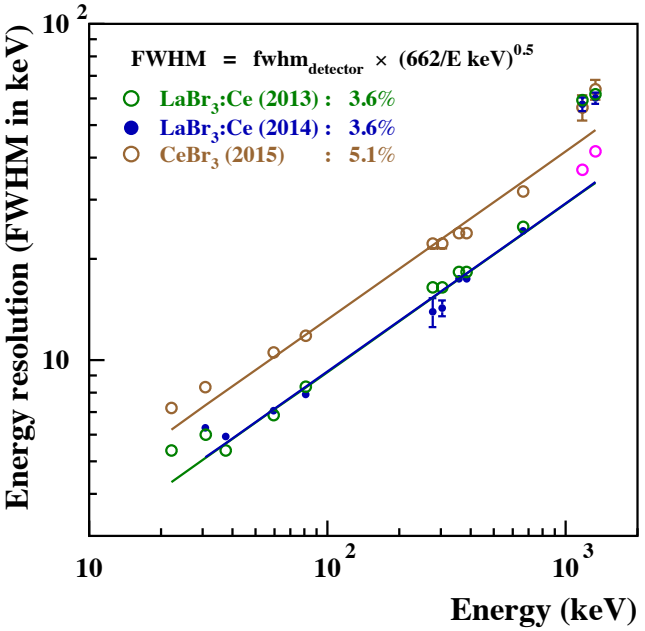

Figure 6.15: Energy resolution measured with the $LaBr_3$:Ce and $CeBr_3$ detectors. The green and blue data points give the performance for $LaBr_3$:Ce measured in 2013 and 2014, respectively. The data in yellow are for the $CeBr_3$ detector. All the experimental data were obtained with a high voltage power supply of the MAPMTs of 1000 V, except for the ^{60}Co data points in pink that show the results obtained with the $LaBr_3$:Ce in 2013 using $\mathrm{HV} = 900$ V. The straight lines show best fits to the data between 59.5 and 662 keV with functions proportionnal to $\sqrt{E}$. The resulting values of $\mathrm{fwhm}_{\mathrm{detector}}$ (the best-fit relative resolution at 662 keV) are of 3.6% ($LaBr_3$:Ce in 2013), 3.6% ($LaBr_3$:Ce in 2014) and 5.1% ($CeBr_3$ in 2015), as given on the plot.

matsu R6233 (Q.E. $\approx 35\%$). We confirmed both results in separate tests performed under the same conditions. The slightly higher FWHM values we measure with the MAPMT modules (3.6% and 5.1% for $LaBr_3$:Ce and $CeBr_3$, respectively) may be explained by the lower quantum efficiency of the H8500C MAPMTs compared to the PMTs used by the manufacturers. Nevertheless, the spectral resolution we reach with both detector modules is well within the requirements for our Compton telescope project.

Conclusions and perspectives

We aimed to study a novel instrumental concept for detection of medium energy gamma-rays. For this purpose, we developed and tested a prototype of scintillation detector module, capable of 3D imaging and calorimetry of gamma-rays between 10 keV and 10 MeV. Utilization of innovative detector materials allowed us to construct a prototype of a so called Advanced Compton Telescope (ACT), an instrument which operates by exploiting Compton scattering interactions in order to detect gamma rays and localize their source in the sky.

The intended primary application of the studied ACT prototype is space born gamma-ray astronomy. The operating energy range of such a prototype is the so-called MeV range, mainly from 100 keV up to 10 MeV. However, the prototype is further meant to be a building block for a bigger, more complex instrument, contending to become a candidate for ESA's future medium-sized mission for gamma-ray astronomy. In this light, a working prototype has to perform with satisfactory results in order to correctly assess the performance of the large scale instrument. The main target is to achieve an improvement of instrumental sensitivity compared to what is available today, bringing it to a level of at least 30 to 50 times better than the sensitivity of previous MeV gamma-ray instruments such as CGRO/COMPTEL and INTEGRAL/SPI. Inventive techniques needed to be developed and tested in order to solve the existing detection challenges in the MeV range. Gamma rays of these energies are hard to study and detect with current instruments due to reasons we discussed in Chapter 1. This leads to a high disproportion and a noticeable lack of observations when MeV range is compared to other energy ranges. Having in mind the grand scale of the future space mission, two international collaborations were formed in the last two years, first AstroMeV[1] and then the presently active ASTROGAM[2], with both working on the development of gamma-ray space-born instrumentation.

Our collaboration in Orsay designed, assembled and fully tested all of the individual components of the ACT prototype such as detectors, readout electronics and data analysis methods. Furthermore, we aim to fully characterize the completed prototype, whose assembly is, at the moment of submitting this manuscript, not yet finalized, but well under way.

The first of the two main parts of this prototype is a charge particles tracker made out of DSSSD detectors. These detectors provide the capability for high-precision tracking of both the electron and the gamma-ray from Compton scattering. The work on testing and commissioning the tracker was done by the IPNO and APC laboratories. In particular, the DSSSD BB7 version 2 of Micron Semiconductor Ltd studied at IPNO is now readout with a homemade front-end electronics board carrying two low-noise ASICs[3] and it is fully operational, providing satisfactory performance (see Chapter 2). The second main component of the ACT prototype, a calorimetric module capable of 3D imaging, was developed by our group at CSNSM Orsay and comprises the majority of the work presented in this thesis.

[1] See `http://astromev.in2p3.fr/`

[2] See `http://astrogam.iaps.inaf.it/`

[3] The selected ASIC is the chip VA32TA7 from the Ideas company, see: `http://ideas.no/`

We studied the performance of novel detectors made of new scintillators, $LaBr_3$:Ce or $CeBr_3$, coupled to a 64-channels MAPMT. We developed a dedicated detector test bench, with the possibility to interchange the two tested modules and a customized readout electronics and data acquisition system, to study the position resolution of the first hit of an incident γ-ray within the scintillation crystal, as well as the energy response of the module. We also performed a one-photoelectron calibration of an MAPMT to measure both the pixel-to-pixel gain and the mean gain of the PMT.

Next, we developed a detailed Geant4 simulation of the experimental setup that includes the tracking of the near-UV photons produced in the scintillation crystal and the creation of photoelectrons at the PMT photocathode. We studied in particular various models for photon reflection at interfaces between volumes and finally found a best match between simulated and measured charge distributions with a model of diffuse Lambertian reflection from all crystal surfaces. However, the simulation that reproduces at best the shape of the measured charge distributions systematically underproduces the overall charge by 15–20%.

The γ-ray hit localization was studied from the measured charge distributions using an ANN trained with Geant4 simulated data. The process is somewhat more complex to setup than an Anger-like method based on a center-of-gravity calculation, but after the network has been prepared it becomes a simple tool to use: the ANN training results in a one file with matrix of weights values, which is later easily implemented in any position reconstruction code. Furthermore, the position resolution obtained with the ANN method is found to be significantly better than that provided by an Anger logic algorithm. We achieved a mean resolution for the position of interaction on the front plane of the detector of ≈ 2.6 mm (1σ value) for γ-rays of 360 keV (^{133}Ba source). Using the same ANN, which was trained with simulated events from incident γ-rays of 356 keV, we also obtained a satisfactory position reconstruction accuracy for two other γ-ray energies, from data acquired with radioactive sources of ^{241}Am ($E_\gamma = 59.5$ keV) and ^{137}Cs ($E_\gamma = 662$ keV). Thus, in the central 9 cm^2 area of the detector, the measured 1σ resolution values are between 2.0 and 3.3 mm for the three γ-ray energies. For the ^{241}Am and ^{137}Cs data, the resolution is lower in the outer area of the detector (see Figure 6.9). But all in all, we expect that the obtained spatial resolution with this ANN will be adequate for the small Compton telescope with the mechanical integration of the $LaBr_3$:Ce module to the telescope prototype being completed.

The depth of interaction (DOI) reconstruction capabilities of the ANN were tested using simulated and experimental data. The returned results, shown on Figure 6.11, show a positive trend when compared with the depth of interaction obtained from the Geant4 simulations. The reconstructed DOIs corresponding to the low 59.5 keV and the higher 360 keV energy gamma-rays follow the expected distributions, with interactions placed in the first several millimeters and over the whole thickness of the $LaBr_3$:Ce, respectively. Nevertheless, we did not experimentally study the resolution in the depth of interaction inside the crystal, because the test bench we used is not suitable for this. However, the performance returned by the validation process of the ANN using simulated data is promising: $\sigma_Z = 2.2$ mm for 356 keV γ-rays (see Figure 5.3). We hope to experimentally confirm this result in the near future.

The dynamic range of the $LaBr_3$:Ce detector with its customized front-end electronics allows us to both detect and identify lines of interest in the desired energy range. This is demonstrated by detecting low energy X-rays from irradiated Ag sheet at 22.1 keV and by detecting γ-ray lines from ^{60}Co at 1.1 and 1.3 MeV. The energy resolution of the module is comparable to the optimal resolution of the cylindrical $LaBr_3$:Ce detector, being only approximately 25% higher. The result we obtain for the 662 keV line, 3.6% FWHM, is fitting and in agreement with the results we require from such a module. The stability of the detector over time is also entirely satisfactory.

Overall, the results we present on the performance of the $LaBr_3$:Ce module show that its characteristics make it a good candidate for a γ-ray astronomy instrument working in the 0.1 up to 10 MeV energy domain. However, the intrinsic radiation of $LaBr_3$:Ce, which is due to ^{138}La (half-life $T_{1/2} = 1.02 \times 10^{11}$ yr; natural abundance 0.09%), can be an important source of background for a space instrument. Therefore, we also studied a $CeBr_3$ + MAPMT detector using the test bench and readout electronics initially developed for the characterization of the $LaBr_3$:Ce module.

The energy resolution of the $CeBr_3$ detector is worse than that of the $LaBr_3$:Ce module by a factor of 1.4 (5.1% FWHM at 662 keV versus 3.6% for $LaBr_3$:Ce; see Figure 6.15). Such a factor is consistent with the difference in spectral resolution measured with cylindrical detectors (*Quarati et al.*, 2013). The position resolution obtained with the $CeBr_3$ detector is also worse than that of the $LaBr_3$:Ce module. Using the same ANN training configuration as for the $LaBr_3$:Ce detector, the average standard deviation of the X–Y 2D positions measured along a diagonal in the front plane of the $CeBr_3$ module was found to be $< \sigma >= 3.3$ mm. This result could be improved by optimizing the simulated data used for the ANN training, i.e. by undertaking a detailed parametric study of the Geant4 simulation for this detector, as done for the $LaBr_3$:Ce module. However, our $CeBr_3$ detector shows a non-uniform response as a function of irradiation position (see Figure 6.6), which could be difficult to take into account in the Geant4 simulation. For such a detector it should be preferable to use experimental scanning data for the ANN training process, rather than simulated data. An automatic detector scanning system with a collimated pencil gamma-ray beam will be developed in the future for this purpose.

Once the BB7 DSSSD and the $LaBr_3$:Ce detector have been fully qualified, we have tested extensive simulation performance of the Orsay ACT prototype, as well as of several larger scale concepts. The simulations were done in MEGAlib, aiming to show the energy response and angular resolution of the finished prototype. The simulations were based on the measured data, from both the tracker and the calorimeter test runs, and provide a realistic prediction of the prototype performances. The obtained results (see Chapter 2) are well within the requirements for a small sized Compton telescope, thus, the energy resolution amounts to about 10 keV FWHM at 662 keV and the corresponding angular resolution is ARM(FWHM) = 4.8°.

In the very near future of next 2 – 6 months, we are aiming to complete the prototype assembly and perform extensive testing on its imaging and spectral capabilities. We wish to obtain the full characterization of the prototype which would allow the comparison of its energy and position resolution performances to the results obtained with MEGAlib simulations. This will give further insight on the goodness of such concept for the future space applications.

In the longer term, during the next five years, with the collaboration of CNES and of several french laboratories including APC, AIM (CEA/DSM/IRFU/SAp), IPNO, and IRAP, we would like to prepare a stratospheric balloon experiment dedicated to the polarimetry measurement of bright X-ray sources, such as the Crab nebula and pulsar, in the 0.1 – 2 MeV range. The instrument would be a fully operational ACT optimized for polarization measurement. In addition, the balloon flight would allow us to test the performance of all of the detectors and readout electronics in a realistic surroundings (i.e. outside laboratory conditions) which, apart from bringing realization challenges, will hopefully be an invaluable opportunity to further test the envisioned ACT concept by performing observational measurements. A preliminary design of the envisioned polarimeter, named ComPol, which was proposed to CNES in 2015 (PI: Philippe Laurent), is shown in Figure 6.16.

The overall simulated instrument weights 64 kg and contains:

1. Tracker volume (dark blue slabs); made out of 8 layers of 4 DSSSD. Each DSSSD has

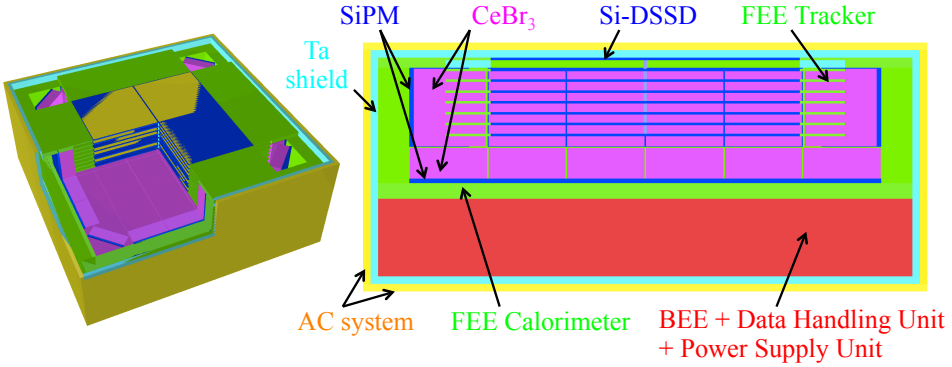

Figure 6.16: A studied model of the ComPol project, a full ACT prototype aimed to be launched in a stratospheric balloon mission to study the emission and polarization of bright X-ray sources such as the Crab nebula.

64×64 strips, covers an area of 10×10 cm^2 and is 1.5 mm thick. The spacing between the layers is 7 mm, and the electronic noise is FWHM = 5 keV.

2. Bottom calorimeter volume (pink); the calorimeter is made out of ∼14 kg of $CeBr_3$ crystals (with the similar or better performance expected of $LaBr_3$:Ce). It is made out of 6×6 monolithic crystal blocks, 50×50×20 mm^3 each. The calorimeter is read out by a set of arrays (1 per each crystal block, of 8×8 silicon photomultipliers. The modeled performance is based on energy performance of FWHM = 5% at 662 keV and the DOI resolution of FWHM = 4.7 mm.

3. Side calorimeter volume (pink); 12 $CeBr_3$ identical to the others, apart from being 1.6 mm thick.

4. Tantalum shielding (light blue); is a structure of 0.5 cm thick Ta plates, weighting a total of 27.6 kg.

5. Anti-coincidence shielding (yellow); it is made out of NE110 plastic scintillators which are 5 mm thick and cover all 6 sides of the instrument.

6. FEE (green) and BEE + Power Supply Unit + Data Handling Unit (red); total weight of 17.3 kg.

Using such geometry design in MEGAlib resulted in the following simulated performance of the ComPol model: the required effective observation time of the Crab nebula to detect at 3σ a polarization fraction of 50% (see: *Moran et al.*, 2013) is 6.5 min, 30.1 min, 4.8 h, 1.4 d, and 4.3 d, for photons in the energy ranges 80 – 250 keV, 250 – 500 keV, 500 – 750 keV, 750 – 1000 keV, and 1 – 2 MeV, respectively.

Another, more commercial application, is being realized for the Call for Proposals from the French National Agency for the Management of Radioactive Waste (ANDRA): "Optimization of post dismantling radioactive waste management". Through a project named ComptonCam, our collaboration in Orsay is currently working on an ultra sensitive, wide field gamma camera for localization and characterization of low-intensity radioactive waste. In short, it is a scaled model of the Compton telescope, which utilizes the developed calorimetry module, DSSSD detectors and electronics to create a small compact portable gamma camera.

Shaped on the space instrumentation background, ComtonCam, represented in Figure 6.17, aims to be the most sensitive portable gamma camera available, being, e.g., approximately 90

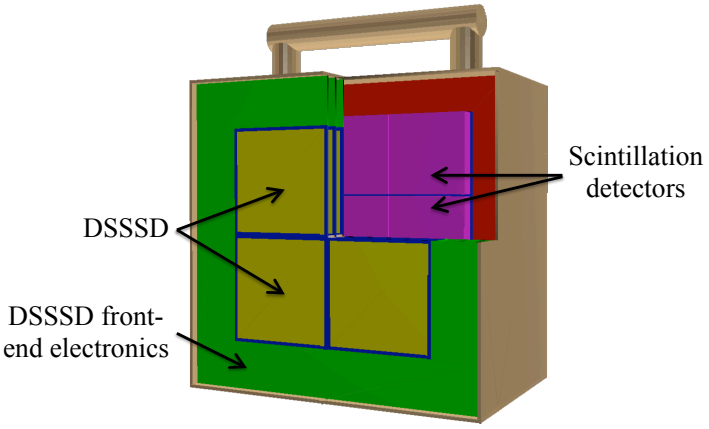

Figure 6.17: MEGAlib geometry model of the ComptonCam portable gamma camera projetc. In the front we see DSSSD detectors (yellow) with the corresponding FEE (green). Behind are the scintillation calorimeter modules (purple) with the BEE electronics in the far back (red).

times more sensitive than the similar instrument ASTROCAM 7000HS produced by Mitsubishi Heavy Industries (in collaboration with scientists from the Japonese Space Agency JAXA) after the Fukushima disaster (*Matsuura et al.*, 2014). In practice, localization of a source, emitting at a dose equivalent rate of 100 nSv/h (similar to the level of natural radioactivity in France), can be done with ComptonCam, within just 10 seconds. Such high level performance projections are based on studied models and simulations. From the MEGAlib model (Fig. 6.17), we obtained an energy resolution of FWHM = 5.1% and an angular resolution of FWHM = 5.6° for 662 keV gamma-rays. In addition, the compact design, corresponding to the ACT design, gives ComptonCam a very large field of view, close to 2π sr.

Finally, the total presented work shows that the 3D imaging modules, as well as astrophysical instrument designs based on them, play a key role in progress of the overall space-born instrumentation development, encouraging exploration of new detector design concepts and pushes forward detector capabilities by exploiting newest available materials. Furthermore, such work has the potential to be applied in more commercial fields, such as environmental surveys and security.

Appendix A

Defining geometry for the simulation of the $LaBr_3$:Ce module

We attach a partition of code from used Geant4 simulation, containing the full detector geometry and explored parametrization of the optical surfaces. The $LaBr3DetectorGeometry.cc$ file corresponds to the "Simulation 2" configuration, (Chapter 4), and was adopted for tests of the $LaBr_3$:Ce detector with the ^{133}Ba source. Same configuration was used for generating the training data of the ANN (Chapter 5).

```
//////////////////////////////////////////////////////////////////
//                                                              //
//            L a B r 3 : Ce   simulation                       //
//                                                              //
// Defining elements and geometry for the LaBr3:Ce module       //
//                                                              //
// Main volumes:                                                //
//      experimental hall : world volume                        //
//      scintillator      : LaBr3:Ce, 10 mm thick               //
//      optical window    : Borosillicate glass, 5 mm thick     //
//      PMT volume        : Borosilicate glass;                 //
//                          Bialkali photocathode inside        //
//      g-ray collimator  : Lead, 57 mm thick, 3 mm diam. hole  //
//                                                              //
// Surfaces:                                                    //
//      Surface 1: interface btwn. scintillator and opt.window  //
//                 UNIFIED, dielectric_dielectric, ground       //
//      Surface 2: crystal+op. windowd border sides;            //
//                 ground and wrapped in Teflon-97% reflec.     //
//      Surface 3: interface btwn opt. window and PMT volume    //
//                 UNIFIED, dielectric_dielectric, polished     //
//      Surface 4: PMT vol. border sides (except detect. side)  //
//                 100% opaque : kills the photons              //
//                                                              //
//                                                              //
// Version: Oct. 2015                                           //
//                                                              //
// created by:   A. Gostojic; V. Tatischeff                     //
// affiliation:  CSNSM, Orsay; University Paris Saclay; CNRS    //
//////////////////////////////////////////////////////////////////

#include "Labr01DetectorConstruction.hh"
#include "Labr01ScintillatorSD.hh"
#include "Labr01PhotocathodeSD.hh"

#include "G4Material.hh"
#include "G4MaterialTable.hh"
#include "G4Element.hh"
#include "G4ElementTable.hh"
#include "G4OpticalSurface.hh"
#include "G4LogicalBorderSurface.hh"
#include "G4LogicalSkinSurface.hh"
#include "G4NistManager.hh"
#include "G4Box.hh"
#include "G4Tubs.hh"
#include "G4LogicalVolume.hh"
#include "G4RotationMatrix.hh"
#include "G4ThreeVector.hh"
#include "G4Transform3D.hh"
#include "G4PVPlacement.hh"
#include "G4SDManager.hh"
#include "G4OpBoundaryProcess.hh"

#include "G4UserLimits.hh"

#include "G4VisAttributes.hh"
#include "G4Colour.hh"

#include "G4ios.hh"
```

```
Labr01DetectorConstruction::Labr01DetectorConstruction():
  experimentalHall_box(0), experimentalHall_log(0), experimentalHall_phys(0),
  scintillator_box(0), scintillator_log(0), scintillator_phys(0),
  teflon_box(0), teflon_log(0), teflon_phys(0),
  par_box(0), par_log(0), par_phys(0),
  isolator_box(0), isolator_log(0), isolator_phys(0),
  collimatorPlate_box(0), collimatorPlate_log(0), collimatorPlate_phys(0),
  collimatorHole_tube(0), collimatorHole_log(0), collimatorHole_phys(0),
  collimatorTube_tube(0), collimatorTube_log(0), collimatorTube_phys(0),
  collimator_tube(0), collimator_log(0), collimator_phys(0),
  sourceBox_tube(0), sourceBox_log(0), sourceBox_phys(0),
  guide_box(0), guide_log(0), guide_phys(0),
  PMT_box(0), PMT_log(0), PMT_phys(0),
  photo_box(0), photo_log(0), photo_phys(0),
  dyno_box(0), dyno_log(0), dyno_phys(0),
  stepLimit(0)
{;}

Labr01DetectorConstruction::~Labr01DetectorConstruction()
{
  delete stepLimit;
}

G4VPhysicalVolume* Labr01DetectorConstruction::Construct()
{

  //---------------------Defining the materials used:

  G4double a;  // atomic mass
  G4double z;  // atomic number
  G4double density;
  G4int nel, natoms;
  G4double abundance;

  //Air
  G4Element* N = new G4Element("Nitrogen", "N", z=7., a= 14.01*g/mole);
  G4Element* O = new G4Element("Oxygen"  , "O", z=8., a= 16.00*g/mole);

  G4Material* Air = new G4Material("Air", density= 1.29*mg/cm3, nel=2);
  Air->AddElement(N, 70*perCent);
  Air->AddElement(O, 30*perCent);

  //LaBr3:5%Ce
  G4Element* La = new G4Element("Lanthanum", "La", z=57., a= 138.91*g/mole);
  G4Element* Br = new G4Element("Bromine"  , "Br", z=35., a= 79.90*g/mole);
  G4Element* Ce = new G4Element("Cerium"  , "Ce", z=58., a= 140.11*g/mole);

  G4Material* LaBr3 = new G4Material("LaBr3", density= 5.08*g/cm3, nel=2);
  LaBr3->AddElement(La, natoms=1);
  LaBr3->AddElement(Br, natoms=3);

  G4Material* LaBr3Ce = new G4Material("LaBr3Ce", density= 5.08*g/cm3, nel=2);
  LaBr3Ce->AddMaterial(LaBr3, abundance=95.*perCent);
  LaBr3Ce->AddElement(Ce, abundance=5.*perCent);

  //Aluminium
  G4Material* Al =
  new G4Material("Aluminum", z= 13., a= 26.98*g/mole, density=2.7*g/cm3);

  //Lead
```

```
  G4Material* Pb =
  new G4Material("Lead", z=82., a= 207.2*g/mole, density=11.34*g/cm3);

  //Glass
  G4Element* H = new G4Element("Hydrogen", "H", z=1., a=1.01*g/mole);
  G4Element* C = new G4Element("Carbon", "C", z=6., a=12.01*g/mole);

  G4Material* Glass = new G4Material("Glass", density=1.032*g/cm3,2);
  Glass->AddElement(C,91.533*perCent);
  Glass->AddElement(H,8.467*perCent);

  //Glass2
  G4Material* Glass2 = new G4Material("Glass2", density=1.032*g/cm3,2);
  Glass2->AddElement(C,91.533*perCent);
  Glass2->AddElement(H,8.467*perCent);

  //Teflon
  G4NistManager* man = G4NistManager::Instance();
  G4Material* Teflon = man->FindOrBuildMaterial("G4_TEFLON");

  // Print all the materials defined.
  //
  G4cout << G4endl << "The materials defined are : " << G4endl << G4endl;
  G4cout << *(G4Material::GetMaterialTable()) << G4endl;

//
// ------------ Material Properties Table for the LaBr3:Ce------------
//
// Parameters taken from:
// van Dam, Herman T. et. al.
// Optical absorption length, Scattering length and Refractive index
// IEEE Trans. on Nucl. Sci., vol 59, no. 3, June 2012

// Range of the emission spectrum:
// 460-(step 10)->410-(step 5)->340 nm

    const G4int nEntries = 20;
    const G4int nEntries2 = 22;

G4double PhotonEnergy2[nEntries] =
  { 2.695*eV, 2.755*eV, 2.818*eV, 2.884*eV, 2.952*eV,
    3.024*eV, 3.061*eV, 3.100*eV, 3.139*eV, 3.179*eV,
    3.220*eV, 3.263*eV, 3.306*eV, 3.351*eV, 3.397*eV,
    3.444*eV, 3.493*eV, 3.542*eV, 3.594*eV, 3.647*eV };

// Range of the absorption spectrum:
// 340-(step 1.)->360 nm + 460 nm for range equalization with the above

G4double PhotonEnergyABS[nEntries2] =
  { 2.695*eV, 3.444*eV, 3.454*eV, 3.463*eV, 3.473*eV,
    3.483*eV, 3.493*eV, 3.502*eV, 3.512*eV, 3.522*eV,
    3.532*eV, 3.542*eV, 3.553*eV, 3.563*eV, 3.573*eV,
    3.583*eV, 3.594*eV, 3.604*eV, 3.615*eV, 3.625*eV,
    3.636*eV, 3.647*eV };

// Fast emission spectrum of LaBr3:Ce:

G4double fastEmissionSpectrum2[nEntries] =
  { 0.000004, 0.00008, 0.0013, 0.0016, 0.0133,
    0.0758, 0.1522, 0.2692, 0.4152, 0.5540,
```

```
    0.6379, 0.6466, 0.6249, 0.6670, 0.8237,
    1.000, 0.9871, 0.6590, 0.2026, 0.0097 };

// Table of refractive indexes of LaBr3:Ce:

G4double refractiveIndex1[nEntries] =
  { 2.150, 2.161, 2.173, 2.187, 2.202,
    2.218, 2.227, 2.236, 2.246, 2.256,
    2.267, 2.279, 2.292, 2.305, 2.319,
    2.334, 2.350, 2.367, 2.386, 2.406  };

// Table of absorption length for LaBr3:Ce:

G4double Absorption1[nEntries2] =
  { 24*cm, 24*cm, 24*cm, 24*cm, 24*cm,
    24*cm, 24*cm, 24*cm, 24*cm, 24*cm,
    24*cm, 24*cm, 24*cm, 24*cm, 24*cm,
    24*cm, 24*cm, 24*cm, 24*cm, 24*cm };

// Absorption and reemission of the scintillation light
// simulated with the WLS Fiber mechanism
// - table of absorption length:

G4double AbsorptionABS[nEntries2] =
  { 99999.*mm, 1594.*mm, 1146.*mm, 827.1*mm, 599.1*mm,
    435.6*mm, 318.0*mm, 233.0*mm, 171.4*mm, 126.7*mm,
    93.98*mm, 70.03*mm, 52.41*mm, 39.40*mm, 29.76*mm,
    22.58*mm, 17.21*mm, 13.19*mm, 10.15*mm, 7.858*mm,
    6.112*mm, 4.779*mm };

// - table of reemission spectrum:

G4double EmissionABS[nEntries2] =
    { 0.000, 0.972, 0.991, 1.000, 0.998,
        0.985, 0.959, 0.919, 0.867, 0.802,
        0.725, 0.640, 0.549, 0.455, 0.362,
        0.274, 0.196, 0.131, 0.081, 0.045,
        0.022, 0.009, };

// Rayleigh scattering length for LaBr3:Ce:

G4double RayleighScattering[nEntries] =
  { 171*mm, 165*mm, 159*mm, 153*mm, 147*mm,
    141*mm, 138*mm, 135*mm, 132*mm, 129*mm,
    126*mm, 123*mm, 120*mm, 117*mm, 114*mm,
    111*mm, 108*mm, 105*mm, 102*mm,  99*mm };

// Setting the properties of the material for LaBr3:Ce

 G4MaterialPropertiesTable* LaBr3MPT = new G4MaterialPropertiesTable();
 LaBr3MPT->AddProperty("FASTCOMPONENT", PhotonEnergy2, fastEmissionSpectrum2,
     nEntries);
 LaBr3MPT->AddProperty("RINDEX", PhotonEnergy2, refractiveIndex1, nEntries);
 LaBr3MPT->AddProperty("ABSLENGTH", PhotonEnergy2, Absorption1, nEntries);
 LaBr3MPT->AddConstProperty("SCINTILLATIONYIELD", 63./keV);
 LaBr3MPT->AddConstProperty("RESOLUTIONSCALE", 1.0);
 LaBr3MPT->AddConstProperty("FASTTIMECONSTANT", 16.*ns);
 LaBr3MPT->AddConstProperty("YIELDRATIO",1.0);
 LaBr3MPT->AddProperty("RAYLEIGH", PhotonEnergy2, RayleighScattering, nEntries
     );
```

```
 LaBr3MPT->AddProperty("WLSABSLENGTH", PhotonEnergyABS, AbsorptionABS,
     nEntries2);
 LaBr3MPT->AddProperty("WLSCOMPONENT", PhotonEnergyABS, EmissionABS, nEntries2
     );
 LaBr3MPT->AddConstProperty("WLSTIMECONSTANT", 0.001*ns);

 LaBr3Ce->SetMaterialPropertiesTable(LaBr3MPT);

 //Air:

 //Refractive index of air:

G4double refractiveIndex2[nEntries] =
  { 1.0, 1.0, 1.0, 1.0, 1.0,
    1.0, 1.0, 1.0, 1.0, 1.0,
    1.0, 1.0, 1.0, 1.0, 1.0,
    1.0, 1.0, 1.0, 1.0, 1.0 };

 G4MaterialPropertiesTable* airMPT = new G4MaterialPropertiesTable();
 airMPT->AddProperty("RINDEX", PhotonEnergy2, refractiveIndex2, nEntries);

 Air->SetMaterialPropertiesTable(airMPT);

 // Refractive index for optical window volume in the detector
 // for the material borosilicate glass,
 // From Saint Gobain private com (email of 15 June 2012):

G4double refractiveIndex3[nEntries] =
  { 1.472, 1.472, 1.472, 1.472, 1.472,
    1.472, 1.472, 1.472, 1.472, 1.472,
    1.472, 1.472, 1.472, 1.472, 1.472,
    1.472, 1.472, 1.472, 1.472, 1.472 };

 G4MaterialPropertiesTable* glassMPT = new G4MaterialPropertiesTable();
 glassMPT->AddProperty("RINDEX", PhotonEnergy2, refractiveIndex3, nEntries);

 Glass->SetMaterialPropertiesTable(glassMPT);

 // Entrance window of the PMT. From Hamamatsu: Borosilicate.
 // Refractive index from Motta & Schonert (2008), Eq. 9: ~1.5 at 380 nm

G4double refractiveIndex4[nEntries] =
  { 1.5, 1.5, 1.5, 1.5, 1.5,
    1.5, 1.5, 1.5, 1.5, 1.5,
    1.5, 1.5, 1.5, 1.5, 1.5,
    1.5, 1.5, 1.5, 1.5, 1.5 };

 G4MaterialPropertiesTable* glassMPT2 = new G4MaterialPropertiesTable();
 glassMPT2->AddProperty("RINDEX", PhotonEnergy2, refractiveIndex4, nEntries);

 Glass2->SetMaterialPropertiesTable(glassMPT2);

//
//------------------------------- volumes

  //------------------------ experimental hall (world volume)
  //------------------------ beam line along z axis

  G4double expHall_x = 30.0/2.*cm;
  G4double expHall_y = 30.0/2.*cm;
```

```
G4double expHall_z = 40.0/2.*cm;
experimentalHall_box
  = new G4Box("expHall_box",expHall_x,expHall_y,expHall_z);
experimentalHall_log = new G4LogicalVolume(experimentalHall_box,
                                           Air,"expHall_log",0,0,0);
experimentalHall_phys = new G4PVPlacement(0,G4ThreeVector(),
                                    experimentalHall_log,"expHall",0,false,0
                                        );

//--------LaBr3:Ce scintillator

G4double scint_x = 5.08/2.*cm;
G4double scint_y = 5.08/2.*cm;
G4double scint_z = 1.0/2.*cm;
scintillator_box = new G4Box("scint_box",scint_x,
                                         scint_y,scint_z);
scintillator_log = new G4LogicalVolume(scintillator_box,
                                           LaBr3Ce,"scint_log",0,0,0);
G4double scintPos_x = 0.0*cm;
G4double scintPos_y = 0.0*cm;
G4double scintPos_z = 0.0*cm;
scintillator_phys = new G4PVPlacement(0,
           G4ThreeVector(scintPos_x,scintPos_y,scintPos_z),
           scintillator_log,"scintillator",experimentalHall_log,false,0);


//---------------Teflon, 0.9 mm layer at the front side of the crystal
//---------------(see Hull et al. 2008, NIM Phys. Res A588, 384)

G4double tefl_x = scint_x;
G4double tefl_y = scint_y;
G4double tefl_z = 0.045*cm;

teflon_box = new G4Box("tefl_box",tefl_x,tefl_y,tefl_z);
teflon_log = new G4LogicalVolume(teflon_box,Teflon,"tefl_log",0,0,0);

G4double teflPos_x = 0.0*cm;
G4double teflPos_y = 0.0*cm;
G4double teflPos_z = -scint_z-tefl_z;
teflon_phys = new G4PVPlacement(0,
           G4ThreeVector(teflPos_x,teflPos_y,teflPos_z),
           teflon_log,"teflon",experimentalHall_log,false,0);

//----Glass layer (isolation) between the crystal and the Al housing:

G4double isol_x = scint_x;
G4double isol_y = scint_y;
G4double isol_z = 0.14/2*cm;

isolator_box = new G4Box("isol_box",isol_x,isol_y,isol_z);
isolator_log = new G4LogicalVolume(isolator_box,Glass,"isol_log",0,0,0);

G4double isolPos_x = 0.0*cm;
G4double isolPos_y = 0.0*cm;
G4double isolPos_z = -scint_z-2*tefl_z-isol_z;
isolator_phys = new G4PVPlacement(0,
           G4ThreeVector(isolPos_x,isolPos_y,isolPos_z),
           isolator_log,"Isolator",experimentalHall_log,false,0);

//------------------------------ Aluminium housing:
```

```
  G4double pa_x = scint_x;
  G4double pa_y = scint_y;
  G4double pa_z = 0.05/2*cm;
  par_box = new G4Box("pa_box",pa_x,pa_y,pa_z);

  par_log = new G4LogicalVolume(par_box, Al,"par_log",0,0,0);

  G4double pasPos_x = 0.0*m;
  G4double pasPos_y = 0.0*m;
  G4double pasPos_z = isolPos_z-isol_z-pa_z;
  par_phys = new G4PVPlacement(0,
             G4ThreeVector(pasPos_x,pasPos_y,pasPos_z),
             par_log,"par",experimentalHall_log,false,0);

//----- Position of the collimator (radioactive beam):

  //******* (X_pos, Y_pos) *******

  G4double Pos_x = +0.0*cm;
  G4double Pos_y = +0.0*cm;

  //*****************************

  //--- Pb collimator (57 mm thick for 133-Ba source, 356 keV g-rays):

  G4double innerRadiusOfTheT = 0.15*cm;
  G4double outerRadiusOfTheT = 3.0*cm;
  G4double hightOfTheT = 5.7/2*cm;
  G4double startAngleOfTheT = 0.*deg;
  G4double spanningAngleOfTheT = 360.*deg;

  collimator_tube = new G4Tubs("coll_tube",
                innerRadiusOfTheT,
                outerRadiusOfTheT,
                hightOfTheT,
                startAngleOfTheT,
                spanningAngleOfTheT);

  collimator_log = new G4LogicalVolume(collimator_tube,Pb,"collimator_log");

  // Added "-3 mm" as the collimator is 3 mm away from the front of the
      detector

  G4double collPos_z = pasPos_z-pa_z-0.1*cm-hightOfTheT;
  collimator_phys = new G4PVPlacement(0,
             G4ThreeVector(Pos_x,Pos_y,collPos_z),
             collimator_log,"collimator",experimentalHall_log,false,0);

  //----------------- Source Container:

  G4double innerRadiusOfBox = 0.0 *cm;
  G4double outerRadiusOfBox = 1.0*cm;
  G4double hightOfBox = 0.5*cm;
  G4double startAngleOfBox = 0.*deg;
  G4double spanningAngleOfBox = 360.*deg;

  sourceBox_tube = new G4Tubs("sourceBox",
                innerRadiusOfBox,
                outerRadiusOfBox,
```

```
                hightOfBox,
                startAngleOfBox,
                spanningAngleOfBox);

sourceBox_log = new G4LogicalVolume(sourceBox_tube,Air,"sourceBox_log");
G4double boxPos_z = collPos_z-hightOfTheT-hightOfBox;
sourceBox_phys = new G4PVPlacement(0,
           G4ThreeVector(Pos_x,Pos_y,boxPos_z),
           sourceBox_log,"sourceBox",experimentalHall_log,false,0);


 //-------------- Optical window volume, 5 mm thick glass:

G4double guide_x = scint_x+0.*cm;
G4double guide_y = scint_y+0.*cm;
G4double guide_z = 0.25*cm;

guide_box = new G4Box("guide_box",guide_x,guide_y,guide_z);
guide_log = new G4LogicalVolume(guide_box,Glass,"guide_log",0,0,0);

G4double guidePos_x = 0.0*cm;
G4double guidePos_y = 0.0*cm;
G4double guidePos_z = scint_z + guide_z;
guide_phys = new G4PVPlacement(0,G4ThreeVector(guidePos_x,guidePos_y,
    guidePos_z),
           guide_log,"LightGuide",experimentalHall_log,false,0);

//------------------------------
// PMT + Photocathode
//------------------------------

// PMT Simulated by glass bulk:

G4double PMT_x = scint_x+0.06*cm;
G4double PMT_y = scint_y+0.06*cm;
G4double PMT_z = 2.0/2*cm;

PMT_box = new G4Box("PMT_box",PMT_x,PMT_y,PMT_z);
PMT_log = new G4LogicalVolume(PMT_box,Glass2,"PMT_log",0,0,0);

G4double PMTPos_x = 0.0*cm;
G4double PMTPos_y = 0.0*cm;
G4double PMTPos_z = scint_z + 2*guide_z + PMT_z;
PMT_phys = new G4PVPlacement(0,G4ThreeVector(PMTPos_x,PMTPos_y,PMTPos_z),
           PMT_log,"LightPMT",experimentalHall_log,false,0);

// Following is a "dummy" volume (called dynode) defined as the sensitive
// detector for counting the optical photons

G4double dyn_x = PMT_x-0.15*cm;
G4double dyn_y = PMT_y-0.15*cm;
G4double dyn_z = 0.05*cm;

dyno_box = new G4Box("dyn_box",dyn_x,dyn_y,dyn_z);
dyno_log = new G4LogicalVolume(dyno_box,Al,"dyn_log",0,0,0);

G4double dynPos_x = 0.0*cm;
G4double dynPos_y = 0.0*cm;
G4double dynPos_z = -PMT_z+0.15*cm+dyn_z+0.1*cm;
```

```
  dyno_phys = new G4PVPlacement(0,G4ThreeVector(dynPos_x,dynPos_y,dynPos_z),
              dyno_log,"Dynode",PMT_log,false,0);

  // the "photocathode" is a metal slab inside the PMT glass

  G4double phot_x = dyn_x;
  G4double phot_y = dyn_y;
  G4double phot_z = 0.05*cm;

  photo_box = new G4Box("phot_box",phot_x,phot_y,phot_z);
  photo_log = new G4LogicalVolume(photo_box,Al,"phot_log",0,0,0);

  G4double photPos_x = 0.0*cm;
  G4double photPos_y = 0.0*cm;
  G4double photPos_z = dynPos_z-dyn_z-phot_z;

  photo_phys = new G4PVPlacement(0,G4ThreeVector(photPos_x,photPos_y,photPos_z
      ),
               photo_log,"Photocathode",PMT_log,false,0);

  //-----------------------------------------------
  // Sensitive detectors
  //-----------------------------------------------

  G4SDManager* SDman = G4SDManager::GetSDMpointer();

  G4String scintillatorSDname = "Labr01/scintillatorSD";
  Labr01ScintillatorSD* scintillatorSD = new Labr01ScintillatorSD(
      scintillatorSDname );
  SDman->AddNewDetector( scintillatorSD );
  scintillator_log->SetSensitiveDetector( scintillatorSD );

    //sensitive detector is not actually on the photocathode.
    //processHits gets done manually by the stepping action.
    //It is used to detect when photons hit and get absorbed&detected at the
    //boundary to the photocathode (which doesnt get done by attaching it to a
    //logical volume.
    //It does however need to be attached to something or else it doesnt get
    //reset at the begining of events

  G4String photoSDname = "/Labr01/photocathodeSD";
  Labr01PhotocathodeSD* photocathodeSD = new Labr01PhotocathodeSD( photoSDname
      );
  SDman->AddNewDetector( photocathodeSD );
  dyno_log->SetSensitiveDetector( photocathodeSD );

//-----------------------------------------------
//---------     Surfaces   ----------------------
//-----------------------------------------------

// Surface 1:

//----------------- Scintillator / optical window interface:

  G4double sigma_alpha_1 = 10.;

  G4double specularlobe2[NUM] = {0.0,0.0};
  G4double specularspike2[NUM] = {0.0,0.0};
  G4double backscatter2[NUM] = {0.0,0.0};
```

```
  G4OpticalSurface *OpCrystalGuide  = new
      G4OpticalSurface("CrystalGuidesurface");
  OpCrystalGuide->SetType(dielectric_dielectric);
  OpCrystalGuide->SetModel(unified);
  OpCrystalGuide->SetFinish(ground);
  OpCrystalGuide->SetSigmaAlpha(sigma_alpha_1);

  G4double guide_reflectivity[NUM] = {1.,1.};

  G4MaterialPropertiesTable* sGuide = new G4MaterialPropertiesTable();
  sGuide->AddProperty("SPECULARLOBECONSTANT", pp, specularlobe2, NUM);
  sGuide->AddProperty("SPECULARSPIKECONSTANT", pp, specularspike2, NUM);
  sGuide->AddProperty("BACKSCATTERCONSTANT", pp, backscatter2, NUM);
  sGuide->AddProperty("REFLECTIVITY", pp,guide_reflectivity, NUM);

  OpCrystalGuide->SetMaterialPropertiesTable(sGuide);

  G4LogicalBorderSurface* CrystalGuidesurface =
    new G4LogicalBorderSurface("",scintillator_phys,guide_phys,
    OpCrystalGuide);

  if(CrystalGuidesurface->GetVolume1() == scintillator_phys)
    G4cout << "Crystal is volume 1" << G4endl;
  if(CrystalGuidesurface->GetVolume2() == guide_phys)
    G4cout << "Light guide is volume 2" << G4endl;

// Surface 2:

// Entrance and side surfaces of the LaBr3:Ce crystal +
// side surfaces of the optical window:

  G4double sigma_alpha_2 = 0.6;

//-----Scintillator crystal ground and wrapped in Teflon on the entry side:

  G4OpticalSurface* OpCrystalTeflonSurface = new
      G4OpticalSurface("crystalSurface1");
  OpCrystalTeflonSurface->SetType(dielectric_dielectric);
  OpCrystalTeflonSurface->SetModel(unified);
  OpCrystalTeflonSurface->SetFinish(groundbackpainted);
  OpCrystalTeflonSurface->SetSigmaAlpha(sigma_alpha_2);

  const G4int NUM = 2;

  G4double pp[NUM] = {2.0*eV, 4.0*eV};
  //Refractory index of the thin layer (=air) between the crystal and the
      Teflon
  //for energies at both ends of scintillation spectrum
  G4double air_rindex[NUM] = {1.0,1.0};
  //The three options for photon reflections at the surfaces (Thesis, Figure
      4.1):
  G4double specularlobe[NUM] = {0.0,0.0};
  G4double specularspike[NUM] = {0.0,0.0};
  G4double backscatter[NUM] = {0.0,0.0};
  //From the 3 above: diffuselobe = {1.0,1.0} - this should be Lambertian
      refl.

  // Teflon reflectivity from:
  // M. Janecek, Reflectivity Spectra for Commonly Used Reflectors,
  // IEEE Transactions on Nuclear Science 59 (2012) 490-497.
```

```
  G4double teflon_reflectivity[NUM] = {0.97,0.97};
  G4double null_efficiency[NUM] = {0.,0.};

  G4MaterialPropertiesTable* s1MPT = new G4MaterialPropertiesTable();

  s1MPT->AddProperty("RINDEX", pp,air_rindex, NUM);
  s1MPT->AddProperty("SPECULARLOBECONSTANT", pp, specularlobe, NUM);
  s1MPT->AddProperty("SPECULARSPIKECONSTANT", pp, specularspike, NUM);
  s1MPT->AddProperty("BACKSCATTERCONSTANT", pp, backscatter, NUM);
  s1MPT->AddProperty("REFLECTIVITY", pp,teflon_reflectivity, NUM);
  s1MPT->AddProperty("EFFICIENCY", pp,null_efficiency, NUM);

  OpCrystalTeflonSurface->SetMaterialPropertiesTable(s1MPT);

  G4LogicalBorderSurface* crystalTeflonSurface =
    new G4LogicalBorderSurface("crystalSurface1",scintillator_phys,teflon_phys
        ,
    OpCrystalTeflonSurface);

  if(crystalTeflonSurface->GetVolume1() == scintillator_phys)
    G4cout << "Physical scintillator is volume 1" << G4endl;
  if(crystalTeflonSurface->GetVolume2() == teflon_phys)
    G4cout << "Physical teflon is volume 2" << G4endl;

// Scintillator crystal ground and wrapped in Teflon on all sides
// Note that Teflon is not "physically" introduced in the simulation for the
    side surfaces

  G4LogicalBorderSurface* crystalSideSurface =
    new G4LogicalBorderSurface("crystalSurface2",scintillator_phys,
        experimentalHall_phys,
    OpCrystalTeflonSurface);

  if(crystalSideSurface->GetVolume1() == scintillator_phys)
    G4cout << "Physical scintillator is volume 1" << G4endl;
  if(crystalSideSurface->GetVolume2() == experimentalHall_phys)
    G4cout << "Physical World is volume 2" << G4endl;

//------------  Optical window border sides:

  G4OpticalSurface* OpGuideBorderSurface = new G4OpticalSurface("");
  OpGuideBorderSurface->SetType(dielectric_dielectric);
  OpGuideBorderSurface->SetModel(unified);
  OpGuideBorderSurface->SetFinish(groundbackpainted);
  OpGuideBorderSurface->SetSigmaAlpha(sigma_alpha_2);

// Optical window is surrounded by a hermetic seal of unknown
// composition, which we also define as Teflon in the simulation,
//  but with 70% reflectivity (see also: Ulyanov et al., 2013, arXiv:
    1302.5786)

  G4double guide_refl[NUM] = {0.7,0.7};

  G4MaterialPropertiesTable* t1guide = new G4MaterialPropertiesTable();

  t1guide->AddProperty("RINDEX", pp,air_rindex, NUM);
  t1guide->AddProperty("SPECULARLOBECONSTANT", pp, specularlobe, NUM);
  t1guide->AddProperty("SPECULARSPIKECONSTANT", pp, specularspike, NUM);
  t1guide->AddProperty("BACKSCATTERCONSTANT", pp, backscatter, NUM);
  t1guide->AddProperty("REFLECTIVITY", pp,guide_refl, NUM);
```

```
  t1guide->AddProperty("EFFICIENCY", pp,null_efficiency, NUM);

  OpGuideBorderSurface->SetMaterialPropertiesTable(t1guide);

   G4LogicalBorderSurface* GuideWorldSurface =
    new G4LogicalBorderSurface("guideExteriorSurface",guide_phys,
        experimentalHall_phys,
    OpGuideBorderSurface);

  if(GuideWorldSurface->GetVolume1() == guide_phys)
    G4cout << "Physical Guide is volume 1" << G4endl;
  if(GuideWorldSurface->GetVolume2() == experimentalHall_phys)
    G4cout << "Physical Experimental Hall is volume 2" << G4endl;


// Surface 3:

//--------- Optical window / PMT glass volume interface:

  G4OpticalSurface *OpGuidePMT  = new G4OpticalSurface("GuidePMTsurface");
  OpGuidePMT->SetType(dielectric_dielectric);
  OpGuidePMT->SetModel(unified);
  OpGuidePMT->SetFinish(polished);

  // Reflectivity consistent with expected light transmission
  // of the optical adhesive used by the manufacturer
  //(Saint-Gobain Crystals, private communication)
  G4double PMT_reflectivity[NUM] = {0.97,0.97};

  G4MaterialPropertiesTable* sPMT = new G4MaterialPropertiesTable();
  sPMT->AddProperty("REFLECTIVITY", pp,PMT_reflectivity, NUM);

  OpGuidePMT->SetMaterialPropertiesTable(sPMT);

  G4LogicalBorderSurface* guidePMTsurface =
    new G4LogicalBorderSurface("",guide_phys,PMT_phys,
    OpGuidePMT);

  if(guidePMTsurface->GetVolume1() == guide_phys)
    G4cout << "Light guide is volume 1" << G4endl;
  if(guidePMTsurface->GetVolume2() == PMT_phys)
    G4cout << "PMT glass is volume 2" << G4endl;

// Surface 4:

//------- Surface between PMT glass volume and World (experimental hall):

// Added to kill the photons which miss the photocatode:

  G4OpticalSurface *OpPMTWorld  = new G4OpticalSurface("PMTWorldsurface");
  OpPMTWorld->SetType(dielectric_dielectric);
  OpPMTWorld->SetModel(unified);
  OpPMTWorld->SetFinish(polished);

  G4double PMT1_reflectivity[NUM] = {0.,0.};

  G4MaterialPropertiesTable* sPMT1 = new G4MaterialPropertiesTable();
  sPMT1->AddProperty("REFLECTIVITY", pp,PMT1_reflectivity, NUM);

  OpPMTWorld->SetMaterialPropertiesTable(sPMT1);
```

```
  G4LogicalBorderSurface* PMTWorldSurface =
    new G4LogicalBorderSurface("lightPMTSurface",PMT_phys,
        experimentalHall_phys,
    OpPMTWorld);

  if(PMTWorldSurface->GetVolume1() == PMT_phys)
    G4cout << "Physical PMT is volume 1" << G4endl;
  if(PMTWorldSurface->GetVolume2() == experimentalHall_phys)
    G4cout << "Physical Experimental Hall is volume 2" << G4endl;


//------------ Photocathode properties:

// Photocathode properties, complex index of refraction, from:
// Motta & Schönert 2005, NIM Phys. Res. A539, 217, Table 3

  G4OpticalSurface* PhotocathodeOpSurface = new
      G4OpticalSurface("photocathodeSurface");
  PhotocathodeOpSurface->SetType(dielectric_metal);
  PhotocathodeOpSurface->SetModel(glisur);
  PhotocathodeOpSurface->SetFinish(polished);

  G4double photocath_efficiency[NUM]={0.46,0.46}; //Enables 'detection' of
      photons
  G4double photocath_ReR[NUM]={1.92,1.92}; // Best fit refractive indices at
      380 nm
  G4double photocath_ImR[NUM]={1.69,1.69};

  G4MaterialPropertiesTable* s3MPT = new G4MaterialPropertiesTable();
  s3MPT->AddProperty("EFFICIENCY",pp,photocath_efficiency,NUM);
  s3MPT->AddProperty("REALRINDEX",pp,photocath_ReR,NUM);
  s3MPT->AddProperty("IMAGINARYRINDEX",pp,photocath_ImR,NUM);

  PhotocathodeOpSurface->SetMaterialPropertiesTable(s3MPT);

  new G4LogicalSkinSurface("photocathodeSurface",photo_log,
      PhotocathodeOpSurface);

//--------- Visualization attributes -------------------------------

  G4VisAttributes* BoxVisAtt= new G4VisAttributes(G4Colour(0.0,0.0,0.0));
  experimentalHall_log  ->SetVisAttributes(BoxVisAtt);

  G4VisAttributes* ScintillatorVisAtt = new G4VisAttributes(G4Colour(0.0,0.0,
      1.0));
  scintillator_log->SetVisAttributes(ScintillatorVisAtt);

  G4VisAttributes* ParVisAtt = new G4VisAttributes(G4Colour(1.0,1.0,1.0));
  par_log->SetVisAttributes(ParVisAtt);

  G4VisAttributes* IsolVisAtt = new G4VisAttributes(G4Colour(1.0,0.0,1.0));
  isolator_log->SetVisAttributes(IsolVisAtt);

  G4VisAttributes* CollimatorVisAtt = new G4VisAttributes(G4Colour(1.1,0.1,0.0
      ));
  collimator_log->SetVisAttributes(CollimatorVisAtt);

  G4VisAttributes* teflonVisAtt = new G4VisAttributes(G4Colour(1.0,0.0,1.0));
  teflon_log->SetVisAttributes(teflonVisAtt);
```

```
  G4VisAttributes* sourceVisAtt = new G4VisAttributes(G4Colour(0.5,0.5,0.5));
  sourceBox_log->SetVisAttributes(sourceVisAtt);

  G4VisAttributes* guideVisAtt = new G4VisAttributes(G4Colour(0.0,1.0,0.0));
  guide_log->SetVisAttributes(guideVisAtt);

  G4VisAttributes* PMTVisAtt = new G4VisAttributes(G4Colour(0.0,1.0,1.0));
  PMT_log->SetVisAttributes(PMTVisAtt);

  G4VisAttributes* CollimatoVisAtt = new G4VisAttributes(G4Colour(1.1,0.1,0.0)
      );
  photo_log->SetVisAttributes(CollimatoVisAtt);

  G4VisAttributes* photoVisAtt = new G4VisAttributes(G4Colour(1.0,1.0,0.0));
  dyno_log->SetVisAttributes(photoVisAtt);

//--------- example of User Limits -------------------------------

  // below is an example of how to set tracking constraints in a given
  // logical volume(see also in N02PhysicsList how to setup the processes
  // G4StepLimiter or G4UserSpecialCuts).

  // Sets a max Step length in the tracker region, with G4StepLimiter
  //
  G4double maxStep = 1.*cm;
  stepLimit = new G4UserLimits(maxStep);
  scintillator_log->SetUserLimits(stepLimit);

  // Set additional contraints on the track, with G4UserSpecialCuts
  //
  // G4double maxLength = 2*fTrackerLength, maxTime = 0.1*ns, minEkin =
      10*MeV;
  // logicTracker->SetUserLimits(new G4UserLimits(maxStep,maxLength,maxTime,
  //                                              minEkin));


  return experimentalHall_phys;
}
```

Synthèse de la thèse en français

Le principal objectif de la thèse est de créer et de tester un nouveau module de détection de photons de haute énergie destiné à l'imagerie gamma, puis d'utiliser ce module au sein d'un prototype opérationnel de télescope Compton de nouvelle génération. Ce travail de recherche et développement (R&D) vise à préparer une nouvelle mission spatiale d'astronomie gamma dans le domaine d'énergie du MeV, qui a pour but la détection et l'étude de l'origine du rayonnement gamma cosmique d'énergie comprise entre 0,1 et 10 mégaélectronvolt (MeV). Le prototype de détecteur étudié dans cette thèse a vocation à devenir une brique de détection élémentaire d'un futur satellite d'astronomie gamma.

Les principaux objectifs scientifiques de l'astronomie au MeV, ainsi que les observatoires spatiaux existants sont présentés dans le Chapitre 1. Nous donnons tout d'abord un panorama du développement de l'astronomie gamma au cours des 20^e et 21^e siècles, en passant en revue les différents télescopes utilisés dans ce domaine. Nous décrivons en particulier la mission *Compton Gamma-Ray Observatory* (CGRO) de la NASA, mise sur orbite en 1991, celle de l'Agence Spatiale Européenne (ESA) *INTEGRAL* (INTErnational Gamma-Ray Astrophysics Laboratory), lancée en 2002 et toujours en opération, ainsi que la mission *Fermi* de la NASA, en observation depuis 2008. Nous présentons les instruments scientifiques à bord de ces missions, leurs performances, notamment en terme de sensibilité de détection d'un flux de rayons gamma, ainsi que les principaux résultats astrophysiques qu'ils ont permis d'obtenir. Nous mettons ainsi en lumière le relatif retard de l'astronomie gamma des moyennes énergies (0,1 – 100 MeV) par rapport au développement au cours des dernières décennies de l'astronomie X (0,1 – 100 keV) et celle des rayons gamma des hautes énergies (100 MeV à quelques dizaines de GeV). Dans ce contexte, la principale motivation de ce travail de thèse est d'augmenter les performances des futurs télescopes gamma du MeV, pour atteindre un niveau de sensibilité environ 50 à 100 fois plus élevé que celui de l'instrument de référence à l'heure actuelle : le télescope COMPTEL de la mission CGRO. Nous énumérons alors les quatre problèmes spécifiques à la conception d'un télescope spatial opérant au MeV :

1. Les rayons gamma sont très difficiles à réfléchir, parce que leurs longueurs d'onde sont beaucoup plus petites que la distance interatomique typique. Par conséquent, les miroirs de focalisation pour les rayons gamma ont des performances limitées et nécessitent de grandes longueurs focales, de sorte qu'ils sont difficiles à utiliser dans l'espace.

2. Le fond instrumental dans la bande des rayons gamma du MeV est très élevé, du fait de l'émission de raies gamma nucléaires produites par irradiation et activation des matériaux actifs et passifs des instruments dans l'espace.

3. Dans la gamme du MeV, le processus dominant des interactions de photons avec la matière est la diffusion Compton, ce qui provoque des difficultés dans la reconstruction des événements détectés. La reconnaissance des événements à absorption photoélectrique ou à production de paires est généralement plus aisée.

4. La probabilité d'interaction de photons avec la matière atteint un minimum à environ 1 MeV, ce qui diminue en conséquence la probabilité de détection.

Nous donnons ensuite un aperçu des multiples sujets scientifiques qui pourraient bénéficier de l'exploitation d'un nouvel instrument spatial dans la gamme d'énergie du MeV. Ces questions scientifiques concernent, par exemple, (i) l'origine, la propagation et l'interaction des rayons cosmiques, (ii) la nucléosynthèse dans les novae et les supernovae, (iii) le rayonnement des pulsars à haute énergie, (iv) la nature des blazars, (v) les sursauts gamma, (vi) les éruptions solaires, et (vii) les flashes terrestres de rayons gamma.

Nous décrivons également dans cette partie, le principe de l'imagerie Compton, en soulignant l'intérêt d'une conception innovante de télescope Compton de nouvelle génération. Nous concluons ce chapitre en donnant un aperçu du travail accompli ces dernières années, par notre équipe de recherche au Centre de Sciences Nucléaires et de Sciences de la Matière (CSNSM) d'Orsay en particulier, et par la communauté des astronomes gamma en général, pour faire progresser à la fois l'instrumentation gamma et les propositions de nouvelles missions soumises aux agences spatiales. Ce tour d'horizon se termine par une brève présentation de la proposition ASTROGAM, qui a été soumise à l'Agence Spatiale Européenne (ESA) en 2015 en réponse à l'appel à projet de l'ESA pour la quatrième mission de classe moyenne du programme scientifique «Cosmic Vision». Le télescope gamma de la proposition ASTROGAM associe deux dispositifs de spectro-imagerie étudiés à Orsay : un trajectographe constitué de couches minces de détecteurs en silicium double face à micropistes (DSSSD) et un calorimètre composé d'une mosaïque de cristaux scintillants inorganiques.

Dans le Chapitre 2, nous présentons le prototype de télescope Compton de nouvelle génération développé à Orsay pour préparer un futur télescope spatial. Ce banc de test associe actuellement un détecteur silicium DSSSD de 32+32 pistes monté sur sa carte électronique de lecture, qui est développé à l'Institut de Physique Nucléaire d'Orsay (IPNO), et un détecteur à scintillation constitué d'un cristal de bromure de lanthane dopé au cérium ($LaBr_3$:Ce) couplé à un photomultiplicateur multi-anodes (MAPMT) 64 voies, réalisé par notre groupe au CSNSM. En 2016, un nouveau détecteur silicium développé au laboratoire AstroParticule et Cosmologie (APC) du campus Paris Rive Gauche, en liaison avec l'Institut de recherche sur les lois fondamentales de l'Univers (Irfu) du CEA-Saclay, sera intégré au banc de test. L'électronique de lecture du scintillateur repose sur l'ASIC (Application-Specific Integrated Circuit) MAROC (MultiAnode Readout Chip), qui a été initialement développé au Laboratoire de l'Accélérateur Linéaire (LAL) d'Orsay pour le luminomètre du détecteur ATLAS installé auprès de l'accelérateur LHC (CERN, Genève). La lecture du DSSSD de l'IPNO (le modèle BB7 version 2 de Micron Semiconductor Ltd) utilise la puce VA32TA7 de l'entreprise Ideas, qui intègre 32 voies complètes d'électronique de traitement de signaux détecteurs. Dans le cadre de ce projet, l'IPNO a conçu une carte électronique embarquant un détecteur BB7, deux ASICs VA32TA7 (un par face du détecteur), les électroniques de numérisation des signaux de sortie des ASICs, ainsi qu'une interface vers une carte de développement FPGA (la carte d'évaluation ML605 de Xilinx). La synchronisation des différents sous-systèmes est assurée par la distribution d'un signal d'horloge d'environ 1 Hz. Les données numérisées sont ensuite transmises à un PC via une interface PCI Express et traitées par le système d'acquisition NARVAL pour l'identification des événements de coïncidences caractéristiques d'une diffusion Compton. Certaines mesures de test du prototype sont réalisées dans une enceinte climatique, à des températures variant entre -5° et 20° C, afin d'étudier le télescope dans de meilleures conditions de fonctionnement des DSSSDs (diminution du courant de fuite à basse température), plus proches des conditions attendues dans l'espace.

Dans la seconde partie de ce chapitre, nous présentons la suite de logiciels MEGAlib spé-

cialement conçue pour simuler les performances de télescopes gamma de nouvelle génération. Nous exposons alors le modèle numérique utilisé pour simuler les performances de notre prototype de télescope Compton. Les propriétés des détecteurs – résolution spectrale, résolution en position, seuil de détection – sont entrées dans la simulation numérique à partir des résultats des mesures de caractérisation. En étudions en particulier dans cette partie l'efficacité de détection, la résolution en énergie et la précision de positionnement des sources gamma avec le prototype de télescope, en fonction de la distance entre les différents détecteurs. Nous montrons que la résolution angulaire s'améliore quand la distance augmente, mais au prix d'une plus mauvaise résolution spectrale et d'une moins bonne efficacité de détection. Un bon compromis pourrait être obtenu avec une distance d'environ 10 cm entre le DSSSD et le scintillateur.

Dans le Chapitre 3, nous nous concentrons sur le principal travail expérimental réalisé par notre groupe au CSNSM. Nous avons assemblé et testé deux modules de détection, l'un avec un cristal de $LaBr_3$:Ce et l'autre avec un cristal de bromure de cérium ($CeBr_3$). Dans les deux modules, la lumière de scintillation des cristaux est collectée par des photomultiplicateurs multi-anodes 64 voies sensibles à la position de l'interaction gamma. L'objectif principal de nos travaux de R&D est d'optimiser la résolution en énergie de ces détecteurs en même temps que la résolution en positionnement du premier impact d'un rayon gamma incident dans le cristal scintillant. Les deux informations sont essentielles pour la reconstruction d'une image gamma avec le prototype de télescope à partir de l'effet Compton. Outre la localisation du dépôt d'énergie dans le plan X–Y de la photocathode, la distribution spatiale des signaux de scintillation sur les anodes peut fournir une mesure de la profondeur Z de l'interaction dans le cristal. Nous avons développé au CSNSM un banc de test pour étudier expérimentalement les deux modules avec une électronique de lecture et un système d'acquisition de données dédiés. L'électronique frontale des détecteurs utilise la carte de test de l'ASIC MAROC initialement conçue au LAL, mais qui a été largement modifiée dans le cadre de ce projet et complétée par une extension assurant le transfert des données numérisées vers une carte FPGA concentratrice. Le système d'acquisition de données auto-déclenchées ainsi obtenu est piloté via une interface graphique dotée d'une configuration dynamique. Un étalonnage précis du système électronique, canal par canal, a été effectué avant les mesures. Le banc de test comprend également une table X–Y permettant de déplacer finement le détecteur devant un faisceau de rayons gamma obtenu avec un collimateur de sources radioactives gamma constitué de plomb et de tantale. Nous avons utilisé les sources radioactives suivantes : ^{241}Am (430 kBq), ^{133}Ba (40 kBq), ^{137}Cs (4.5 kBq et 3,8 MBq) et ^{60}Co (34,8 kBq). De nombreuses mesures de position ont été effectuées avec ce banc de test, afin d'étudier la précision de localisation du site d'interaction des rayons gamma dans les scintillateurs, en fonction de la position du faisceau incident et de son énergie.

Dans le Chapitre 4, nous présentons une simulation numérique détaillée de l'expérience visant à reproduire au mieux les mesures de distribution spatiale de la lumière de scintillation au niveau de la photocathode. Ce travail, réalisé avec le logiciel Geant4, a nécessité une modélisation fine des propriétés optiques des différents constituants des détecteurs (cristal scintillant, enveloppe réfléchissante, fenêtre optique, photomultiplicateur etc..), ainsi que de la propagation des photons ultraviolets depuis leur site d'émission dans le cristal jusqu'à la photocathode. Nous avons inclus dans cette simulation l'ensemble des propriétés optiques des scintillateurs données dans la littérature : spectres d'émission et de ré-absorption, longueur caractéristique d'auto-absorption de la lumière ultraviolette etc.. Nous présentons dans cette partie une série de tests visant à optimiser les paramètres du modèle dans son ensemble. Ces travaux nous ont permis de sélectionner deux configurations reproduisant correctement les mesures effectuées sur le banc de test avec les détecteurs au $LaBr_3$:Ce et au $CeBr_3$. Les constituants du détecteur au $LaBr_3$:Ce et leurs propriétés optiques déterminées grâce à la simulation sont données en annexe

du manuscrit. La simulation Geant4 nous a permis de comprendre dans le détail le fonctionnement de ces nouveaux modules de détection et d'envisager des moyens d'améliorer encore leurs performances. En outre, les données simulées sont utilisées pour entraîner un réseau de neurones artificiels (RNA) dédié à la reconstruction de la position 3D du premier impact des rayons gamma dans les scintillateurs.

Le logiciel RNA utilisé, JETNET 3.0, est présenté dans le Chapitre 5. Ici, nous donnons tout d'abord une brève introduction sur la théorie des réseaux de neurones artificiels, en présentant le concept de base, les termes principaux du formalisme mathématique et les avantages pratiques de l'utilisation d'un tel algorithme. Ensuite, nous détaillons la configuration de l'algorithme utilisé et l'optimisation des paramètres informatiques pour une application en imagerie 3D. Nous avons étudié de manière détaillée les variables d'entrée du réseau de neurones, le nombre de couches du réseau, le nombre de nœuds (ou neurones) par couche, ainsi que la durée nécessaire du processus d'apprentissage. Le réseau de neurones finalement retenu est un perceptron multicouche comprenant deux couches cachées de dix nœuds chacune, avec rétro-propagation des erreurs. Il prend en entrée les 64 charges mesurées avec le photomultiplicateur multi-anodes et donne en sortie les positions X, Y et Z. Enfin, nous présentons dans cette partie les performances idéales de cette méthode pour l'imagerie gamma 3D, en appliquant l'algorithme de reconstruction à des données simulées avec le logiciel Geant4.

Dans le dernier chapitre de la thèse, nous présentons tous les résultats expérimentaux obtenus avec les deux modules à scintillation, en commençant par exposer une méthode relativement simple de reconstruction de position gamma basée sur la logique dite d'Anger (en référence au concept de gamma caméra d'Anger). Cette méthode repose sur la mesure du centre de gravité de la distribution de charges, en utilisant un nombre fixé de pixels présentant une charge maximum, pour estimer les positions X et Y sur le plan de la photocathode. Cette méthode a été développée à titre de comparaison et de vérification des résultats obtenus avec l'algorithme RNA. Nous présentons ensuite les performances de plusieurs RNAs entraînés avec différents jeux de données simulées, en appliquant l'algorithme de reconstruction de position à des données expérimentales enregistrées sur le banc de test. Nous discutons alors de l'erreur quadratique moyenne obtenue sur la position 2D des interactions des rayons gamma dans le plan frontal des détecteurs. Pour estimer au mieux l'erreur sur le positionnement 2D de l'interaction gamma, nous avons développé une nouvelle simulation numérique, de type Monte-Carlo, visant à reproduire au mieux la distribution des positions reconstruites. Cette simulation inclut notamment le bruit de fond propre du détecteur au $LaBr_3$:Ce dû à la radioactivité interne de ce scintillateur.

Finalement, nous donnons dans cette partie l'ensemble des résultats portant sur la réponse spectrale des détecteurs. Nous étudions en particulier la gamme dynamique des détecteurs, pour une tension de polarisation donnée, ainsi que leur résolution en énergie. Nous avons utilisé pour ce travail une douzaine de raies X et gamma, comprise dans une gamme d'énergie entre 22,1 keV – raie Kα de fluorescence de l'argent – et 1332,5 keV – raie produite par la source de cobalt-60. Nous avons par ailleurs montré la bonne stabilité avec le temps du détecteur au $LaBr_3$:Ce, sur une période de près de deux ans. De plus, nous démontrons dans ce travail comment une simple correction dépendante de la position d'interaction des rayons gamma à l'intérieur du détecteur peut améliorer de manière significative la résolution en énergie des scintillateurs.

Les résultats que nous avons obtenus dans cette thèse demontrent clairement l'intérêt du détecteur étudié pour l'astronomie gamma spatiale. Ainsi, notre module en $LaBr_3$:Ce a un seuil de détection d'environ 15 keV, une résolution en énergie de 3,6% à 662 keV et une résolution moyenne en position d'environ 2,6 mm (écart type) sur toute la surface du détecteur. Ce dernier résultat a été obtenu en utilisant un algorithme RNA entraîné avec des données simulées pour

des photons gamma de 356 keV (caractéristiques d'une source de ^{133}Ba). Mais nous avons montré que ce même algorithme fournit également des résultats tout à fait satisfaisant pour des photons de 59,5 keV (source de ^{241}Am) et 662 keV (^{137}Cs). Les résultats obtenus avec le module en $CeBr_3$ sont moins probants du fait du plus faible taux de scintillation de ce cristal, ainsi que d'un défaut structurel de ce détecteur révélé par ce travail ; néanmoins, les résolutions mesurées répondent parfaitement aux exigences d'un futur télescope spatial de type Compton.

Nous concluons le manuscrit par un résumé du travail effectué et une brève présentation de différents projets utilisant le concept d'imagerie gamma 3D développé dans cette thèse. Le projet principal porte sur le développement d'un petit télescope Compton dédié à des mesures de polarisation gamma entre 0,1 et 2 MeV dans des expériences sous ballon stratosphérique. Une autre application envisagée consiste en la réalisation d'une gamma caméra portative ultra sensible pour les prochains chantiers de démantèlement d'installations nucléaires.

List of Figures

1.1 Opacity of the Earth's atmosphere as a function of photon wavelength. 7

1.2 EM shower, cherenkov light, telescopes 8

1.3 H.E.S.S. Telescope Array located in Namibia. It consisted of 4 smaller, 12 meters diameter telescopes, and one central telescope of 28 meters diameter. 9

1.4 $Left$: Artist impression of the CTA site, including 23 m and 12 m telescopes. $Right$: Gamma-ray Cherenkov Telescope (GCT), one of the prototype instruments for the CTA. GCT is a small 4 m diameter telescope, installed at Paris Observatory in Meudon. It is also the first Schwarzschild-Couder telescope to be used in detection of the Cherenkov light. 9

1.5 View of the Compton Gamma Ray Observatory during deployment of the spacecraft. 11

1.6 Artist's view of the INTEGRAL satellite. 12

1.7 Fermi (GLAST) satellite schematic, with noted two main instruments: LAT - with tracker, calorimeter and ACS; and GBM on the opposite side. 13

1.8 Sensitivity achieved in different energy bands of the gamma-ray astronomy by different instruments (from: *Takahashi et al.*, 2012). Here, $\nu F_\nu = S(E) \times E^2$, where E is the photon energy and $S(E)$ the differential sensitivity, i.e. the minimum flux (e.g. in photons cm^{-2} s^{-1} MeV^{-1}) that can be detected at a given confidence level (usually 3σ or 5σ) after a given time of observation of the astrophysical source (see: *Takahashi et al.*, 2012). The lines in blue represent past or currently operating instruments, while instruments planned for the near future are in black. The dashed red line shows the sensitivity reference expressed by mCrab, an equivalent to one thousandth part of intensity detected from the Crab nebula (including the Crab pulsar within it). 14

1.9 Cross-sections for different interactions of gamma-rays with matter, calculated for Si, depending on the energy of an incident gamma-ray. 17

1.10 Simple representation of a Compton effect. The incident gamma-ray (in red) hits an electron at rest and scatters with lower energy (in blue). The noted angle Θ is the angle between the original and scattered direction of the gamma-ray, and is called Compton scattering angle. A part of energy is also given to the electron, called Compton electron, which scatters in a different direction, defined by the electron scattering angle. 18

1.11 Representation of an electron-positron ($e^- e^+$) pair production in the electromagnetic field of a nucleus of charge Z. Noted with Z' is the nucleus of the same charge but with change in momentum due to occurred interaction. 18

1.12 $a)$ Principle of a classical Compton telescope made of two detectors D1 and D2. $b)$ An advanced Compton telescope comprising a tracker allowing the tracking of the Compton electron and a 3-D position sensitive calorimeter. Measuring the direction of the recoil electron can constrain the gamma-ray event to an arc of the Compton annulus. 19

1.13 $Left$: A Compton image gained from a classical Compton telescope. $Middle$: An image obtained with a Compton telescope capable of electron tracking. $Right$: Imaging with electron tracking for the case of high-energy events (from: *Zoglauer*, 2006). 21

1.14 The ARM ($\Delta\varphi$) is the measure of the width of the Compton scatter cone or an arc. The $\Delta\varphi_{ARM}$ value can be positive, meaning the real point of origin lays outside the cone and we have an incomplete detection of an recoil electron, or if $\Delta\varphi_{ARM}$ is negative, the point of origin lies inside the cone, and the scattered gamma-ray is incompletely absorbed (*Zoglauer*, 2006). 21

1.15 DUAL in deployed configuration with a detailed view of the focal plane instrument ASCI (All-Sky Compton Imager) made of a compact array of cross-strip germanium detectors. 22

1.16 View of the CAPSiTT payload made of a stack of double-sided silicon strip detectors, on top of the Sentinel 3 platform developed by Thales Alenia Space. . . . 23

1.17 GRIPS configuration in the two satellite option, where the Gamma-Ray Monitor (GRM) is on one satellite, and the X-Ray Monitor (XRM) and the InfraRed Telescope (IRT) on the other. 23

1.18 $Left$: ASTROGAM satellite with deployed solar panels and radiators. $Right$: Zoom-in on the satellite's payload showing the Silicon Tracker, the Calorimeter and the Anti-Coincidence (AC) system. 24

1.19 Same as Figure 1.8, but with the predicted sensitivity of ASTROGAM for an effective exposure of one year of a high Galactic latitude source. The curve for e-ASTROGAM is the goal sensitivity of the larger scale and enhanced instrument that will be proposed to ESA in 2016 in response of the M5 Call. 25

2.1 $Left$: Mechanical drawing of the gamma-ray telescope concept. $Right$: Presentation of the telescope and the collimator for radioactive gamma-ray sources inside the climatic chamber. The telescope is placed in a black box not shown in this diagram. 28

2.2 Photograph of the BB7 DSSSD test bench around PACI preamplifiers. The detector is mounted in the lower left corner of the electronic readout card. A copper cooling circuit provides temperature control of the preamplifiers. 28

2.3 ^{207}Bi energy spectrum obtained with the BB7 DSSSD at IPNO, Orsay. 29

2.4 Computer-aided design of the FEE card of the BB7 detector. 29

2.5 Medium Energy Gamma-ray Astronomy telescope (MEGA) mission; $Left$: scaled working prototype. The tracker in gold casing in the middle is made of 11 layers of 3×3 DSSSDs. The tracker is surrounded with 20 CsI(Tl) detectors placed in separate grey aluminium boxes. $Right$: a simulated geometry model corresponding to the prototype. 31

2.6 Simulated model of the ACT prototype. Separate elements are explained in the text. 32

2.7 Reconstructed spectrum from the simulated data, implementing the prototype geometry with Z_{dist} = 10 cm. All of the counts correspond to detected Compton scattered photons, originating from a radioactive beam of Eγ = 662 keV. The events, which deposited the full energy in the detector are grouped in a noted 662 keV peak, while the uneven distribution to the left is from incompletely detected events. By using the implemented fit tools in MEGAlibg we placed a selection around the full energy peak and performed fitting, obtaining the width (1σ) of a Gaussian fit function. 33

2.8 ARM spectrum obtained in MEGAlib after a selection on the full energy peak in the energy spectrum (Figure 2.7), with $E_\gamma = 662$ keV and Z_{dist} = 10 cm. The performed fit, from which we obtained the ARM(FWHM)=4.8^o value is noted in red, while the data is given in green. 34

2.9 Efficiency study using MEGAlib simulations. We note the full-energy peak efficiency with full lines, and efficiency to detect Compton events with dotted lines, for three different source energies: 122 keV (in blue), 356 keV (in red) and 662 keV (in green). 35

2.10 Compton Imaging performed with MEGAlib from the obtained simulated data with $E_\gamma = 662$ keV and $Z_{\mathrm{dist}} = 10$ cm. The top left image corresponds to the left image on the Fig. 1.13 (Chapter 1). The final outcome is improved over several iterations, where we note the limit of the method reached after the 4th iteration. 36

3.1 Detector test bench at CSNSM Orsay: 1. collimated radioactive source, 2. interchangeable detector module, 3. electronics board, 4. X–Y table, 5. PC. 37

3.2 Schematic representation of main elements within the $LaBr_3$:Ce detector module. From left to right: $LaBr_3$:Ce crystal is coupled to a borosilicate glass optical window which on the other side connected to the 64 channel MAPMT. The elements are placed in an isolated aluminium protective box. 39

3.3 $CeBr_3$ module, with the scintillator crystal wrapped in reflective coating and placed in an air-tight enclosure within the aluminum casing. In front of the crystal is an optical window held by a hermetic seal. The module was later coupled, via the surface visible on the figure, to a MAPMT via optical grease. 40

3.4 The schematic of the electronics test board used to read out the 64 channel MAPMT from the detector module. 40

3.5 Block schematic of the MAROC chip architecture. 41

3.6 Examples of results used for the calibration of four different channels numbered: 04, 33, 46 and 61. *Top panels*: measured $\mathrm{ADC_m}(q)$ data points, presented as red dots, were fitted with three different functions: f_1 (eq. 3.2) in orange, f_2 (eq. 3.3) in green and f_3 (eq. 3.4) in blue. The functions are taken in intervals defined by borders $q(B1) = 80$ pC and $q(B2) = 150$ pC. *Bottom panels*: corresponding fit residuals for each of the three fit functions. 44

3.7 Charge distribution dependency on the radioactive beam position. All four cases are measured with a collimated ^{241}Am source and selecting the full energy 59.5 keV gamma-rays in the analysis. The respective beam positions, relative to the central position of the detector, are: $X_{\mathrm{POS}} = Y_{\mathrm{POS}} = -20$, $+00$, $+05$, and $+20$ mm, for each panel respectively, from the top left to the bottom right. 46

3.8 *Left*: Uncorrected total charge distribution over the 64 channels of the MAPMT. *Right*: After correction for the non-uniformity of the MAPMT anodes. Both panels correspond to the same measurement run, performed with collimated gamma-rays of 662 keV from a ^{137}Cs source. The beam is aimed at the central position of the $LaBr_3$:Ce detector, $X_{\rm POS} = Y_{\rm POS} = 0$ mm. 47

3.9 Two energy spectra, with marked energy peaks, obtained with the $LaBr_3$:Ce detector. *Left*: ^{241}Am radioactive source, in linear scale. *Right*: ^{133}Ba radioactive source, in logarithmic scale. 47

3.10 Result from one photoelectron calibration of the MAPMT. In blue is the measured gain for each of the anode (in total 15 different anodes out of 64), while in red are scaled ($\times$1.3) values from the test sheet provided by Hamamatsu Photonics. 49

4.1 *Right*: representation of a ground surface with micro-facets. The inclination of each micro-facet is defined by the angle α from the normal of the average surface. *Left*: different cases of photon reflection as defined in the UNIFIED model. The *Lambertian* reflection is represented on the figure by the *Diffuse Lobe*. The *Backscatter* reflection is when the reflected photon propagates in the opposite direction from the *Incident light*. 53

4.2 $Left$: Schematic representation of volumes and surfaces within the $LaBr_3$:Ce detector module: $Surface\ 1$, shown in red, is the coupling surface between the $LaBr_3$:Ce crystal and the optical window; $Surface\ 2$, shown in blue, includes the border sides of both the $LaBr_3$:Ce crystal and the optical window. $Right$: Image from Geant4 visualization with simulated elements: 1 – ^{241}Am radioactive source, 2 – radioactive beam, 3 – Cu collimator, 4 – aluminium entrance window modeling the aluminium housing, 5 – $LaBr_3$:Ce scintillator (with produced scintillation light in green), 6 – optical window, 7 – MAPMT volume with photocathode (red) and active detector volume (yellow). Note that, for clarity, we reduced the $LaBr_3$:Ce's light yield from 63 to 0.1 photons per keV, which resulted in detecting only 1 simulated photon. 54

4.3 $Left$: LS and $Contrast$ parameters derived from Geant4 simulations with different combinations of σ_α and with the reflection type from the sides of the crystal and optical guide (Surface 2) set to be 100% $backscatter$. The horizontal lines in the lower panels show the values of $Contrast$ from the experimental measurements, for the two beam positions. Vertical data lines with points, corresponding to simulated data, show the variation depending on different values of SigmaAlpha 2 (the σ_α parameter for the border sides of the crystal and optical window). SigmaAlpha 1 is the σ_α parameter for the interface between the crystal and the optical window. Data points corresponding to beam positions $X_{\rm POS} = Y_{\rm POS} = 0$ and $+15$ mm are given in black and green, respectively. All simulations and measured data are for 59.5-keV γ-rays from the ^{241}Am source. $Right$: Same as on the left panel, but for the reflection type from Surface 2: 100% $specularspike$. . 57

4.4 Same as Figure 4.3, but for the reflection type from Surface 2: 100% $Lambertian$ (*left panel*) and 100% $specularlobe$ (*right panel*). 58

4.5 $Left$: LS and $Contrast$ parameters as a function of SigmaAlpha 2 (the σ_α parameter for the border sides of the crystal and optical window in the Geant4 simulation), for $\mathrm{SigmaAlpha}\ 1 = 10$ (the σ_α parameter for the interface between the crystal and the optical window) and the reflection type from Surface 2 set to be 100% $Lambertian$. The horizontal lines in the lower panel show the measured $Contrast$ for the three beam positions. Simulated data points corresponding to beam positions $X_{\mathrm{POS}} = Y_{\mathrm{POS}} = 0$ mm/+15 mm/+20 mm are given in black,green and blue, respectively. All simulations and data are for 356-keV γ-rays from the ^{133}Ba source. $Right$: LS and $Contrast$ parameters as a function of SigmaAlpha 1, for $\mathrm{SigmaAlpha}\ 2 = 10$ and the reflection type from Surface 2 set to be 100% $specularspike$. 59

4.6 Comparison of (top) measured and (bottom) Geant4 simulated distributions of charges for the $LaBr_3$:Ce detector, and for fully-absorbed 662-keV γ-rays emitted by a collimated ^{137}Cs source pointing at the position from the detector centre X_{POS}=Y_{POS}=+15 mm. The bottom left panel shows the simulated distribution for the $specularspike$ case of "Simulation 1", while the bottom right panel is for the $Lambertian$ case of "Simulation 2" (see text). The measured total charge is Q_{exp}=2174 pC, while the simulated ones are Q_{sim}=2190 and 1814 pC for Simulations 1 and 2, respectively (see Table 1). 61

4.7 Comparison of (top) measured and (bottom) Geant4 simulated distributions of charges for the $CeBr_3$ detector, and for fully-absorbed 356-keV γ-rays emitted by a collimated ^{133}Ba source pointing at the detector centre (X_{POS}=Y_{POS}=0 mm). The bottom left panel shows the simulated distribution for the $specularspike$ case of "Simulation 1", while the bottom right panel is for the $Lambertian$ case of "Simulation 2" (see text). The measured total charge is Q_{exp}=881 pC, while the simulated ones are Q_{sim}=941 and 860 pC for Simulations 1 and 2, respectively (see Table 2). 62

5.1 A representation of an artificial neuron - a main computational unit of the ANN. The $x_{1\cdots n}$ are the input values with corresponding attributed weights $w_{1j\cdots nj}$, Σ is an integration function reducing the number of inputs to a single net input value, g is the activation function of the neuron, with θ_j being the threshold value attributed to g and y_j are the corresponding output features. 64

5.2 A schematic representation of a multilayer perceptron structure available with JETNET 3.0. We can see an ANN with one input layer made out of x_k nodes, one hidden layer containing h_j nodes and one output layer with y_i nodes. The nodes are connected through weights w_{jk} and w_{ij}, where i,j and k denote the index of nodes in each layer, respectively. 65

5.3 RMS deviations of the reconstructed 3D position of gamma-ray hits from the training and validation processes of the ANN as a function of the number of iterations in the training process. The three panels correspond to three position coordinates of the first γ-ray hit in the $LaBr_3$:Ce crystal. The ANN training and validation processes are done with 6×10^4 and 3×10^4 simulated events, respectively. The Geant4 simulation is performed for incident γ-rays of energy $E_\gamma = 356$ keV using the configuration of "Simulation 2" (see text). 69

5.4 Standard deviations of X_1 and Y_1 from the ANN validation process, as a function of the number of training events. The ANN training configuration is as for Fig. 5.3. The number of iterations in the ANN training process is 1000. 70

5.5 Distribution of the RMS error of the reconstructed X–Y position, averaged for both coordinates X and Y, as a function of position on the front plane of the crystal. The values are obtained from the ANN readout after the training and validation processes. The ANN training configuration is the same as for Figures 5.3 and 5.4. 70

5.6 Study of the ANN performance on the reconstruction of the depth-of-interaction (DOI) of the first interaction position of the incident gamma rays within the $LaBr_3$:Ce detector. Full black lines are direct DOI output from the Geant4 simulations, while in red we give reconstructed DOI values from the ANN. $Left$: ANN trained with E_γ = 59.5 keV gamma rays; $Right$: same study for the case of E_γ = 356.5 keV. 71

6.1 First reconstructed position obtained by a center-of-gravity method as a function of the experimental irradiation position (open symbols). Different experimental points are obtained for different number of pixels utilized for the truncated charge distributions. *Left:* $LaBr_3$:Ce; *Right:* $CeBr_3$ module. 74

6.2 Distributions of reconstructed positions for each full-energy event of the measurement with the collimated ^{241}Am source at $X_{\rm POS} = Y_{\rm POS} = +5$ mm from the $LaBr_3$:Ce detector middle position, using the 25 pixels with the highest charge value. Blue histogram: first reconstruction step of the center-of-gravity method; green histogram: second reconstruction step after interpolation between the mean values obtained in the first step. The solid curves show Gaussian fits to the data yielding centroid values of +3.76 and +5.60 mm, and FWHM of 5.29 and 7.55 mm, for the blue and green histograms, respectively. 75

6.3 Position resolution obtained by the center-of-gravity method – 1σ standard deviation about the experimental position – as a function of projected distance from the center along a diagonal in the front plane of the detector. Each line corresponds to a given number of pixels, as indicated in the panels. The values given in the panels correspond to the mean position resolutions. *Left:* $LaBr_3$:Ce; *Right:* $CeBr_3$ module. 75

6.4 Reconstructed X-Y position of the first γ-ray hit in the $LaBr_3$:Ce crystal using the ANN method. From left to right, the data are for fully-absorbed 59.5-keV γ-rays (^{241}Am source), $\sim$ 360-keV γ-rays (from the lines at 356 and 384 keV from the ^{133}Ba source), and 662-keV γ-rays (^{137}Cs source). The black crosses note the γ-ray beam positions during the measurements; they change in steps of ± 5 mm for $X_{\rm POS}$ and $Y_{\rm POS}$ starting from the central position ($X_{\rm POS} = Y_{\rm POS} = 0$ mm). The ANN was trained using 6×10^4 simulated events for incident γ-rays of energy $E_\gamma = 356$ keV, using the configuration of "Simulation 2" (see Chapter 4). 76

6.5 Further examples of ANN performance for the reconstructed X-Y position of the first γ-ray hit in the $LaBr_3$:Ce crystal. Left panel: ^{241}Am data reconstructed using an ANN trained with simulated events from 59.5 keV γ rays and with the configuration of "Simulation 2" (see Sect. 3.4). Middle panel: ^{133}Ba data reconstructed with an ANN trained with simulated events from 356 keV γ rays and with the configuration of "Simulation 1". Right panel: ^{133}Ba data reconstructed with an ANN trained with two sets of simulated events, both produced with $E_\gamma = 356$ keV and "Simulation 2", but with two different values of SigmaAlpha 2 depending on the X-Y position (see text). 77

6.6 ANN performance for the reconstructed X-Y position of the first γ-ray hit in the $CeBr_3$ detector. The data are for fully-absorbed γ rays from the ^{133}Ba source. The ANN is trained with simulated events from 356 keV γ-rays, using the configuration of "Simulation 2" (see Chapter 4). 78

6.7 Measured (*left*) and simulated (*right*) distributions of reconstructed X-Y positions in the $LaBr_3$:Ce detector, for the ^{133}Ba γ-ray beam at the position $X_{\rm POS} = Y_{\rm POS} = +10$ mm. The position reconstruction uses the ANN trained with Geant4 simulated events from 356 keV γ-ray with the configuration of "Simulation 2". The two distributions were quantitatively compared (see text) by calculating the RMS error of the reconstructed beam position, using only the data within the circle of radius $d_{\rm max}$. For illustrative purpose, we used for this Figure the same number of Monte-Carlo simulated events as measured: 1800. The simulated data were drawn randomly using the best-fit parameters $\sigma = 2.2$ mm and $f_{\rm bg} = 14.5\%$, σ being the standard deviation of the Gaussian function representing the γ-ray emission from the collimated source and $f_{\rm bg}$ the relative intensity of the background emission. 78

6.8 Standard deviations of truncated 2D distributions of the reconstructed γ-ray hit position around the experimental position of irradiation, as a function of the maximum distance of the reconstructed position to the γ-ray beam position. The number of events used in the calculations of the 1σ values thus increases with $d_{\rm max}$. The open symbols are standard deviations for $X_{\rm POS}$ (in blue) and $Y_{\rm POS}$ (in red) calculated with real data, whose positions were reconstructed with the ANN method (see text). The black curves are simulated fitting curves depending on two free parameters: the 1σ width of the Gaussian representing the γ-ray emission from the collimated source, and the relative intensity of the uniform background emission, $f_{\rm bg}$. We show two cases (top and bottom panels) for two different measurements as noted on panels. For each case we give three different fit functions, calculated with different parameters as noted on bottom right of the panels. Functions 1 and 3 are clearly over- and under-producing the data, respectively, while function 2 is the best-fit result. 79

6.9 Position resolution obtained by the ANN method – 1σ standard deviation about the experimental position – as a function of projected distance from the center along a diagonal in the front plane of the detector. Solid lines: position resolution on data corresponding to measurements at three different energies (noted on the panel), where the γ-ray hit position is reconstructed with a matrix of weights from an ANN trained with simulated $E_\gamma = 356$ keV γ-rays and the Geant4 configuration of "Simulation 2". The red dashed line shows the error in the position reconstruction using simulated $E_\gamma = 59.5$ keV γ-rays (together with "Simulation 2"). The green dotted line gives the position resolution for the $CeBr_3$ detector; it is for ^{133}Ba data reconstructed with an ANN trained with simulated events from 356 keV γ rays and with the Geant4 configuration of "Simulation 2". 80

6.10 2D distribution of the RMS error of the first gamma-ray interaction position, averaged for both coordinates X and Y, as a function of position on the front plane of the crystal. $Left$: RMS error distribution from simulated data shown in Fig. 5.5 (Chapter 5); $Right$: RMS error distribution obtained using measured data from ^{133}Ba source as in Figure 6.9, and using the same ANN configuration as for the left panel of the current Figure. 81

6.11 DOI of gamma-rays in the $LaBr_3$:Ce module obtained with the ANN method. The black and red curves were already shown in Figure 5.6: they correspond to DOI values obtained from the Geant4 simulation and to those reconstructed from the ANN method, respectively. The blue curves show the reconstructed DOI using experimental data. $Left$: both experimental and simulated data were obtained with $E_\gamma = 59.5$ keV (^{241}Am radioactive source), and the ANN was trained with simulated gamma rays of the same energy; $Right$: experimental data were obtained with $E_\gamma \sim 360$ keV (from the lines at 356 and 384 keV from the ^{133}Ba source), simulated data with $E_\gamma = 356$ keV and the ANN was also trained with $E_\gamma = 356$ keV gamma rays. In both cases, the ANN training was done using the Geant4 configuration of "Simulation 2" (see text and Chapter 5 for details). 82

6.12 Blue symbols: energy spectrum obtained with the $LaBr_3$:Ce detector from the irradiation of a silver plate with a collimated ^{241}Am source. Red symbols: spectrum measured under the same conditions but without the silver plate. The structure above the K X-ray lines of Ag and Ba is due to 59.54-keV γ rays reaching the detector directly and/or indirectly by coherent and incoherent scattering. The two spectra have been obtained with a high-voltage power supply on the MAPMT of HV $= 1000$ V. 83

6.13 Total charge spectrum recorded with the ^{60}Co source. The measurement is done with a high voltage of HV $= 900$ V. 85

6.14 Experimentally recorded events from uncollimated ^{137}Cs source. The left panel corresponds to an uncorrected charge spectrum, where we select events from the full energy peak at E_γ=661.7 keV by choosing a corresponding window in the charge spectrum (2100–2350 pC). A clear trend is visible: the larger the distance from the center of the detector r [mm] the less charge is collected. The green points on the graph present the average charge collected for all events with the reconstructed position less than $r = 3, 9, 15, 21, 27$ and 33 mm. After fitting the data we are able to find a correction function f_Q from the fit. On the right is the same plot after the correction is applied. The selection window is narrower (2200–2350 pC), which indicates that the full-energy peak is also narrower. The fit now shows a horizontal flat trend, which directly improves the final energy resolution. 86

6.15 Energy resolution measured with the $LaBr_3$:Ce and $CeBr_3$ detectors. The green and blue data points give the performance for $LaBr_3$:Ce measured in 2013 and 2014, respectively. The data in yellow are for the $CeBr_3$ detector. All the experimental data were obtained with a high voltage power supply of the MAPMTs of 1000 V, except for the ^{60}Co data points in pink that show the results obtained with the $LaBr_3$:Ce in 2013 using HV $= 900$ V. The straight lines show best fits to the data between 59.5 and 662 keV with functions proportionnal to $\sqrt{E}$. The resulting values of $\mathrm{fwhm}_{\mathrm{detector}}$ (the best-fit relative resolution at 662 keV) are of 3.6% ($LaBr_3$:Ce in 2013), 3.6% ($LaBr_3$:Ce in 2014) and 5.1% ($CeBr_3$ in 2015), as given on the plot. 87

6.16 A studied model of the ComPol project, a full ACT prototype aimed to be launched in a stratospheric balloon mission to study the emission and polarization of bright X-ray sources such as the Crab nebula. 92

6.17 MEGAlib geometry model of the ComptonCam portable gamma camera projetc. In the front we see DSSSD detectors (yellow) with the corresponding FEE (green). Behind are the scintillation calorimeter modules (purple) with the BEE electronics in the far back (red). 93

List of Tables

2.1 Energy, angular resolution (ARM) and efficiency obtained with MEGAlib simulation runs using the geometry defined on Fig. 2.6. Each of the recorded values listed are explained in the text. We used a gamma-ray source with E = 662 keV. Furthermore, we varied the Z_{dist} parameter, assigning values of 1, 4, 7 and 10 cm. 33

4.1 Comparison between experimental data and two Geant4 simulations (see Sect. 3.4) for the $LaBr_3$:Ce detector. The selected γ-ray energies are: 59.5 keV (^{241}Am), 356 keV (^{133}Ba) and 662 keV (^{137}Cs). The γ-ray beam position is given as the distances X_{POS} and Y_{POS} from the center of the detector. The simulated contrast values in bold are those differing by more than 25% from the experimental ones. 60

4.2 Same as Table 1, but for the $CeBr_3$ detector. 60

6.1 Studied X-ray and γ-ray lines with FWHM for both detector modules. In the fit of the ^{133}Ba spectrum, equal Gaussian widths were imposed for the lines at 276.4 and 302.9 keV, and for those at 356.0 and 383.8 keV. All data were acquired with a high-voltage power supply on the MAPMT of 1000 V. The results of a measurement with the $LaBr_3$:Ce detector and $\mathrm{HV} = 900$ V are shown for the ^{60}Co lines at 1173.2 and 1332.5 keV by the values in parenthesis. 85

Bibliography

Barrillon, P. et al. (2006). MAROC Multi-Anode ReadOut Chip for MaPMTs. In Nuclear Science Symposium Conference Record, 2006. IEEE, volume 2, pages 809–814.

Berger, M. et al. (2010). Note on NIST X-Ray Attenuation Databases.

Bernlöhr, K., Barnacka, A., Becherini, Y., Blanch Bigas, O., Carmona, E., Colin, P., Decerprit, G., Di Pierro, F., Dubois, F., Farnier, C., Funk, S., Hermann, G., Hinton, J. A., Humensky, T. B., Khélifi, B., Kihm, T., Komin, N., Lenain, J.-P., Maier, G., Mazin, D., Medina, M. C., Moralejo, A., Nolan, S. J., Ohm, S., de Oña Wilhelmi, E., Parsons, R. D., Paz Arribas, M., Pedaletti, G., Pita, S., Prokoph, H., Rulten, C. B., Schwanke, U., Shayduk, M., Stamatescu, V., Vallania, P., Vorobiov, S., Wischnewski, R., Yoshikoshi, T., Zech, A., and CTA Consortium (2013). Monte Carlo design studies for the Cherenkov Telescope Array. Astroparticle Physics, 43:171–188.

Bignami, G. F., Boella, G., Burger, J. J., Taylor, B. G., Keirle, P., Paul, J. A., Mayer-Hasselwander, H. A., Pfeffermann, E., Scarsi, L., and Swanenburg, B. N. (1975). The COS-B experiment for gamma-ray astronomy. Space Science Instrumentation, 1:245–268.

Bishop, C. (1995). Neural Networks for Pattern Recognition. Advanced Texts in Econometrics. Clarendon Press.

Bloser, P. F., Ryan, J. M., McConnell, M. L., Macri, J. R., Bravar, U., Kanbach, G., Andritschke, R., Ajello, M., Zoglauer, A., Hunter, S. D., Phlips, B. F., Wulf, E. A., Hartmann, D. H., Miller, R. S., Paciesas, W. S., Zych, A. D., Kippen, R. M., Vestrand, T., Cherry, M. L., Guzik, T. G., Stacy, J. G., Wefel, J. P., Reglero, V., Di Cocco, G., and Cravens, J. P. (2005). Mega: a medium-energy gamma-ray astronomy mission concept. volume 5898, pages 589804–589804–12.

Brun, R. and Rademakers, F. (1997). Root - an object oriented data analysis framework. Nuclear Instruments and Methods in Physics Research Section A: Accelerators, Spectrometers, Detectors and Associated Equipment, 389(1-2):881–882. New Computing Techniques in Physics Research V.

de Faoite, D., Hanlon, L., Roberts, O., Ulyanov, A., McBreen, S., Tobin, I., and Stanton, K. T. (2015). Development of glass-ceramic scintillators for gamma-ray astronomy. Journal of Physics Conference Series, 620(1):012002.

Drozdowski, W. et al. (2008). $CeBr_3$ Scintillator Development for Possible Use in Space Missions. Nuclear Science, IEEE Transactions on, 55(3):1391–1396.

Fahlman, S. E. (1989). Faster-learning variations on back-propagation: An empirical study. In Touretzky, D. S., Hinton, G. E., and Sejnowski, T. J., editors, Proceedings of the 1988 Connectionist Models Summer School, pages 38–51. San Francisco, CA: Morgan Kaufmann.

Fichtel, C. E., Hartman, R. C., Kniffen, D. A., Thompson, D. J., Ogelman, H., Ozel, M. E., Tumer, T., and Bignami, G. F. (1975). High-energy gamma-ray results from the second small astronomy satellite. ApJ, 198:163–182.

Forot, M., Laurent, P., Lebrun, F., and Limousin, O. (2007). Compton telescope with a coded aperture mask: Imaging with the integral/ibis compton mode. The Astrophysical Journal, 668(2):1259.

Garcia de Acilu, P. et al. (2012). Study and optimization of positioning algorithms for monolithic PET detectors blocks. Journal of Instrumentation, 7:C6010.

Gauchet, L. and Creusot, A. (2012). Black box set-up and the first results on the Antares optical module. *ANTARES-OPMO-2012* - unpublished.

Geant4 Collaboration (2013). Geant4 Users Guide for Application Developers.

Gentit, F.-X. (2002). Litrani: a general purpose monte-carlo program simulating light propagation in isotropic or anisotropic media. Nuclear Instruments and Methods in Physics Research Section A: Accelerators, Spectrometers, Detectors and Associated Equipment, 486(1-2):35 – 39. Proceedings of the 6th International Conference on Inorganic Scin tillators and their Use in Scientific and Industrial Applications.

Gostojic, A. et al. (2013). Development of a 3D Imaging Calorimeter in Lanthanum Bromide for Gamma-Ray Space Astronomy. In Nuclear Science Symposium and Medical Imaging Conference (NSS/MIC), 2013 IEEE, pages 1–7.

Gostojic, A. et al. (2015). Application of artificial neural network in 3D imaging with lanthanum bromide calorimeter. NIMA, 787:140 – 143. New Developments in Photodetection {NDIP14}.

Gould, R. J. and Schréder, G. (1966). Opacity of the Universe to High-Energy Photons. Physical Review Letters, 16:252–254.

Grave, X., Canedo, R., Clavelin, J.-F., Du, S., and Legay, E. (2005). NARVAL a modular distributed data acquisition system with Ada 95 and RTAI. pages 5 pp.–.

Greiner, J. et al. (2012). GRIPS - Gamma-Ray Imaging, Polarimetry and Spectroscopy. Experimental Astronomy, 34:551–582.

Gumplinger, P. (2002). Optical Photon Processes in GEANT4. TRIUMF/GEANT4 Users Workshop at SLAC.

Hamamatsu Photonics K.K. (2011). Flat Panel Type Multi Anode PMT Assembly H8500/H10966 Series.

Hamrita, H., Rauly, E., Blumenfeld, Y., Borderie, B., Chabot, M., Edelbruck, P., Lavergne, L., Le Bris, J., Legou, T., Le Neindre, N., Richard, A., Rivet, M. F., Scarpaci, J. A., Tillier, J., Barbey, S., Becheva, E., Bocage, F., Bougault, R., Bzyl, R., Grévy, S., Carniol, B., Cussol, D., Désesquelles, P., Etasse, D., Galichet, E., Grévy, S., Guinet, D., Lalu, G., Lanzalone, G., Lautesse, P., Lopez, O., Martinet, G., Pierre, S., Politi, G., Rosato, E., Tamain, B., and Vient, E. (2004). Charge and current-sensitive preamplifiers for pulse shape discrimination techniques with silicon detectors. Nuclear Instruments and Methods in Physics Research A, 531:607–615.

Hellma Materials GmbH (2014). Scintillation Crystals Data Sheet.

Iltis, A. and Snoussi, H. (2015). The temporal pet camera: A new concept with high spatial and timing resolution for pet imaging. Journal of Imaging, 1(1):45.

Jan, S., Santin, G., Strul, D., Staelens, S., Autret, K. A. D., Avner, S., Barbier, R., Bardiès, M., Bloomfield, P. M., Brasse, D., Breton, V., Bruyndonckx, P., Buvat, I., Chatziioannou, A. F., Choi, Y., Chung, Y. H., Comtat, C., Donnarieix, D., Ferrer, L., Glick, S. J., Groiselle, C. J., Guez, D., Honore, P.-F., Kerhoas-Cavata, S., Kirov, A. S., Kohli, V., Koole, M., Krieguer, M., van der Laan, D. J., Lamare, F., Largeron, G., Lartizien, C., Lazaro, D., Maas, M. C., Maigne, L., Mayet, F., Melot, F., Merheb, C., Pennacchio, E., Perez, J., Pietrzyk, U., Rannou, F. R., Rey, M., Schaart, D. R., Schmidtlein, C. R., Simon, L., Song, T. Y., Vieira, J.-M., Visvikis, D., de Walle, R. V., Wieërs, E., and Morel, C. (2004). Gate: a simulation toolkit for pet and spect. Physics in Medicine and Biology, 49(19):4543.

Janecek, M. (2012). Reflectivity Spectra for Commonly Used Reflectors. IEEE Transactions on Nuclear Science, 59:490–497.

Johansson, E., Dowla, F., and Goodman, D. (1991). Backpropagation learning for multilayer feed-forward neural networks using the conjugate gradient method. International Journal of Neural Systems, 02(04):291–301.

Khazov, Y., Rodionov, A., and Kondev, F. G. (2011). Nuclear data sheets for a = 133. Nuclear Data Sheets, 112(4):855–1113.

Khodyuk, I. V. and Dorenbos, P. (2010). Nonproportional response of $LaBr_3$:Ce and $LaCl_3$:Ce scintillators to synchrotron x-ray irradiation. Journal of Physics Condensed Matter, 22:5402.

Khodyuk, I. V. et al. (2013). Energy resolution and related charge carrier mobility in $LaBr_3$:Ce scintillators. Journal of Applied Physics, 114(12):123510.

Kraushaar, W. L., Clark, G. W., Garmire, G. P., Borken, R., Higbie, P., Leong, V., and Thorsos, T. (1972). High-Energy Cosmic Gamma-Ray Observations from the OSO-3 Satellite. ApJ, 177:341.

Laureijs, R. J., Duvet, L., Escudero Sanz, I., Gondoin, P., Lumb, D. H., Oosterbroek, T., and Saavedra Criado, G. (2010). The euclid mission. volume 7731, pages 77311H–77311H–6.

Lebrun, F. et al. (2010). CAPSiTT: A Sensitive 100 keV - 100 MeV All Sky Survey . In 8th Integral Workshop. The Restless Gamma-ray Universe (INTEGRAL 2010).

Lippmann, R. (1987). An introduction to computing with neural nets. IEEE ASSP Magazine, 4(2):4–22.

Lönnblad, L., Peterson, C., and Rögnvalsson, T. (1992). Pattern recognition in high energy physics with artificial neural networks —jetnet 2.0. Computer Physics Communications, 70(1):167–182.

Mahoney, W. A., Ling, J. C., Jacobson, A. S., and Tapphorn, R. M. (1980). The HEAO 3 gamma-ray spectrometer. Nuclear Instruments and Methods, 178:363–381.

Matsuura, D., Genba, K., Kuroda, Y., Ikebuchi, H., and Tomonaka, T. (2014). "ASTRO-CAM 7000HS" Radioactive Substance Visualization Camera. Mitsubishi Heavy Industries Technical Review, 51(1):68.

McCulloch, W. S. and Pitts, W. (1943). A logical calculus of the ideas immanent in nervous activity. The bulletin of mathematical biophysics, 5(4):115–133.

Moran, P., Shearer, A., Gouiffes, C., and Laurent, P. (2013). INTEGRAL/IBIS and optical observations of the Crab nebula/pulsar polarisation. ArXiv e-prints.

Morrison, P. (1958). On gamma-ray astronomy. Il Nuovo Cimento (1955-1965), 7(6):858–865.

Motta, D. and Schonert, S. (2005). Optical properties of bialkali photocathodes. NIMA, 539(1-2):217–235.

Olive, K. A. and Particle Data Group (2014). Review of Particle Physics. Chinese Physics C, 38(9):090001.

OpenGATE Collaboration (2014). OpenGATE Users Guide.

Peterson, C., Rögnvaldsson, T., and Lönnblad, L. (1994). JETNET 3.0 – A versatile artificial neural network package. Computer Physics Communications, 81:185–220.

Predehl, P., Andritschke, R., Becker, W., Bornemann, W., Bräuninger, H., Brunner, H., Boller, T., Burwitz, V., Burkert, W., Clerc, N., Churazov, E., Coutinho, D., Dennerl, K., Eder, J., Emberger, V., Eraerds, T., Freyberg, M. J., Friedrich, P., Fürmetz, M., Georgakakis, A., Grossberger, C., Haberl, F., Hälker, O., Hartner, G., Hasinger, G., Hoelzl, J., Huber, H., von Kienlin, A., Kink, W., Kreykenbohm, I., Lamer, G., Lomakin, I., Lapchov, I., Lovisari, L., Meidinger, N., Merloni, A., Mican, B., Mohr, J., Müller, S., Nandra, K., Pacaud, F., Pavlinsky, M. N., Perinati, E., Pfeffermann, E., Pietschner, D., Reiffers, J., Reiprich, T., Robrade, J., Salvato, M., Santangelo, A. E., Sasaki, M., Scheuerle, H., Schmid, C., Schmitt, J., Schwope, A. D., Sunyaev, R., Tenzer, C., Tiedemann, L., Xu, W., Yaroshenko, V., Walther, S., Wille, M., Wilms, J., and Zhang, Y.-Y. (2014). eROSITA on SRG. In Space Telescopes and Instrumentation 2014: Ultraviolet to Gamma Ray, volume 9144 of Proc. SPIE, page 91441T.

Quarati, F. G. A. et al. (2013). Scintillation and detection characteristics of high-sensitivity $CeBr_3$ gamma-ray spectrometers. Nuclear Instruments and Methods in Physics Research A, 729:596–604.

Rögnvaldsson, T. (1994). On langevin updating in multilayer perceptrons. Neural Computation, 6(5):916–926.

Rojas, R. (1996). Neural Networks: A Systematic Introduction. Springer-Verlag New York, Inc., New York, NY, USA.

Rosenblatt, F. (1958). The perceptron: A probabilistic model for information storage and organization in the brain. Psychological Review, 65(6):386–408.

Rumelhart, D. E., Hinton, G. E., and Williams, R. J. (1986). Learning representations by back-propagating errors. Nature, 323(6088):533–536.

Schotanus, P. (2015). Development and application of novel scintillators on an industrial scale. Workshop on Applications of Novel Scintillators in Research and Industry - ANSRI 2015.

Swanenburg, B. N., Bennett, K., Bignami, G. F., Buccheri, R., Caraveo, P., Hermsen, W., Kanbach, G., Lichti, G. G., Masnou, J. L., Mayer-Hasselwander, H. A., Paul, J. A., Sacco, B., Scarsi, L., and Wills, R. D. (1981). Second COS B catalog of high-energy gamma-ray sources. ApJ, 243:L69–L73.

Takahashi, T. et al. (2012). The ASTRO-H X-ray Observatory. volume 8443, pages 84431Z–84431Z–22.

Tatischeff, V., Kiener, J., Sedes, G., Hamadache, C., Karkour, N., Linget, D., Astorino, A. T., Bardalez Gagliuffi, D. C., Blin, S., and Barrillon, P. (2010). Development of an Anger camera in Lanthanum Bromide for gamma-ray space astronomy in the MeV range. In Eighth Integral Workshop. The Restless Gamma-ray Universe (INTEGRAL 2010), page 107.

Ulyanov, A. et al. (2013). Study of silicon photomultipliers for the readout of scintillator crystals in the proposed GRIPS \gamma-ray astronomy mission. ArXiv e-prints.

van Dam, H. T. et al. (2012). Optical Absorption Length, Scattering Length, and Refractive Index of $LaBr_3:Ce^{3+}$. Nuclear Science, IEEE Transactions on, 59(3):656–664.

von Ballmoos, P. (2007). Focusing Telescopes in Nuclear Astrophysics. Springer Netherlands.

von Ballmoos, P., Alvarez, J., Barrière, N., Boggs, S., Bykov, A., Del Cura Velayos, J. M., Frontera, F., Hanlon, L., Hernanz, M., Hinglais, E., Isern, J., Jean, P., Knödlseder, J., Kuiper, L., Leising, M., Pirard, B., Prost, J.-P., da Silva, R. M. C., Takahashi, T., Tomsick, J., Walter, R., and Zoglauer, A. (2012). A DUAL mission for nuclear astrophysics. Experimental Astronomy, 34:583–622.

Wei, H., , et al. (2014). The scintillation properties of $CeBr_{3-x}Cl_x$ single crystals. Journal of Luminescence, 156:175 – 179.

Zoglauer, A., Andritschke, R., and Schopper, F. (2006). MEGAlib: The Medium Energy Gamma-ray Astronomy Library. 50:629–632.

Zoglauer, A., Boggs, S. E., Galloway, M., Amman, M., Luke, P. N., and Marc Kippen, R. (2011). Design, implementation, and optimization of MEGAlib's image reconstruction tool Mimrec. Nuclear Instruments and Methods in Physics Research A, 652:568–571.

Zoglauer, A., Weidenspointner, G., Galloway, M., Boggs, S. E., and Wunderer, C. (2009). Cosima - the cosmic simulator of megalib. In Nuclear Science Symposium Conference Record (NSS/MIC), 2009 IEEE, pages 2053–2059.

Zoglauer, A. C. (2006). First light for the next generation of Compton and pair telescopes : Development of new techniques for the data analysis of combined Compton and pair telescopes and their application to the MEGA prototype. PhD thesis, PhD Thesis, Garching: Max-Planck-Institut für Extraterrestrische Physik, 2006, MPE Report, No. 289.

université PARIS-SACLAY | ÉCOLE DOCTORALE PHENIICS

Titre : Développement d'un télescope Compton avec un calorimètre imageur 3D pour l'astronomie gamma

Mots clés: Astronomie gamma, Télescope Compton, Imagerie gamma, Détecteurs, Scintillateurs, Simulation par ordinateur – Logiciels, Réseau de neurones

Résumé: La thèse porte sur le développement d'un petit prototype de télescope Compton pour l'astronomie gamma spatiale dans la gamme d'énergie du MeV (0.1-100 MeV). Nous avons étudié de nouveaux modules de détection destinés à l'imagerie Compton. Nous avons assemblé et testé 2 détecteurs à scintillation, l'un avec un cristal de bromure de lanthane dopé au cérium ($LaBr_3$:Ce) et l'autre avec un cristal de bromure de cérium ($CeBr_3$). Les deux cristaux sont couplés à des photomultiplicateurs multi-anodes 64 voies sensibles à la position. Notre objectif est d'optimiser la résolution en énergie en même temps que la résolution en position du premier impact d'un rayon gamma incident dans le détecteur. Les deux informations sont vitales pour la reconstruction d'une image avec le prototype de télescope à partir de l'effet Compton. Nous avons développé un banc de test pour étudier expérimentalement les deux modules, avec une électronique de lecture et un système d'acquisition de données dédiés. Nous avons entrepris un étalonnage précis du dispositif et effectué de nombreuses mesures avec différentes sources radioactives. En outre, nous avons réalisé une simulation numérique détaillée de l'expérience avec le logiciel Geant4 et effectué une étude paramétrique extensive pour modéliser au mieux la propagation des photons ultraviolet de scintillation et les propriétés optiques des surfaces à l'intérieur du détecteur. Nous avons alors développé une méthode originale de reconstruction de la position d'impact en 3D, en utilisant un réseau de neurones artificiels entrainé avec des données simulées. Nous présentons dans ce travail tous les résultats expérimentaux obtenus avec les deux modules, les résultats de la simulation Geant4, ainsi que l'algorithme basé sur le réseau de neurones. En plus, nous donnons les premiers résultats sur l'imagerie Compton obtenus avec le prototype de télescope et les comparons avec des performances simulées. Enfin, nous concluons en donnant un aperçu des perspectives d'avenir pour l'imagerie gamma Compton et considérons une application possible en discutant d'un concept de télescope spatial semblable à notre prototype.

Title : Development of a Compton Telescope with a 3D imaging calorimeter for gamma-ray astronomy.

Keywords: gamma-ray astronomy, Compton telescope, gamma-ray imaging, detectors, scintillators, Computer simulation – Software, Neural networks

Abstract: The thesis aims to develop a small prototype of a Compton telescope for future space instrumentation for gamma-ray astronomy. Telescope's main target is the MeV range (0.1-100MeV). We studied novel detector modules intended for Compton imaging. We assembled and tested 2 modules, one with a cerium-doped lanthanum(III) bromide ($LaBr_3$:Ce) crystal and the other with cerium(III) bromide ($CeBr_3$). Both modules are coupled to and read out by 64-channel multi-anode PMTs. Our goals are to obtain the best possible energy resolution and position resolution in 3D on the first impact of an incident gamma-ray within the detector. Both values are vital for successful reconstruction of a Compton image with the telescope prototype. We developed a test bench to experimentally study both modules and have utilized a customized readout electronics and data acquisition system. We conducted a precise calibration of the system and performed experimental runs utilizing different radioactive sources. We have written a detailed Geant4 simulation of the experiment and performed an extensive parametric study on defining the surfaces and types of scintillation propagation within the scintillator. We utilized simulated data to train an Artificial Neural Network (ANN) algorithm to create a simplified 3D impact position reconstruction method and in addition developed an approximation routine to estimate the standard deviations for the method. We show all experimental results obtained by both modules, results from the Geant4 simulations and from the ANN algorithm. In addition, we give the first results on Compton imaging with the telescope prototype and compare them with simulated performance. We analyzed and discussed the performance of the modules, specifically spectral and position reconstruction capabilities. We conclude by giving an overview of the future prospects for gamma-ray imaging and consider possible applications showing a concept of a space telescope based on our prototype.

Université Paris-Saclay
Espace Technologique / Immeuble Discovery
Route de l'Orme aux Merisiers RD 128 / 91190 Saint-Aubin, France